UNIVERSIDAD NACIONAL AUTÓNOMA DE MÉXICO

POSGRADO EN CIENCIAS FÍSICAS

INSTITUTO DE CIENCIAS NUCLEARES

Neutral meson measurement at ALICE experiment and phenomenology of hadronic matter created in p+p and Pb+Pb systems

TESIS

QUE PARA OPTAR POR EL GRADO DE:

DOCTOR EN CIENCIAS (FÍSICA)

PRESENTA:

EDGAR DOMINGUEZ ROSAS

TUTOR PRINCIPAL:

DR. ELEAZAR CUAUTLE FLORES

INSTITUTO DE CIENCIAS NUCLEARES

MIEMBROS DEL COMITÉ TUTOR

DR. JOSÉ ALEJANDRO AYALA MERCADO

INSTITUTO DE CIENCIAS NUCLEARES

DR. JOSÉ RUBÉN ALFARO MOLINA

INSTITUTO DE FISICA

OCTUBRE 2022

"In every age, in every place,
the deeds of the men remain the same."

— ...

Agradecimientos institucionales

A la Universidad Nacional Autónoma de México, por haberme dado la oportunidad de ser su orgulloso miembro de su comunidad y permitirme crecer tanto personal como profesionalmente.

Al Instituto de Ciencias Nucleares y Posgrado en Ciencias Físicas por abrirme sus puertas y permitirme usar sus instalaciones, asi como el apoyo al gobierno Mexicano por la beca CONAHCYT.

Al Consejo Nacional de Ciencias y Tecnología, por el apoyo económico brindado a través del programa de Becas Nacionales, durante el periodo de mis estudios de posgrado.

Al programa de Apoyo a los Estudios de Posgrado (PAEP) por el apoyo económico brindado en distintos momentos de mis estudios.

Al proyecto DGAPA-PAPIIT IG100322 y BG100322, por el apoyo económico otorgado para la elaboración de este trabajo.

Al proyecto CONAHCYT: A1-S-16215, por el apoyo económico otorgado para la elaboración de este trabajo.

Agradecimientos personales

A mi madre y padre, por todo el amor y la educación que ma han dado. A los dos, gracias por toda la motivación y la confianza que han depositado en mí.

A mis hermanos Edmundo y Eduvier, por su ejemplo y las diversas lecciones que me han dado o hemos aprendido juntos.

A el Dr. Eleazar Cuautle, por ser mi tutor y haberme aceptado como tal. Por todas esas grandes enseñanzas que he recibido, por toda la paciencia que ha tenido conmigo, y más que nada por dejarme seguir con mi curiosidad científica.

A el Dr. José Alejandro Ayala Mercado y al Dr. José Rubén Alfaro Molina, por ser parte de mi comité tutor. Por todo su apoyo y sus valiosos comentarios y criticas que ayudaron a la elaboración de este trabajo.

A los miembros del jurado de titulación: Dr. Eleazar Cuautle, Dr. Alexis Aguilar, Dr. Alberto, Dr. Hermes y Dr. Gerardo, por sus comentarios y sugerencias a mi trabajo.

Resumen

En la primera parte de la tesis se analiza datos del experimento ALICE para colisiones p+p a $\sqrt{s}$ = 5.02 TeV y $\sqrt{s}$ = 13 TeV, midiendo la producción de los mesones neutros (π^0 y η) a través del canal de decaimiento Dalitz (π^0, $\eta \to \gamma^*\gamma \to e^+ + e^- + \gamma$). También son reportadas la producción (yield) en función de multiplicidad así como la fracción de decaimiento del $\pi^0 \to \gamma\gamma$ y $\pi^0 \to e^+ + e^- + \gamma$. Los resultados son comparados con las últimas mediciones de colisiones p+p a $\sqrt{s} = 2.76$ y 7 TeV, en la región de momento transverso mayor a 2 GeV/c, donde la Cromodinámica Cuántica (QCD) predice un pequeño incremento en Monte Carlo para la producción de ambos mesones.

La segunda parte de este trabajo presenta un estudio de las variables cinemáticas asociadas a colisiones p+p, p+Pb y Pb+Pb a energías de $\sqrt{s}$ =0.01, 0.9, 2.76, 7, y 13 TeV utilizando diferentes generadores de eventos Monte Carlo, analizando el comportamiento como función de la energía de colisión. Las correlaciones de multiplicidad hacia adelante-atrás son exploradas considerando diferentes fenómenos asociados a la hadronización, encontrando buen acuerdo con los resultados del experimento ALICE, solo si se incorporan los efectos de las interacciones partónicas múltiples.

En la tercera parte se analiza el momento transverso promedio de hadrones cargados como función de la multiplicidad para datos p+p, p+Pb, y Pb+Pb del experimento CMS y ALICE comparado con los generadores Monte Carlo, en busca de una posible ley de escalamiento para el momento transverso promedio escalado al área de colisión. De manera adicional, los datos experimentales son usados para calcular cantidades termodinámicas tales como la densidad de energía y entropía en el enfoque de Bjorken. Los resultados son comparados con predicciones de generadores Monte Carlo como EPOS y PYTHIA. En estos podemos observar una excelente concordancia para $\langle p_{\mathrm{T}} \rangle$ en sistemas p+p pero no para variables termodinámicas como la densidad de energía, donde un aumento repentino en un rango de $\langle p_{\mathrm{T}} \rangle$ se parece a los resultados de QCD para ϵ / T^4 en función de la temperatura; sin embargo, solo los datos experimentales de p+p muestran una especie de saturación.

Abstract

In the first part of this thesis, an analysis of ALICE p+p collisions data at $\sqrt{s} = 5.02$ TeV and $\sqrt{s} = 13$ TeV was done to measure the yield of neutral mesons (π^0 and η) through the Dalitz decay channel ($\pi^0, \eta \to \gamma^*\gamma \to e^+ + e^- + \gamma$). Additional we report the yield as a function of multiplicity distributions, as well, the fraction of decay for and $\pi^0 \to \gamma\gamma$ and $\pi^0 \to e^+ + e^- + \gamma$. The results are compared with the last experimental results from p+p collisions at $\sqrt{s} = 2.76$ and 7 TeV, in the region of transverse momentum larger than 2 GeV/c, where the Quantum Chromodynamics (QCD) predicts a slightly larger in Monte Carlo production for both mesons.

The second part of this work presents a study of global variables associated to the collisions of p+p, p+Pb and Pb+Pb energies of $\sqrt{s} = 0.01$, 0.9, 2.76, 7, and 13 TeV using different Monte Carlo event generators, analyzing the behavior in terms of the energy of the collision. The forward-backward multiplicity correlation is explored for small collision systems in terms of different hadronization mechanisms, finding an agreement with ALICE data when multiple parton interactions are included in the analysis.

The third part is the study of the average transverse momentum of charged hadrons as a function of the multiplicity

for p+p, p+Pb, and Pb+Pb data from the ALICE and CMS experiments. Comparing the results with those obtained from Monte Carlo event generators, we look for a possible scaling law of average transverse momentum scaled to the transverse collision area. Additionally, the experimental data are used to compute thermodynamical quantities such as the energy and entropy densities in the Bjorken approach. The results are compared with predictions from EPOS and PYTHIA Monte Carlo event generators. We observe an excellent agreement for the $\langle p_{\mathrm{T}} \rangle$ from p+p but not for thermodynamical observables, where a sudden rise in a small $\langle p_{\mathrm{T}} \rangle$ range resembles the lattice QCD results for the ϵ / T^4 as a function of the temperature; however, only the experimental data from p+p show a kind of saturation.

Contents

Chapter 1.

Introduction

1.1. Physics Background

According to Quantum Chronodynamics (QCD), strongly-interacting matter at high temperature or density exists. This state is called Quark-Gluon Plasma (QGP), in which the carriers of the colour charge, quarks, and gluons, are deconfined (i.e., not confined within colourless hadrons), and their properties are very different from those of ordinary hadronic matter. Such high temperature and density conditions existed in the Early Universe, a few microseconds after the Big Bang. The study and characterization of the QGP gives information on the crossover transition and insights into the equation of the state of deconfined matter [1,2]. Transitions are expected to occur in the Early Universe; such information is relevant to cosmology [3] even without neutrinos.

One way to study this fundamental state of matter is via collisions of heavy nuclei at high energies in the laboratory. Such collisions are produced at particle accelerators like the currently operating Large Hadron Collider (LHC) at CERN. For example, lead ions collide at a center-of-mass energy per nucleon pair of a few TeV: 2.76 TeV during the LHC Run1 (2010-2013) and 5.1 TeV in the Run2 (2015-2018). Large-scale experiments (ALICE, ATLAS, CMS, and also LHCb since 2015) investigate the properties of the QGP by studying the yields and kinematic distributions of the different particles produced in the collisions. In

addition, various probes are expected to test the interaction with the deconfined medium, to characterize the thermodynamic and transport properties of the QGP.

In particular, the ALICE experiment at the LHC [4] was designed to study heavy-ion physics. The properties of the quark-gluon plasma (QGP) are then studied using different probes: high-p_{T} particles and jets, heavy-flavor hadrons and their decay products, quarkonium states($J/\psi, \psi'$ and Y), azimuthal correlations between produced particles, direct photons in lead-lead (Pb-Pb) and, for reference, in proton-proton (pp) and p-Pb collisions. The ALICE experiment was designed to minimize the material budget into the acceptance while having at the same time excellent vertex resolution to be able to reconstruct secondary vertices from hyperons, D, and B mesons. The detector material budget influences the charged particle tracking and the reconstruction efficiency, the amount of produced secondaries, the energy loss corrections, and the photon conversion probability, among other variables. Therefore, achieving an accurate implementation of the complete detector in AliRoot[1] is essential.

1.1.1. Physics measurement

Many observables probe the QGP, and measurements of π^0 and η meson production over a wide transverse momentum (p_{T}) range from different colliding systems could be one of them. At low transverse momentum ($p_{\mathrm{T}} < 3$ GeV/c), light meson production in heavy-ion collisions gives an understanding of hadronization collectivity and the evolution of the QGP. At high-p_{T} ($p_{\mathrm{T}} > 5$ GeV/c), it helps to quantify parton energy loss mechanisms. However, high-p_{T} particle suppression in heavy-ion collisions may be modified by cold nuclear matter effects, such as nuclear parton distribution function (nPDF) modifications involving the vacuum. Therefore, measurements in p–A collisions are needed to disentangle cold nuclear effects from the observed high-p_{T} particle suppression in A–A collisions.

[1] AliRoot is the name ALICE Off-line framework for simulation, reconstruction, and data analysis

Different exciting probes of the QGP that can benefit from neutral meson measurements are studies of direct photon and heavy-flavor production measurements [5, 6]. The π^0 and η decay mesons are two of the most abundant sources of photons (and electrons); consequently, they generate the significant primary background for these rare probes. Furthermore, the measurement of neutral mesons over a wide transverse momentum range in p+p collisions at the LHC has been important [7–10] to understand the matter created in heavy-ion collisions. On the one hand, it allows for testing of perturbative Quantum Chromodynamics (pQCD) next leading order (NLO) calculations and provides constraints on the parton distribution functions (PDF) and fragmentation functions (FF). Parametrizations of PDFs and FFs are derived from global fits to the experimental data at various collision energies. On the other hand, it also serves as a test for phenomenological models.

The LHC found discrepancies between the measured π^0 and η meson spectra [7, 11] and pQCD calculations based on fragmentation functions, which mainly include data from experiments below the TeV scale. Since the gluon contribution becomes more dominant with the increased center of mass energy ($\sqrt{s}$), π^0 and η meson spectra at LHC energies provide new constraints on the gluon to light-flavor hadron fragmentation functions. Recent progress in understanding global QCD analysis for parton-to-pion fragmentation functions at next-to-leading order (NLO) [12] derived from inclusive pion production in semi-inclusive electron-positron annihilation, deep-inelastic scattering achieve a good and consistent description of pion spectra including the LHC results. On the other hand, the description of the η meson is of worse quality as the η FF has not yet been updated. These measurements also serve as a test for phenomenological models. The latest measurements of π^0 and η spectra in p+p collisions at $\sqrt{s}$ = 2.76, 7, and 8 TeV are shown in Fig.1.1.

The simultaneous measurement of π^0 and η mesons over a broad p_{T} range is important to explore the validity of m_{T} scaling in p+p and p–A collisions. The shape of the invariant production cross-section of various hadron species in p+p collisions can be approximated by a universal function of $m_{\mathrm{T}} = \sqrt{p_{\mathrm{T}}^2 + M^2}$ ("m_{T} scaling") [13] where M is the hadron mass. This scaling has been tested

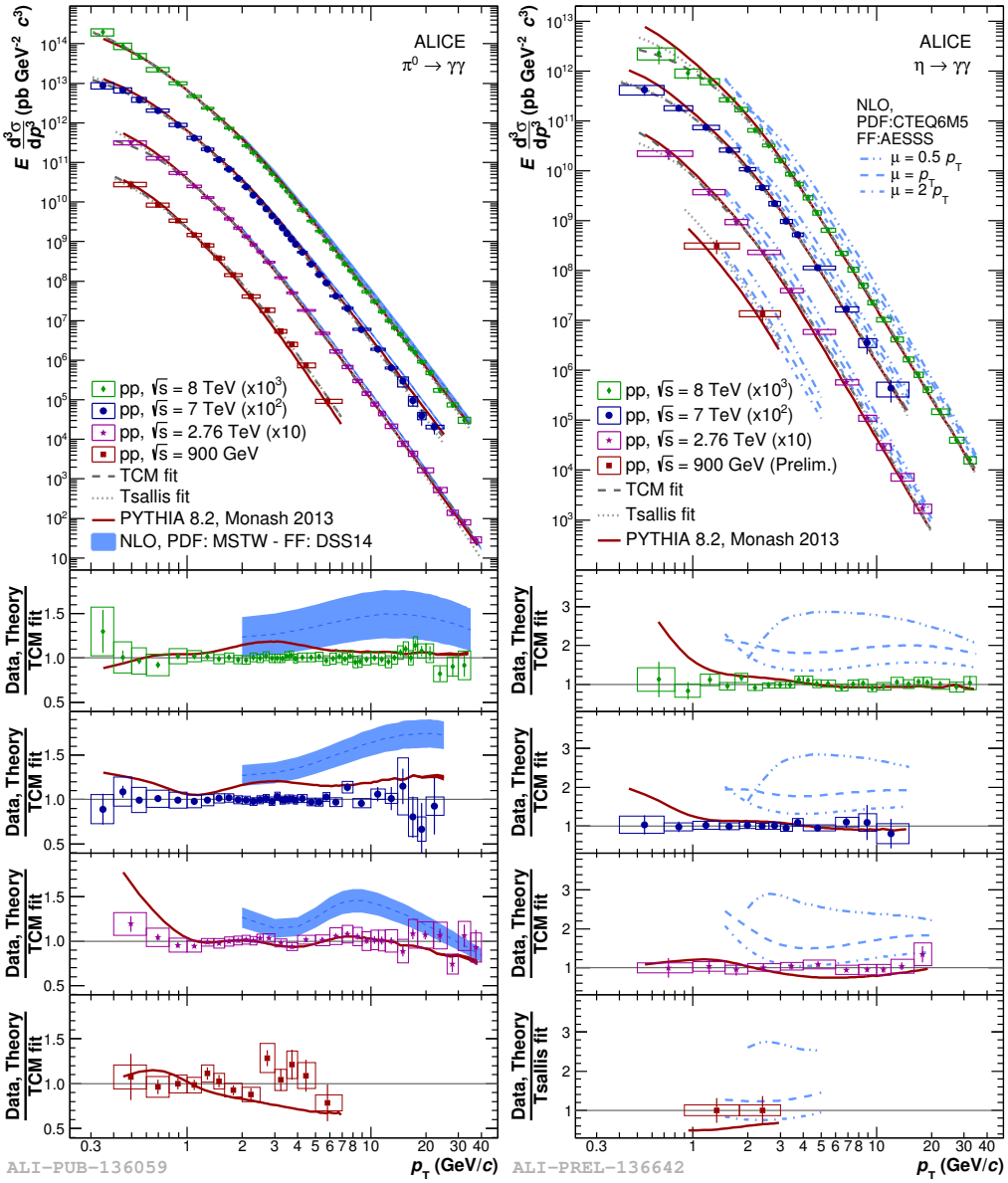

Figure 1.1.: Compilation of the π^0 and η meson differential invariant cross sections at 0.9, 2.76, 7 and 8 TeV measured by the ALICE experiment and compared to model predictions using Pythia8 and to NLO pQCD calculations.

with many collision energies and systems [14–16], and is commonly used to calculate hadronic distributions without measurements. Violation of m_T scaling at low p_T has been observed for π^0 and η mesons in p+p collisions at the LHC at $\sqrt{s}$ = 0.9 TeV [7], and at $\sqrt{s}$ = 8 TeV [10] (Fig. 1.2) and p–Pb collisions at

$\sqrt{s_{\mathrm{NN}}}$ = 5.02 TeV [17]; this may arise from a collective radial flow that is observed in p+p collisions for $\sqrt{s} > 0.9$ TeV [18]. However, a deviation from m_{T} scaling at very low p_{T} has also been observed in p–A collisions at $\sqrt{s_{\mathrm{NN}}}$ = 29.1 GeV [19], which was attributed to enhanced low p_{T} pion production from resonance decays.

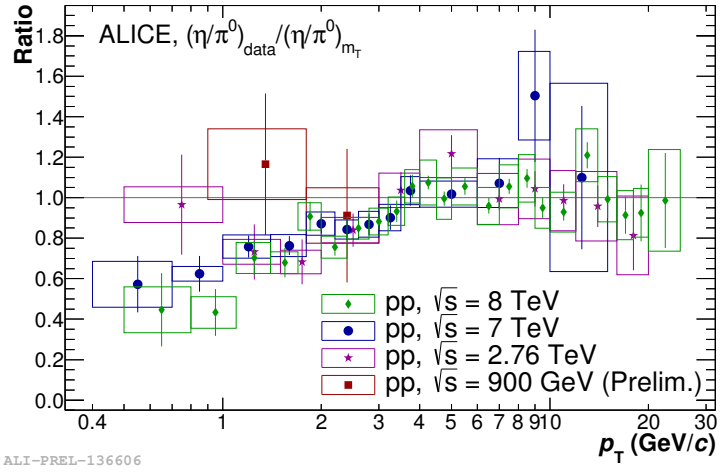

Figure 1.2.: η/π^0 ratio divided by the m_{T} scaling expectation for p+p collisions at different collision energies measured by the ALICE experiment.

ALICE has recorded data for p+p collisions at $\sqrt{s}$=13 TeV and 5 TeV during 2016, 2017 and 2018, 2015, and 2017 respectively. The total number of events recorded is of the order 3×10^9 (see Fig. 1.3) for the minimum bias trigger and of the order of 1.5×10^9 for the high multiplicity trigger. This data is the ALICE experiment's most significant sample of recorded events for p+p collisions. Therefore, a priority is to test the validity of NLO pQCD calculations at 13 TeV using the new π^0 FF [12], after the energy increase of about 60% from 8 TeV to 13 TeV. Moreover, whether the deviation from transverse mass scaling depends on collision energy (Fig. 1.2) could also be checked with the neutral meson measurement in p+p collisions at 13 TeV. On the other hand, the large sample of events with the high multiplicity trigger will allow exploring if a QGP is formed in high multiplicity p+p collisions by measuring neutral mesons for different classes of particle multiplicities and direct photons.

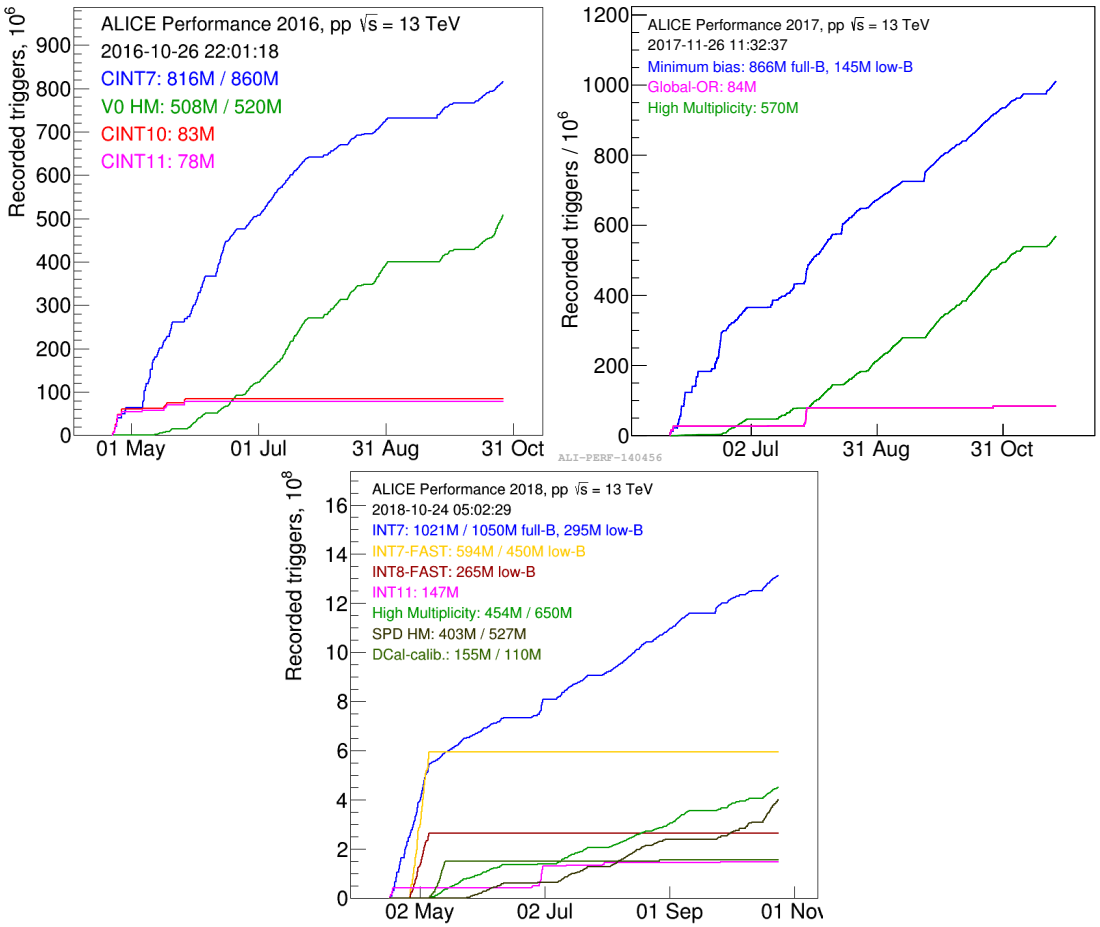

Figure 1.3.: Recorded triggers in p+p collisions at $\sqrt{s}$ = 13 TeV during the 2016, 2017 and 2018 runs.

Historically the Dalitz decay was pointed out for the first time by Richard Henry Dalitz [20] in 1951, who suggested that a photon could become a pair of electron-positron internally. Then, Budagov [21], Samios [22], and Schardt [23] measured the decay $\Gamma(\pi^0 \rightarrow e^+e^-\gamma)/\Gamma(\pi^0 \rightarrow \gamma\gamma)$=1.213 $\pm$ 0.030% [24], and these measurements made it possible to calculate the ratio of decay, which was consistent with the theoretical calculations [25], with a 2.5% difference. For this reason the ALEPH [26] collaboration made a new measurement at $\sqrt{s} = 91.2$ GeV, in Figure 1.4 shows the results obtained by ALEPH, here it can be seen how the measurement of the older experiment and the new one with respect to the theoretical results differ only by 2.0%. Furthermore, the precision can be

improved with the increase in statistics achieved by ALICE and the different energy measurement.

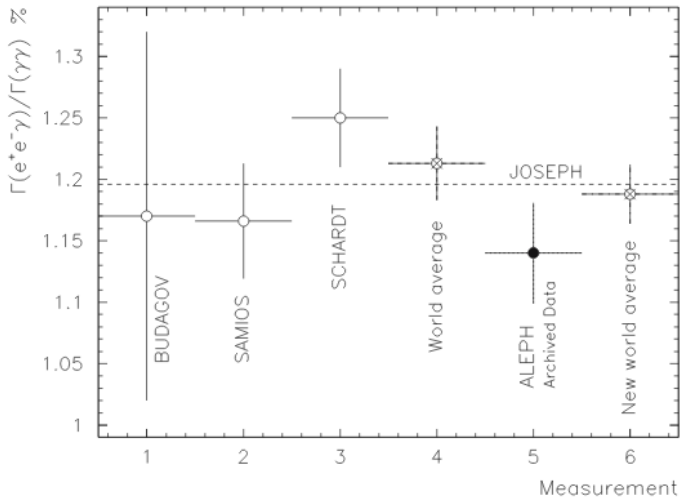

Figure 1.4.: Decay ratio of Dalitz between $\gamma\gamma$; Experimental result from Budagov, Samios and Schardt [26].

Photons are reconstructed in ALICE with electromagnetic calorimeters (PHOS, EMCal, and DCal) and with the photon conversion method (PCM), exploiting the excellent momentum resolution of the conversion photons down to the shallow transverse momentum and the high reconstruction efficiency and triggering capability of calorimeters, ITS and the TPC. Neutral mesons are reconstructed in the two-photon decay channel ($\gamma\gamma$) with different detection methods and in the Dalitz decay channel (γe^+e^-) with PCM [17,27]. The individual results are combined, taking into account the correlation of the systematic uncertainties. Thanks to the combination of independent or partially independent results, neutral mesons, and direct photons are measured over a wide transverse momentum range with outstanding precision.

The simultaneous measurement of neutral pions in the ($\gamma\gamma$) and the (γe^+e^-) decay channel with PCM allows for cross-checking the material budget in ALICE, and the uncertainty assigned to it is a vital ingredient of the PCM method to measure photons. In addition, it is possible to study, employing the Dalitz method, the production of χ_c decaying into $J/\psi + (\gamma \rightarrow e^+e^-\gamma)$, in the vast

data sample of p+p collisions at 13 TeV. A simulation study was previously presented in [28].

One of the objectives of ultra-relativistic heavy ion collision experiments such as ALICE is to recreate a Big Bang for a brief time, called micro-Big-Bang, and study the properties of the matter created, which is almost baryon-free, and corresponds to the early universe. In contrast, matter rich in baryons is expected to occur in heavy ion collisions in the Facility for Antiproton and Ion Research (FAIR) and Nuclotron-based Ion Collider fAcility (NICA), which correspond to the conditions in the core of neutron stars. Therefore, the creation and study of QGP at two extremes of baryon density is crucial for the heavy ion physics community.

There are many experimental signals to probe the QGP, for example, the collective flow, parton energy loss, and J/ψ suppression, among others. The measurement of direct and decayed photons is an excellent tool to study the QGP, and for that, we need to identify every source of hadrons producing photons to clean the spectra of photons coming from neutral mesons. Photons are created through various processes in each stage of the medium produced in heavy-ion or proton collisions.

In presence of an external magnetic field on the decay channel of neutral mesons ($\pi^0 \rightarrow \gamma\gamma$), produces a change of the branching ratio of the pions; it is explained in [29] that in the presence of strong magnetic fields, the transition between a neutral pion and a virtual photon becomes possible through the triangle diagram relevant for the chiral anomaly. Furthermore, they find that the decay mode of a π^0 into $\gamma\gamma$ cannot persist in the dominant mode in strong magnetic fields and that decay into a dilepton instead dominates over the other modes. Such contribution can lead to an anisotropic spectrum or false results. However, it is possible to analyze this type of magnetic field effect from an experimental point of view.

One more phenomenon with neutral mesons is the colour factor of gluons and quarks; the former suffer a more significant energy loss in a medium than the latter. This effect, together with the different relative contributions of quarks

and gluons to π^0 and η production, leads to different suppression patterns of the two particles [30].

Photons generated from the initial scattering of particles, such as gluon and quark, Compton scattering, quark-antiquark annihilation, and electromagnetic Bremsstrahlung, are called direct photons. After the system cools down, the photons are produced from hadron-hadron process, such as Compton scattering, the annihilation process, and the decay of the mesons (π^0, η and ω mesons) [31]. Analyzing photons at low and intermediate transverse momentum gives us an insight into the QGP signal, but it is necessary to remove every source of background on the photons signal [32], and neutral mesons are one of the primal source of background.

The recent results from ALICE have shown an intriguing behavior because the system created in a collision, instead of being a QGP, is an sQGP, a strongly interacting system. The list of questions to answer and how to address these is exhaustive, so here we will concentrate from the experimental side to investigate the neutral mesons (π^0 and η) in an Dalitz decay mode. Another problem is the collective phenomena in both small [33] and large systems with finite size [34,35]. From the phenomenological point of view we address the collective phenomena in both small and large systems, considering only charged particles.

Chapter 2.

Experimental measurement

The production of neutral mesons is studied through their Dalitz decay channel. The results of this part are based in two analysis notes for the ALICE collaboration for 5 TeV [36] and 13 TeV [37]. The section will explain the PCM-Dalitz procedure [27] and the data information used in this work. The following section describes the selection of the events for the Dalitz decay channel, starting with the physics selection cuts for the electron-positron coming from the primary vertex; with this pair, we construct our candidate of virtual photon for the Dalitz decay. Afterward, we explain the selection of the candidates for the photon conversion using the V^0. Further ahead, we illustrate all the processes of the reconstruction from the invariant mass candidates for Dalitz decay to the final spectra obtained. Finally, we show the final results.

2.1. Neutral meson measurement using the Dalitz decay channel

In the Dalitz decay channel, the π^0 and η mesons decay into a $\gamma^*\gamma$, i.e., electron-positron and photon with the following branching ratios $\eta \rightarrow e^+e^-\gamma$ (Branching ratio: $(6.9 \pm 0.4)x10^{-3}$) and $\pi^0 \rightarrow e^+e^-\gamma$ (Branching ratio: (1.174 ± 0.035)) [38]. In terms of their decays, Dalitz decay is in the second place after the main,

π^0 or $\eta \rightarrow \gamma\gamma$ (Branching ratio: 98.823% and 39.41%), and is more or less two orders of magnitude smaller than the main decay. Additionally, information will be shown on the selection of which condition needs to be fulfilled to get a Dalitz decay. The e^+e^- pair forming the γ^* comes directly from the primary vertex. Any ALICE photon detectors can detect the γ, but in this work, the PCM method will be used, where photons that convert into e^+e^- pairs in the detector material are reconstructed in the central barrel.

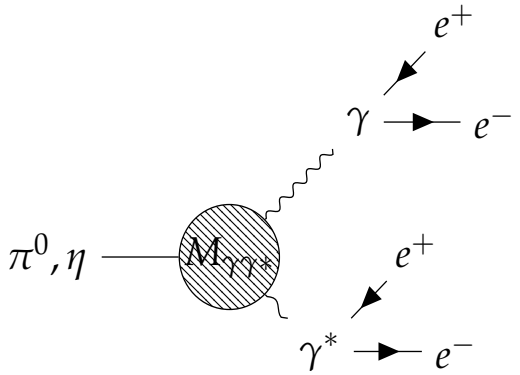

Figure 2.1.: Diagram of PCM-Dalitz.

The internal conversion process may be described as follows. A given reaction produces a virtual photon instead of a real one, producing an electron-positron pair. If the photon momentum is enormous compared to the twice mass energy of the electron (mc^2), then for pairs emitted with small transverse momentum, the energy of the intermediate state containing the photon is nearly the same as that of the final state. The associated small energy denominator highly favors this mode of production; consequently, the emitted pairs tend to have small transverse momentum. It is the predominance of "nearly real" photons in the process which tends to dissociate the conversion of the photon from its emission [39].

The invariant mass distribution of the e^+e^- pairs from the π^0 Dalitz decay follows the Kroll-Wada QED formula Eq.2.1 and the form factor Eq. 2.2:

$$\frac{d^2N_{e^+e^-}}{dM_{e^+e^-}} = \frac{2\alpha}{3\pi}\frac{1}{M_{e^+e^-}}\sqrt{1-\frac{4M_e}{M^2_{e^+e^-}}}(1+\frac{2M_e}{M^2_{e^+e^-}})(1-\frac{M_e}{M^2_{\pi^0}})^3|F(M^2_{e^+e^-})|, \quad (2.1)$$

where $M_{e^+e^-}$ is the invariant mass of the e^+e^- pair, M_e is the electron mass, $M^2_{\pi^0}$ is the π^0 mass and $F(M^2_{e^+e^-})$ is the form factor defined as:

$$F(M^2_{e^+e^-}) = \frac{1}{1 - M^2_{e^+e^-}/\Lambda^2}, \tag{2.2}$$

with $\Lambda^2 = 0.43 \pm 0.06\ GeV/c^2$. This Kroll-Wada parametrization and the invariant mass distribution $M_{e^+e^-}$ from π^0 and η Dalitz decays obtained in Monte Carlo simulations are compared 2.2. A good agreement is obtained for PYTHIA8 and the Kroll-Wada formula, for both mesons.

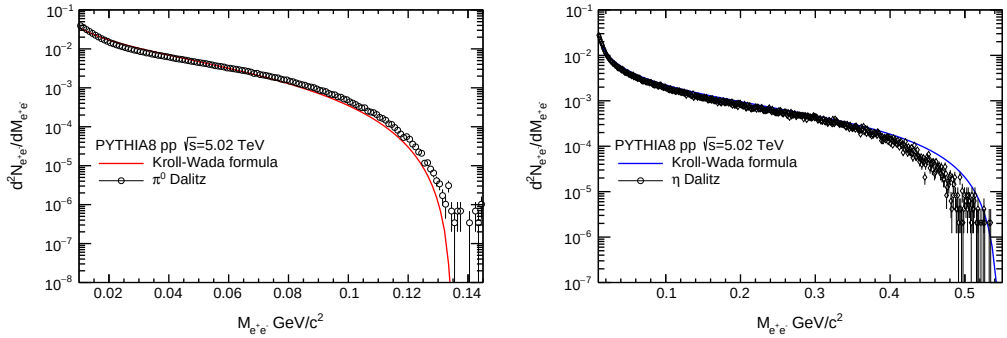

Figure 2.2.: Invariant mass distribution for π^0 (left) and η (right) Dalitz decays obtained in Monte Carlo simulations compared to the expectations from the Kroll-Wada parametrization.

2.1.1. Methodology

The Dalitz decay method used to reconstruct neutral mesons is based on the detection of four particles, two pairs of electron-positron ($\eta, \pi^0 \rightarrow \gamma e^+e^- \rightarrow e^+e^-e^+e^-$). One originates at the central interaction vertex (primary), and the other from a secondary vertex is not necessary for the principal interaction since photons convert throughout the detector material. Technically our outcome is to measure π^0 and η meson transverse momentum spectra in proton-proton collisions at $\sqrt{s} = 13$ TeV with the Dalitz decay channel. In terms of the ALICE

detectors, the method consists of the following steps, furthermore information diagram:

- The positron and the electron are detected using the TPC and ITS, this pair of particles we called primary electrons because we delimited its presence to be close of the collision.
- The gamma is detected using the Photon Conversion Method (PCM) developed by the Heidelberg and GSI groups, where the use one pair of electron and positron to reconstruct this photon with the same detectors, we called secondary electrons, not necessary on the collision vertex.
- The combinatorial background is estimated using the mixed event technique.
- The mesons peak is fitted with a convoluted function (gaussian + exponential + linear function).
- Correction for acceptance and efficiency.

One detail of every data analysis lies in choosing variables to analyze the neutral mesons since they must be justified physically and statistically. For that, we have to work on optimizing the kinematic and topological inputs of the analysis for the primary and secondary electrons, which means calculation of systematic uncertainties: corrections for variation in the input of electrons, correction factor provided by the detector materials, corrections for the reconstruction of traces, efficiency, selection of events and estimation of combinatorial noise, furthermore we will explain considerably the methodology and technique used on this thesis. All this is in parallel with the analysis of all the data sets.

2.1.2. Event Selection

We call Physics selection at the events that did not fulfill the central barrel trigger condition, calibration and beam-gas interactions (events of not physics type) are rejected. Subsequently, it is required that at least one track contributes

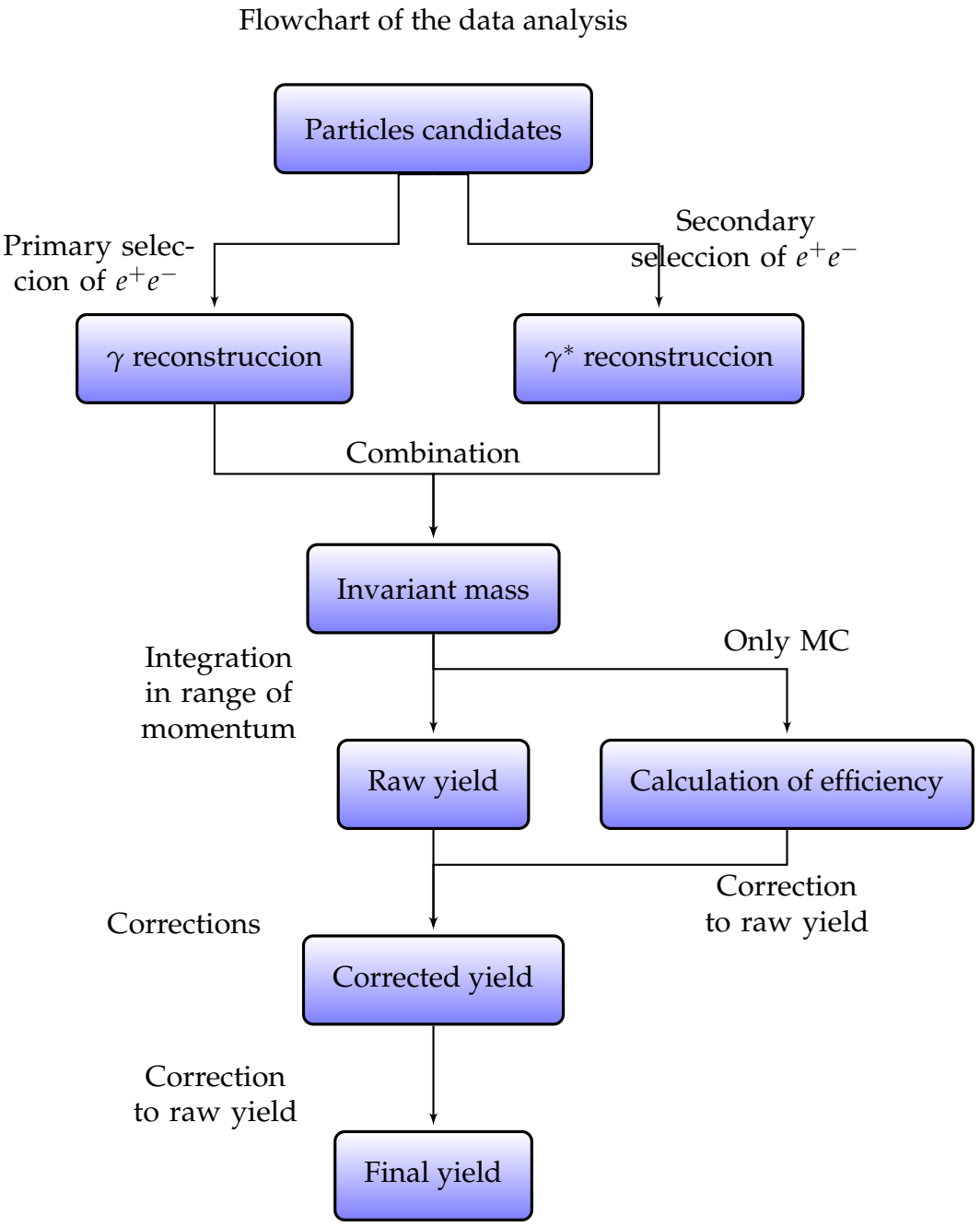

Figure 2.3.: Flowchart of the methodology used to measure the production of mesons with Dalitz decay.

to the primary vertex, which has to be within 10 cm from the center of ALICE detectors (standard for ALICE). Events that do not belong to the same event are referred to as pile-up events ($MB(Pileup)$) and need to be rejected.

$$N_{norm.evt} = N_{MB,|z_{vtx}|<10cm} + \frac{N_{MB,|z_{vtx}|<10cm}}{N_{MB,|z_{vtx}|<10cm} + N_{MB,z_{vtx}>10cm}} N_{MB,novtx} \quad (2.3)$$

The number of events used for the normalization of the neutral meson spectra is obtained as Eq. 2.3, with $N_{MB,|z_{vtx}|<10cm}$ the number of minimun bias events with vertex lower than 10 centimeters, $N_{MB,z_{vtx}>10cm}$ number of events with vertex outside of the 10 centimeters and $N_{MB,novtx}$ events with no vertex.

Data Set	N_{MB}	$N_{norm,evt}$	$\frac{MB(Vtx_{\|z_{vtx}\|<10})}{MB}$	$\frac{MB(Vtx_{\|z_{vtx}\|>10})}{MB}$	$\frac{MB(noVtx)}{MB}$	$\frac{MB(Pileup)}{MB}$
Experimental data						
LHC15n(pass4)	1.06409e+08	9.93491e+07	0.920218	0.0628447	0.0143558	0.00258152
LHC17pq(FAST+woSDD)	1.06062e+09	9.56036e+08	0.889261	0.0960115	0.0134421	0.00128539
	1.16703e+09	1.05538e+09	0.892084	0.0929874	0.0135254	0.00140357
Monte Carlo data						
LHC17e2 + LHC18j3	8.95126e+07	8.38099e+07	0.922223	0.0626086	0.0150236	0.000145041
LHC17l3b + LHC18j2	8.97893e+08	8.22889e+08	0.902391	0.0820845	0.0153552	0.000169525
	9.87406e+08	9.06699e+08	0.904189	0.0803189	0.0153251	0.000167305

Table 2.1.: Number of minimun bias events per category of experimental and Monte Carlo data.

On table 2.1 we show the different quantity used in Eq 2.3. for normalization, the overall size of the event, the fraction with vertex lower and bigger than 10 centimeters and with no vertex and pile-up normalize to MB.

2.2. Primary electron and positron selection

The electron-positron coming from the primary vertex is treated as our candidate of the virtual photon (γ^*) for the Dalitz decay. The γ^* is treated as a real photon, except with non-zero mass. One important topic was the dE/dx cut on the TPC. Studying the energy deposit in the detector in terms of nσ and dE/dx, we can observe the contribution of the charged particles; from the bottom to the top, we have π, e, K and p.
The next step in the diagram (Fig. 2.3) is the process of selecting pairs of electrons and positrons, primary and secondary, and identifying this pair of leptons with the ITS and TPC detectors, which the mechanism to detect the particles is based on the identification of the mean energy loss ($\langle dE/dx \rangle$) when these particles are traveling through the detector. It is known that the form of the distribution of the lost energy is described in principle by the Bethe-Bloch formula Eq. 2.4,

$$\left\langle \frac{dE}{dx} \right\rangle = \frac{4\pi N e^4}{mc^2} \frac{z^2}{\beta^2} \left(\ln \frac{2mc^2\beta^2\gamma^2}{I^2} - \beta^2 - \frac{\delta(\beta)}{2} \right), \tag{2.4}$$

where mc^2 is the energy in the rest of the electrons, z is the particle charge through the medium; N is the density of electrons passing through the matter, e is the elemental charge, β is the velocity of the particle, I is the mean energy of excitation of the atom, and the last $\delta(\beta)$ is the correction term for the density effects. For a snapshot, the mean energy lost on a track only depends on the particle's charge and mass. In ALICE, we have an entire group that continues working on reconstructing these tracks and refining the particles identification [40].
In the case of electrons, we consider the only ones in a range of -4 to 5 σ around the dE/dx of equation 2.4 to obtain good candidates. In my service task for ALICE, I have been refining the identification of the charged particles at low momentum using the TPC+ITS for the collaboration. This work consists in analyzing sample by sample the behavior of the mean energy lost, analyzing and fitting the parameters to optimize the identification of the charged particles.

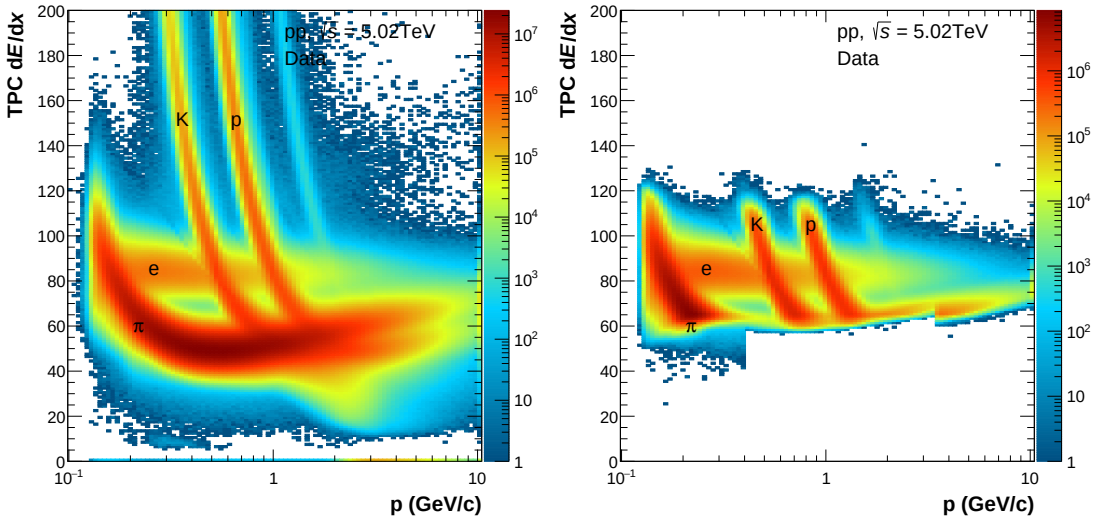

Figure 2.4.: TPC $\mathrm{d}E/\mathrm{d}x$ before (left) and after (right) the selection cut applied on the experimental data sets LHC17 and LHC15 for the primary vertex selection.

Optimizing the cut is one of the main points in the data analysis of electrons; studying different ranges on $n\sigma$ values, going from symmetric and asymmetric, plus taking the difference for the systematic is the way to go. The problem is the charged pions; there are too many in terms of statistics and can quickly overrun the electron-positron statistics at low p_T.
We need to select primary electron-positron tracks using prefilter in the Analysis Object Data files (AOD). The following selection is implemented: Tracks were required to cross at least 70 TPC pad rows, with the number of TPC clusters to be at least 80% of the number expected from the geometry of the trajectory of the track in the detector. The track selection was based on χ^2 of the ITS, and TPC clusters fit to the track.

To ensure that the selected tracks came from the primary vertex, their distance of closest approach to the primary vertex in the longitudinal direction (DCA_z) was required to be smaller than 2 cm and $DCA_{xy} < 0.0182\,\mathrm{cm} + 0.0350\,\mathrm{cm}/p_T^{1.01}$ in the transverse plane with p_T given in GeV/c which corresponds to a 7 σ selection. In addition, to minimize the contribution from photon conversions in the beam pipe and part of the SPD detector, only tracks with at least one hit in any layer of the SPD were accepted. Electrons were identified by the TPC dE/dx by

requiring that tracks fall within $-4 < n\sigma_e < 5$ of the electron hypothesis. For the pion rejection at intermediate p_{T}, the same $n\sigma_\pi$ selections as described for the conversion electron tracks was used. In contrast, at high p_{T} the selection was not applied to increase the efficiency.

Detection of charged particles is more manageable than neutral ones because one can use a magnetic field to split between positive and negative; also, with the radius of the trajectory, the identification of the hadron or lepton is transparent. On lepton selection, we have the candidates detected with the energy deposition on the TPC dE/dx and with aid from the ITS. However, detecting any particle is not perfect; at lower momentum and long angle, the candidate for hadrons and leptons need corrections.

2.2.1. Rejection of π^0 contamination

Virtual photons are reconstructed from all primary electron-positron pairs with both particles inside the acceptance. However, because it is impossible to know the pairs that correspond to the virtual photons in actual data, all the combinations between electrons and positrons are carried out, resulting in a combinatorial background where only a tiny fraction of the pairs corresponds to the desired sample.

The π^0 contamination in the primary electron-positron sample was reduced by constraints on the $\gamma*$ invariant mass ($M_{\gamma*} < 0.015 GeV/c^2$ at $p_{\mathrm{T}} < GeV/c$ and $M_{\gamma*} < 0.035 GeV/c^2$ at $p_{\mathrm{T}} > 1 GeV/c$) exploiting that most of the $\gamma*$ from π^0 Dalitz decays have a minimal invariant mass, as given by the Kroll–Wada formula Eq.[1].
Studying Monte Carlo data, we can see the different sources of electron-positron pairs. In Fig. 2.5, we can appreciate the diverse sources of lepton pairs as a function of the invariant mass after and before applying the angle cut. In gray color we have all the electron-positron candidates from the MC sampling on the detectors, in green all true electron-positrons sets, light green all electron-positron couples coming from Dalitz decay for neutral π^0, yellow the η ones (Kroll-Wada)

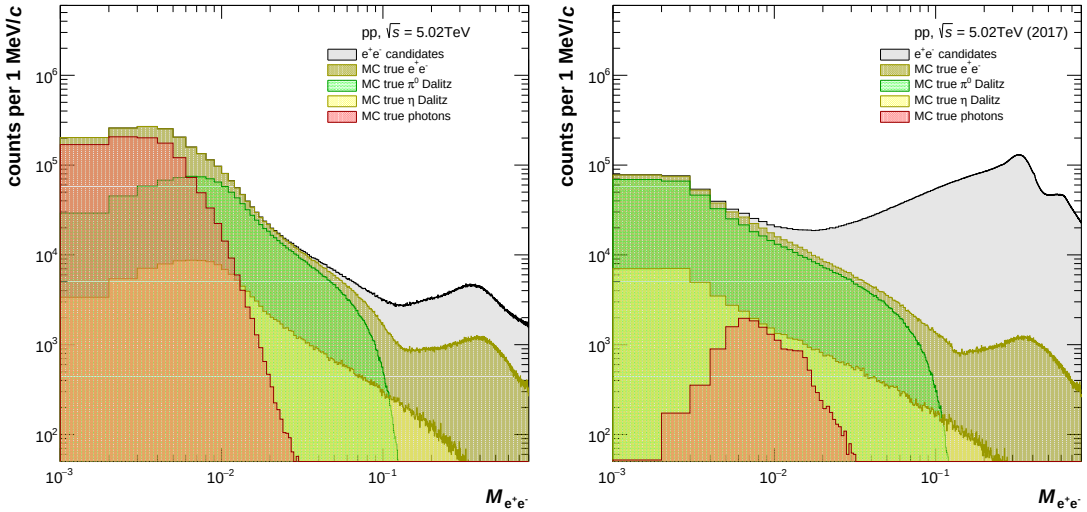

Figure 2.5.: Left Ψ_{Pair} cut not applied and on right cut applied on the invariant mass of e^+e^- candidates , true e^+e^- pairs, as well as e^+e^- pairs from true π^0 and η Dalitz decay and true γ conversion.

and in red all the electron-positron coming from a photon conversion. The invariant mass cut allow us to remove all kinds of extra unwanted candidates from our sample and create a different approach based on the momentum of the invariant mass. Afterward we select pairs in terms of the momentum, if it is lower than 1 GeV, we select mass lower than 0.015 (π^0 selection case); for momentum higher than that, we extend to 0.035 (η case).

2.2.2. Rejection of a γ conversion

Contamination that cannot be rejected with the e^+e^- invariant mass cut is the one coming from the actual photon conversion. Exploring the angle formed between the flat extension where the transverse momentum lives and the plane made by the electron-positron pairs (Ψ_{Pair}). In terms of physics, most of the photons come from a conversion that generates a small angle, while for Dalitz decay, this is not the case. In conclusion, this is remarkably important for the Dalitz decay channel because, with this variable, we can restrict the selection between the electron-positron pair coming from a photon (accepted on PCM)

and those coming directly from the γ^*.

For the Ψ_{Pair} calculation, we use the candidates' momentum for electrons and positrons, but the momentum is necessary to be close to the primary vertex. On ESD data, constrained parameters are the ones used. In AOD, the momentum constrained to the vertex is not stored, so it is needed to recalculate it. A function called *GetParamG* was implemented for this analysis.
The Ψ_{Pair} angle defined as function of $\Delta\theta_0$ and ξ_{pair} Eq. 2.7:

$$\Psi_{\text{Pair}} = arcsin\left(\frac{\Delta\Phi_0}{\xi_{\text{pair}}}\right), \tag{2.5}$$

$$\Delta\Phi_0 = \Phi_{e^-} - \Phi_{e^+}, \tag{2.6}$$

$$\xi_{\text{pair}} = arccos\left(\frac{\vec{p}_{e^-} \cdot \vec{p}_{e^+}}{||\vec{p}_{e^-}|| \cdot ||\vec{p}_{e^+}||}\right). \tag{2.7}$$

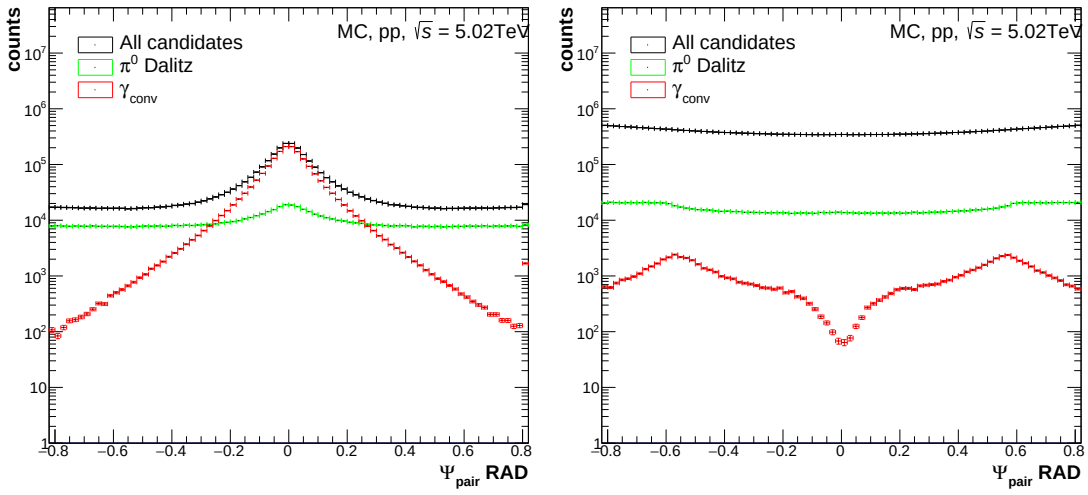

Figure 2.6.: On the left Ψ_{Pair} projection, with no cut, and on the right with cut applied. Red all γ_{conv}, green all Dalitz candidates for the neutral π^0 and black all the candidates (different volume of data compared).

Fig. 2.6 presents the Ψ_{Pair} distribution (right panel) for all electron-positron candidates (black), true electron-positrons coming from Dalitz decay for the pion (green), and the ones coming from a conversion photon (red). As seen in the

figure, the Ψ_{Pair} behavior of conversion is symmetrical around zero, contrasting with a broader distribution for the one coming from a Dalitz decay.

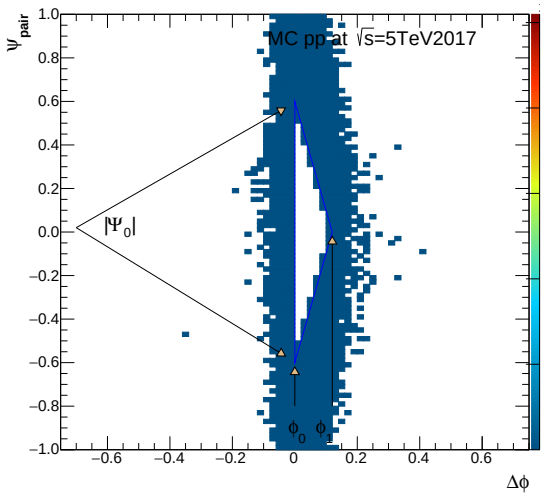

Figure 2.7.: Triangular cut on Ψ_{Pair} and Φ.

The cut we applied is the one used in the plot Ψ_{Pair} angle vs. $\Delta\Phi$ angle as shown in Fig. 2.7, a triangular cut has been defined (called Ψ_{Pair} triangular cut) to reject conversion products in the virtual photons sample. The Ψ_{Pair} triangular cut is defined as Eq. 2.8:

$$\phi_0 < \Delta\phi < \phi_1, \qquad \Psi_{\text{Pair}}| < \left(\Psi_0 - \frac{\Psi_0}{\Phi_1}\Delta\Phi\right), \tag{2.8}$$

Where Φ_0, Φ_1, and Ψ_0 are the parameters of the cut, the variation of this variable is considered for the systematic evaluation. As shown in the 2 figures, the Ψ_{Pair} triangular cut is applied to all electron-positrons candidates, meaning that it will remove Dalitz candidates. However, the ratio of γ_{conv} removed will be a factor of 2 lower. Therefore, contamination of the $\gamma\gamma$ channel will remain very low. Nonetheless, we show later on how to deal with this contribution in the error systematic. Further ahead a smarter cut was implemented, based in integrating the contamination in ranges of $\Delta\Phi$, optimizing to obtain 95% of contamination removed.

2.3. Photon Conversion selection

The photon used is reconstructed with the selection of the electron-positron pair coming from a secondary vertex, followed by the reconstruction of the photon, and quality cuts are applied. Photons converted into e^+e^- pairs are reconstructed with the secondary vertex algorithm that searches for the oppositely charged track pairs originating from a common vertex, referred to as V^0 [41]. The working principle of this so-called V^0 finder is illustrated in Fig. 2.8 with the decay of K^0_s into two pions as analogous for the photon. Since only secondary tracks should be considered, secondary vertex finder checks that the PCA (Point Close Aproach) is closer to the interaction vertex than the innermost hits of the charged tracks. Otherwise, these tracks could not originate from the PCA. Therefore, $\cos(\theta)$ is required to be larger than 0.85, with θ being the angle between the V^0 momentum vector and the straight connection between primary and secondary vertex.

The main contributors to the reconstructed V^0 sample are K^0_s, $\overline{\Lambda}$, Λ, and γ. To select photons among the V^0 candidates, several selection criteria are applied: cuts on the charged track level to ensure a good track quality, particle identification cuts on the track level for electron selection and pion rejection, and cuts on the V^0 sample that exploit the specific conversion topology of the photon as we show in table B.3.

For the identification of a conversion photon, the electron-positron pair is not restricted to the ITS trigger. The physical meaning is that the photon is stable, so it interacts over all the detector range, contrary to the virtual photon, where we required ITS trigger. For the secondary tracks to ensure quality, we select TPC refit and exclude the R range from $55 - 72$ cm where efficiency shows a lousy behavior. Also, a minimum track transverse momentum of 0.05 GeV/c is required.

The electron-positron identification for this analysis relies on the specific energy loss measurement in the TPC since the fraction of secondary tracks in the other

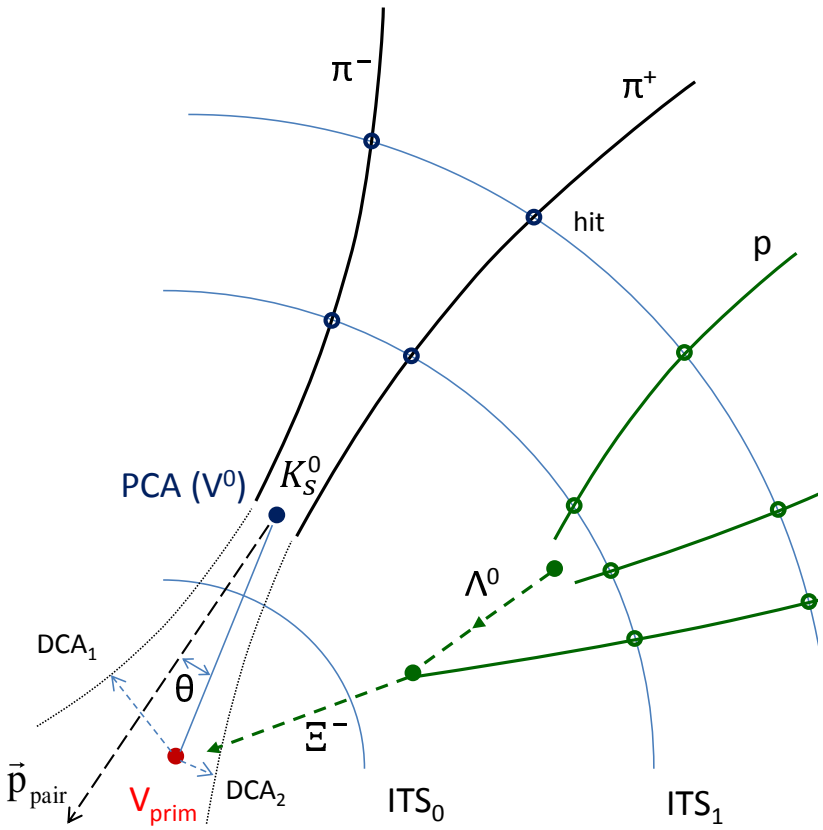

Figure 2.8.: Secondary vertex reconstruction principle, with K_S^0 and Ξ^- decays shown as an example. The solid lines represent the reconstructed charged particle tracks, extrapolated to the secondary vertex candidates. Extrapolations to the primary vertex and auxiliary vectors are shown with dashed lines [41].

detectors is significantly lower and would dramatically decrease the statistics. The cut is applied on the dE/dx hypothesis for being an electron-positron ($e^{\pm}$-line) in terms of $n\sigma_{e^{\pm}}$. In this way, most electron-positron pairs are kept while most pions are suppressed. By default, all particles with an energy loss in the range within $-3\sigma_{e^{\pm}}$ and $4\sigma_{e^{\pm}}$ are selected. Additionally, a cut concerning the /Pion hypothesis (/Pion-line) is performed to further suppress charged pions. This cut can be varied independently for low and high momentum. We use pion-line from $\sigma_{\pi^{\pm}}$ with the momentum higher than 0.5 GeV/c^2.

More information can be seen on the analyses note of the different analysis from the PCM method on proton-proton [42] [43], proton-lead [44], and

lead-lead collision [45] [46] or the tutorial page from the PWG-GA group [https://friederikebock.gitbook.io/pcgtutorial/].

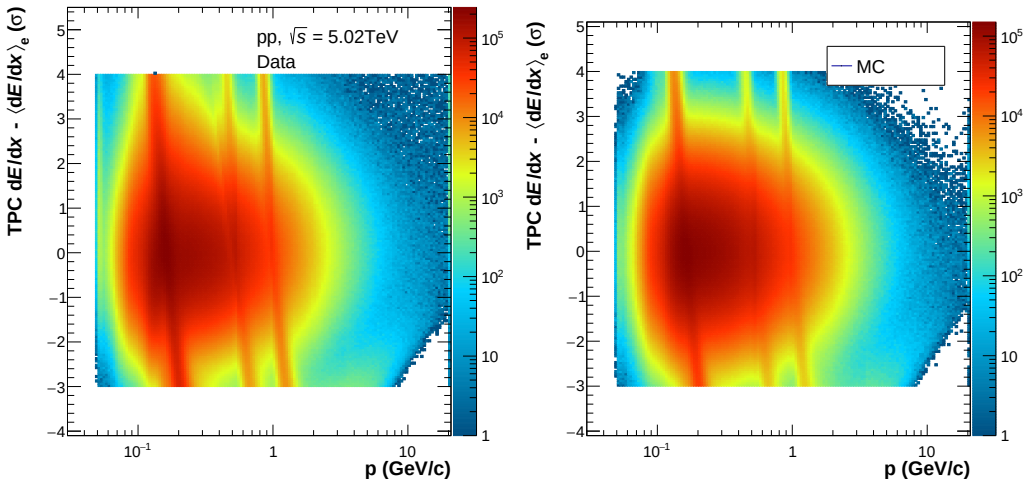

Figure 2.9.: TPC $\mathrm{d}E/\mathrm{d}x$ experimental data (left) and Monte Carlo sample (right) after the selection cut applied on the secondary vertex.

2.3.1. Armenteros Polonoski plot

In the Armenteros Polonoski plot, we can see the candidates of V^0, trajectories of charged particles traveling inside a magnetic field. Positive trajectories are curved to one side; meanwhile, negative trajectories are curved to the opposite side, named V^0 for his trajectories. In Fig. 2.10 shown the projection of momentum of the daughter particle with respect to the mother particle in the transverse direction (q_T) versus the longitudinal momentum asymmetry (α) Eq. 2.9:

$$q_T = \frac{|\overrightarrow{p_T} \times \overrightarrow{p_m}|}{|\overrightarrow{p_m}|} = |p_T| Sin(\measuredangle_{mother}^{daughter}), \qquad \alpha = \frac{p_L^+ - p_L^-}{p_L^+ + p_L^-}, \tag{2.9}$$

where p_L is the longitudinal momentum of the positive/negative particle, in the laboratory frame, the secondary electron pair, used for the photon conversion, flies inside a small opening angle, in the same direction as the photon; therefore, the momentum of the real photons is close to zero. Furthermore, the distribution

is symmetric in α as the conversion products have the same mass. For heavier particles the opening angle is larger and, consequently, the momentum is higher, as we can see on the plot for $K_s^0 \to \pi^+ + \pi^-$, $\overline{\Lambda} \to \overline{p} + \pi^+$ and $\Lambda \to p + \pi^-$.

In PCM method we want to remove the contribution of all heavier hadrons, and only obtain photons. There are two possibilities to apply the q_T cut: a one dimensional cut in Armenteros-Podolanski plot where all V^0 candidates with $q_T < q_{T,max}$ are rejected, or a two dimensional cut where all V^0 candidates follow the elliptic cut show in Eq. 2.10 and results are show in Fig. 2.10.

$$(\frac{\alpha}{0.95GeV/c})^2 + (\frac{q_T}{q_{T,max}})^2 < 1 \tag{2.10}$$

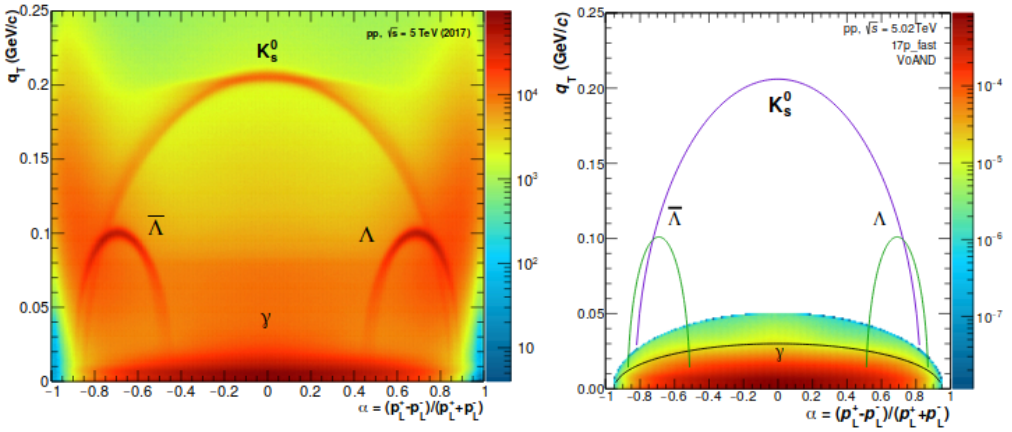

Figure 2.10.: Armenteros-Podolanski-Plot of the remaining photon candidates before (left) and after (right) all electron PID and photon cuts [42].

2.4. Reconstruction of the neutral mesons

The reconstruction of the invariant mass is carried out for both mesons using the candidates of the real and virtual photons. The calculation of the raw yield is performed in different ranges of transverse momentum and the invariant mass, difference are used as systematic errors.

In the meson selection, we must decide among different ranges and techniques. The background scheme is used with the V^0 multiplicity option offering an approach to the combinatorial background produced from counting non-meson. The specific meson selection cuts used in this analysis are displayed in table B.4.

We do not apply a direct cut at the meson reconstructed. Instead, the quality of the background is applied with at least 50 tracks, 15 degrees of freedom are taken, and a rapidity cut at 0.8. A minimum momentum for the meson is not implemented and an alpha cut which must have a range between 0.0-0.1 is demanded. The Selection window is implemented from 0.1 to 0.15; we do not share electrons and positrons between virtual and real photons, we do not require rejection of particles close to V^0, smearing and close distance approach is not applied.

The standard technique to calculate the combinatorial background is the event mixing method. Photons from different events which are by default not correlated are paired. For this purpose, we select at least 50 photon candidates from the different reconstructed events and store them in a first-in-first-out buffer for the event mixing; the resulting invariant mass distribution is purely combinatorial and suited to describe the shape of the combinatorial background. Due to a different kinematical configuration, the distribution pattern depends on the meson candidates transverse momentum, the events multiplicity, and the z-coordinate of the primary vertex.

2.4.1. Invariant mass calculation

The reconstruction of the invariant mass for the π^0 and η is done by combining all real (γ) and virtual (γ^*) photon candidates. This mass is equivalent to Eq. 2.11.

$$M^2_{\gamma\gamma^*} = m^2_{\gamma^*} + 2E_\gamma E_{\gamma^*}\left(1 - \sqrt{1 - \frac{m^2_{\gamma^*}}{E^2_\gamma}}cos(\theta_{\gamma\gamma^*})\right), \tag{2.11}$$

where we use conservation of the energy and momentum plus relativistic energy with natural units ($c = 1$), E_γ is the energy from the pair of electrons and positrons of the secondary vertex coming from PCM method.E_{γ^*} is the energy of the virtual photon, $\theta_{\gamma\gamma^*}$ is the opening angle between the γ and γ^*, m_{γ^*} is the mass of the virtual photon and if we make $m^2_{\gamma^*} = 0$, we recover the case for $\gamma\gamma$ channel.

$$\begin{aligned} E_{\gamma^*} &= E_{e^-} + E_{e^+}, \\ E_{\gamma^*} &= \sqrt{m^2_{e^+} + \vec{p_{e^+}}^2} + \sqrt{m^2_{e^-} + \vec{p_{e^-}}^2}, \end{aligned} \tag{2.12}$$

Eq. 2.12 we shows the energy E_{γ^*} in terms of the mass and momentum of the electron and positron pair.

$$m^2_{\gamma^*} = m^2_{e^+} + m^2_{e^-} + 2E_{e^+}E_{e^-} - 2\sqrt{(E^2_{e^+} - m^2_{e^+})(E^2_{e^-} - m^2_{e^-})}cos(\theta_{e^+e^-}), \tag{2.13}$$

In Eq. 2.13 we can see the virtual mass from the photon with E_{e^+}, E_{e^-}, m_{e^+} and m_{e^-} the respective energy and mass of the leptons, and $\theta_{e^+e^-}$ the angle between them e^+ and e^-. The invariant mass is calculated by combining all reconstructed virtual photons with all reconstructed real photons candidates. As a result, an invariant mass distribution composed of correlated and uncorrelated pairs is obtained. For example, in Fig. 2.11, two peaks at the rest mass of the π^0 and η mesons are seen on top of the combinatorial background.

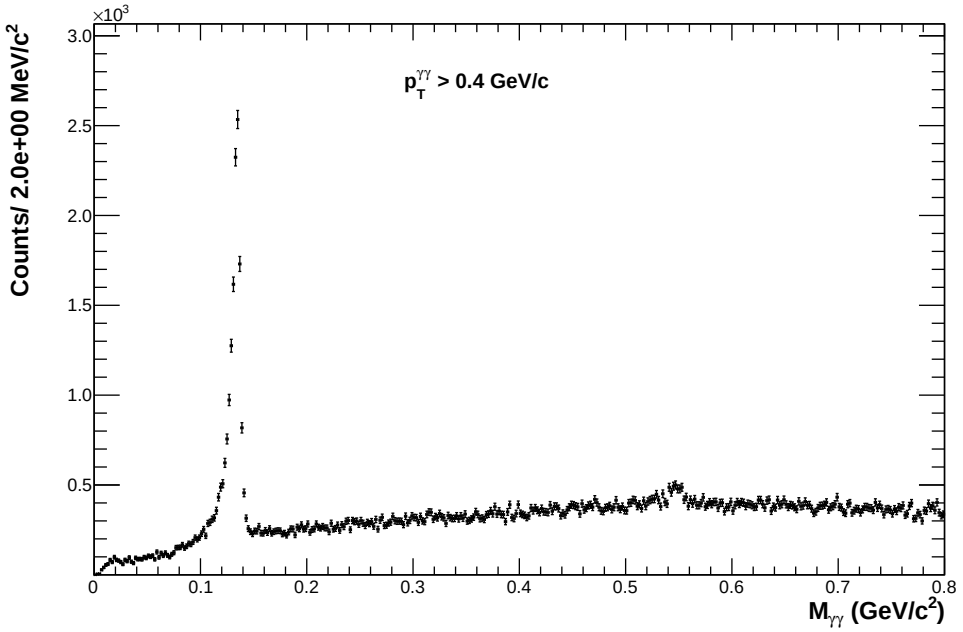

Figure 2.11.: Invariant mass distribution for π^0 and η meson.

2.4.2. Combinatorial background estimation

The combinatorial background comes mainly from uncorrelated $\gamma^*\gamma$-pairs. The combinatorial background was estimated using the mixed event technique. In this technique, real and virtual photons from different events are paired in order to avoid correlations. Therefore, the uncorrelated combinatorial background can be estimated.

The combinatorial background is better reproduced when events with similar photon multiplicity (N_γ) or with similarly charged particle multiplicity (N_{ch}) and within the same range in the Z vertex coordinate ($Vtxz$) are selected. In each event, the reconstructed γ^* are combined with reconstructed γ from previous events with the same bin class (N_{ch} (N_γ),$Vtxz$) as the current one. Afterward, the reconstructed γ of the current event is stored in the corresponding bin class of the pool. By default, classes of similar N_γ are taken.

Once the combinatorial background spectrum is obtained, the next step is normalized and scaled with the $\gamma^*\gamma$ spectrum obtained in the real event. The normalization factor is calculated by integrating the two spectra in a region

where the meson mass signal is negligible. The normalization can be done either to the left or right side of the peak. The default normalization region is chosen for the right side of the meson peak to avoid the long left tail due to the electron Bremsstrahlung effects. The actual ranges are given in Table 2.2. The left normalization is used for the evaluation of the systematic uncertainties.
The raw yield is calculated by fitting and integrating the invariant mass distribution in ranges of p_T. The raw yield of the mesons is computed by integrating the π^0 or η signal after background subtraction within the integration windows. The integration windows are estimated around the peak given by the Gaussian convoluted with an exponential fit as given in Eq 2.14. However, due to the Bremsstrahlung tail, the integration window is asymmetric around the mass peak. Therefore, the integration windows used in the analysis are given in Table 2.2. Moreover, the possible remaining background estimated from the linear fit is subtracted from the integral.

$$\frac{dN_{\gamma^*\gamma}}{dM_{\gamma^*\gamma}} = a\left(e^{-\frac{1}{2}\left(\frac{M_{\gamma^*\gamma}-M_m}{\sigma_{M_{\gamma^*\gamma}}}\right)^2} + e^{\frac{M_{\gamma^*\gamma}-M_m}{\lambda}}\left(1-e^{-\frac{1}{2}\left(\frac{M_{\gamma^*\gamma}-M_m}{\sigma_{M_{\gamma^*\gamma}}}\right)^2}\right)\theta(M_m-M_{\gamma^*\gamma})\right) + b + cM_{\gamma^*\gamma}, \tag{2.14}$$

where M_m is the meson peak position and is taken as the measured mass, $\sigma_{M_{\gamma^*\gamma}}$ corresponding to the experimental Gaussian width of the meson mother, and b and c are linear parameters. The λ parameter corresponds to the inverse slope of the exponential function. Finally, the exponential function's effect at the meson peak's right side is put to zero by the Heaviside step function $\theta(M_m - M_{\gamma^*\gamma})$. This part is to account for the Bremsstrahlung tail contribution.
In Fig. 2.12 the red dots represent the invariant mass distribution after subtraction. The fit shown in Eq. 2.14 is displayed with the blue line. The residual background under the π^0 peak in all momentum ranges remains smaller than the correction. For the η case, the residual background under the peak is more prominent than in the π^0. A higher contribution of the combinatorial background manifests in this range.

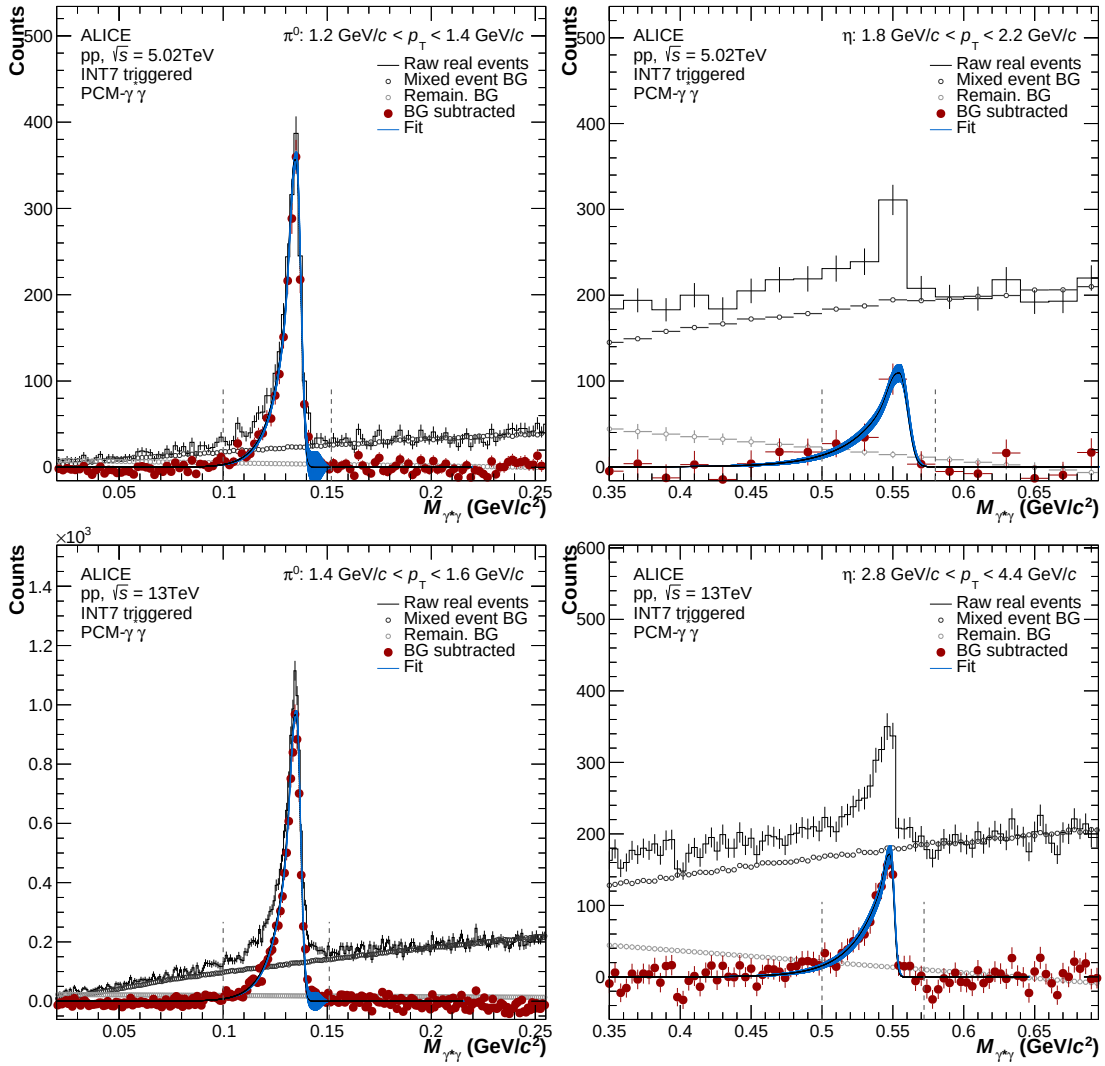

Figure 2.12.: Invariant mass for π^0 (left) and η (right) for an interval of p_T. The black histogram shows the data before combinatorial background subtraction and the red bullets after subtraction. The gray empty bullets represents the event mixing background while the blue line is a fit to the invariant mass peak after background subtraction. $\sqrt{s}$ = 5.02 TeV top and $\sqrt{s}$ = 13 TeV bottom.

We display the mass resolution between data and MC in Fig. 2.13. The π^0 exhibit good behavior at low momentum and decrease as the momentum increases (lack of statistics); for the η meson, this is different because it is heavier, and the intermediate range of momentum shows further consistent results between the

MC sample and the experimental one.

	π^0	η
Normalization window		
Right	$[0.17, 0.3]$ GeV$/c^2$	$[0.58, 0.7]$ GeV$/c^2$
Left	$[0.05, 0.08]$ GeV$/c^2$	$[0.35, 0.48]$ GeV$/c^2$
Integration range		
Standard	$M_{\pi^0} - 0.035, M_{\pi^0} + 0.015$ GeV$/c^2$	$M_\eta - 0.048, M_\eta + 0.022$ GeV$/c^2$
Wide	$M_{\pi^0} - 0.055, M_{\pi^0} + 0.025$ GeV$/c^2$	$M_\eta - 0.68, M_\eta + 0.032$ GeV$/c^2$
Narrow	$M_{\pi^0} - 0.015, M_{\pi^0} + 0.010$ GeV$/c^2$	$M_\eta - 0.033, M_\eta + 0.012$ GeV$/c^2$

Table 2.2.: Compilation of the mass range regions used for the normalization of the combinatorial mixed event background to the same event background and the π^0 and η peak integration in the standard, wide and narrow cases.

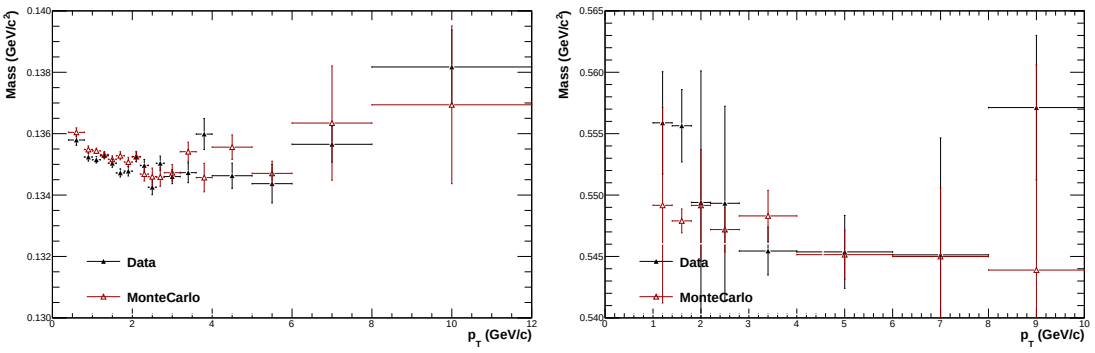

Figure 2.13.: Reconstructed mass for the π^0 and η mesons as a function of transverse momentum, for data (full black markers) and MC simulation (empty red markers).

Contamination of the $\gamma\gamma$ channel

The more probable decay for the neutral meson is the $\gamma\gamma$ channel, around 98% of all mesons. In principle, the photon could convert within all the range of the detector, meaning that even the rigorous selection for the primary pair of

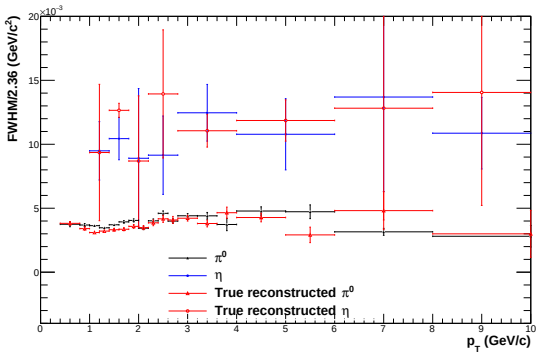

Figure 2.14.: Reconstructed mass resolution (σ=FWHM/2.36) for the π^0 (black) and η (blue) mesons as a function of transverse momentum, for data (full markers) and MC simulation (empty red markers).

electron-positron leave contributions of fake virtual photons. In the previous section, we discussed that Ψ_{pair} angle was the critical feature for removing real photons' contribution. In quantitative terms, it was removed from a 60% of contamination to $3-4\%$ as shown in Fig. 2.15 on the left side, proving that it is a fundamental variable on Dalitz analysis.

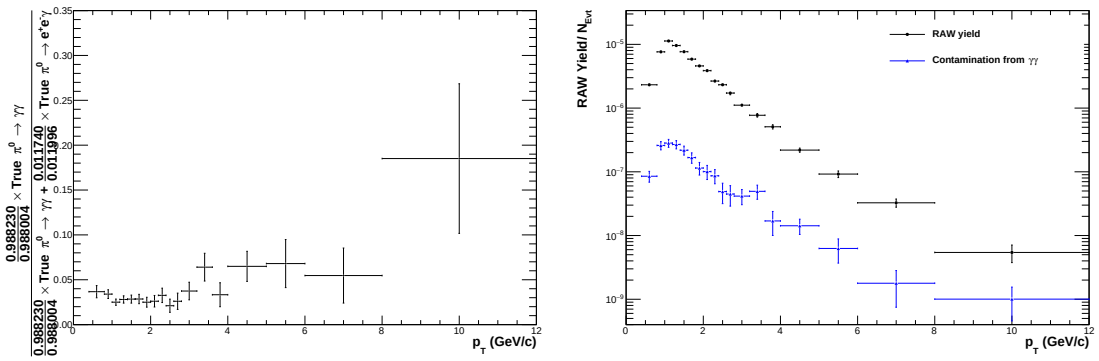

Figure 2.15.: Contamination from the $\gamma\gamma$ channel and raw yield reconstructed bin by bin with the invariant mass of the pair of V_0 for both mesons.

The remaining contamination is shown in Fig. 2.15 on the right plot; the blue distribution is the one coming from the $\gamma\gamma$ channel, and the black is shown in the raw spectra obtained from Dalitz. This quantity can be quantified; from now on, we will call $C(p_T)$. With pure data, we are unable to exclude this contribution; assuming that MC and data are equivalent, we proceed as:

$$C(p_T) = \frac{(Br^{PDG}_{\gamma\gamma}/Br^{GEANT}_{\gamma\gamma})N^{m\to\gamma\gamma}_{Raw}}{(Br^{PDG}_{\gamma\gamma}/Br^{GEANT}_{\gamma\gamma})N^{m\to\gamma\gamma}_{Raw} + (Br^{PDG}_{\gamma e^+e^-}/Br^{GEANT}_{\gamma e^+e^-})N^{m\to\gamma e^+e^-}_{Raw}}, \quad (2.15)$$

where Eq. 2.15 depends of $Br_{\gamma\gamma}$ and $Br_{\gamma e^+e^-}$ the corresponding branching ratios for the π^0 and η, $N^{m\to\gamma e^+e^-}_{Raw}$ and $N^{m\to\gamma\gamma}_{Raw}$ are the own number of particles in an interval of momentum for the mesons its decay channel. The contamination fraction is subtracted from the data using the following relation in Eq. 2.16.

$$N^{m\to\gamma e^+e^-}_{Raw}(p_T) = (1 - C(p_T))N^{m}_{Raw}(p_T), \quad (2.16)$$

with $N^{m}_{Raw}(p_T)$ the number of particles coming from our selection of data. Furthermore, analyses were taken by studying for one or two hits on the Inner Track System. Previous results show a better reduction of the contamination on the $\gamma\gamma$ channel using one hit; with two hits, results show a slight reduction in the contamination, but in raw data, remove half of the statistic, and poor statistic implies a bigger error in the fit parameter for the invariant mass. Therefore, we will only use one hit.

2.4.3. Acceptance and efficiency corrections

The result we aim at is the transverse momentum distribution for both mesons. To achieve this goal, correcting the raw yield with two factors coming from the MC reconstruction: acceptance and efficiency. The first one is defined as the ratio of mesons within a range of rapidity, whose daughter particles are inside the fiducial acceptance in pseudorapidity for Dalitz decay, overall mesons generated in the same rapidity window Eq.2.17:

$$A_m = \frac{N_{m,|y|<y_{max}} Daughters(|\eta_{\gamma,e^+e^-}| < 0.9)}{N_{m,|y|<y_{max}}}, \quad (2.17)$$

where m are π^0 or η. For efficiency the numerator accounts only for the mesons reconstructed and validated/verified Eq. 2.18:

$$\epsilon_{reco,m} = \frac{N_{m,|y|<y_{max}}(p_{T,MC})}{N_{m,|y|<y_{max}} Daughters(|\eta_{\gamma,e^+e^-}| < 0.9)(p_{T,MC})} \tag{2.18}$$

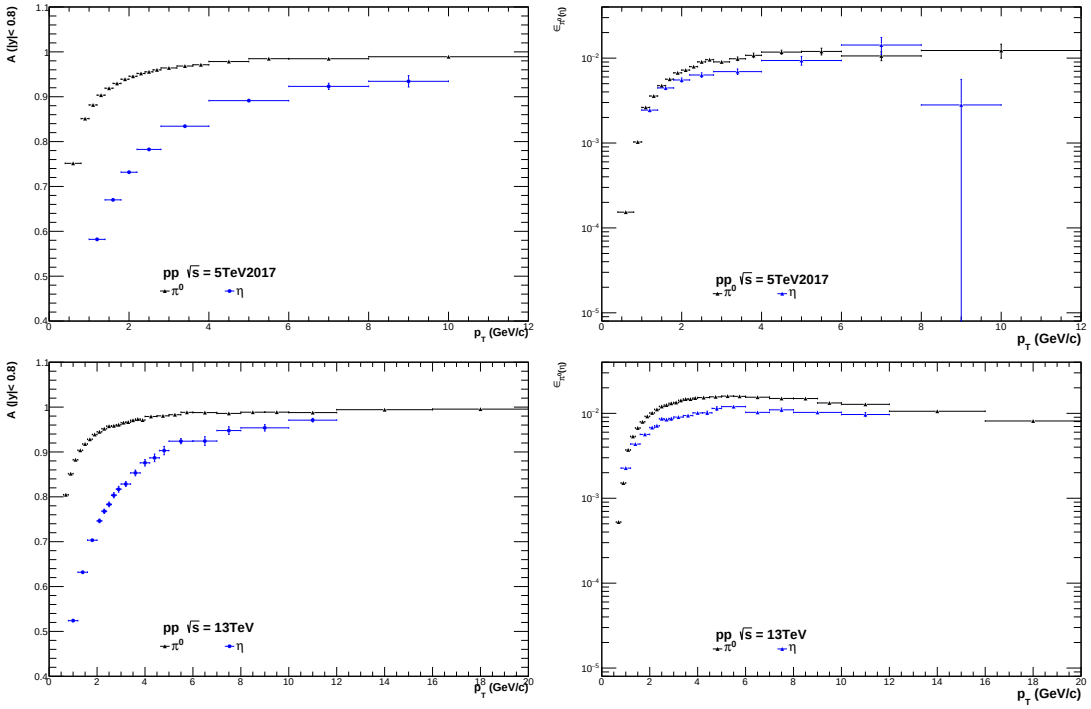

Figure 2.16.: Acceptance and efficiency for π^0 (black) and η (blue) as function of the transverse momentum.

Figure 2.16 shows acceptance and efficiency calculated from Eq. 2.17 and 2.18 for both mesons. As the mass for the η meson is larger than the mass of the π^0 meson the opening angle between the daughter particles is wider and thus the acceptance rises slower to one than the π^0 case.

2.5. Systematic uncertainty estimation

The systematic uncertainties for the π^0 and η meson are estimated varying each cut which has been performed to select the tracks, electrons, photons and mesons, one at a time. The list with all variations is given in table B.1, B.2, B.3 B.5 and B.6. The differences in the fully corrected spectra are calculated bin by bin in p_T and the errors are calculated, also bin by bin, as the maximum negative or positive deviation from the standard cut and then the average of the maximum deviations in both directions is taken as the systematic error, as shown in equation 2.19. The statistical error for each fully corrected spectrum with respect to the default one is given by $\sigma\ (p_T)$, as shown in equation 2.20, assuming that the errors among the subsets are correlated.

$$\Delta(p_T) = \frac{d^2N}{dydp_T}(p_T)_{Modified} - \frac{d^2N}{dydp_T}(p_T)_{Standard} \tag{2.19}$$

$$\sigma_{\Delta(p_T)} = \sqrt{\left|\sigma_{\frac{d^2N}{dydp_T}(p_T)_{Modified}} - \sigma_{\frac{d^2N}{dydp_T}(p_T)_{Standard}}\right|} \tag{2.20}$$

If a systematic error for one p_T bin is 0, it is checked whether the neighboring bins show larger contributions. If this is the case the systematic uncertainty is smoothed by taking the average of the neighboring bins, to avoid wrong estimations.
Once one has obtained the systematic uncertainties for each cut, we grouped in categories (see below). After we calculate the maximum and minimum variation each cut category and finally the total systematic uncertainty is calculated by adding all the sources in quadrature.

Branching ratio: The branching ratio of the π^0 meson into the Dalitz decay channel is known with a limited accuracy. Therefore, the 2.98% relative error is taken as fix systematic uncertainty.

Material Budget: The contribution of the material budget was taken from the analysis note [47]. According to the material budget error was estimated by

varying the photon conversion radius, by using the two different V^0 finder algorithms and by using different Monte Carlo simulations.

Track reconstruction: The track reconstruction groups the contribution of primary and secondary track selections. This includes the number of TPC clusters (N_{TPCcls}), the single p_T cut for primary and secondary electrons,the ratio between the found and findable clusters ($N_{found}/N_{findable}$) and the DCA_{xy} cut. Therefore, the systematic uncertainties were calculated by fitting the measured ones with polynomial functions of degree 3 and 4.

Reconstruction efficiency: This group contains the variation of the π^0 meson rapidity (y) and the variation of the pseudorapidity (η) of primary and secondary electrons. For this analysis this category is the one that make higher contribution to the systematic, specially at high momentum.

Electron selection: primary and secondary tracks: The electron selection group contains the systematic uncertainty of the particle identification. This includes the electron inclusion and π^0 rejection cuts applied in the primary and secondary electron selection on the $\mathrm{d}E/\mathrm{d}x$.

Photon selection: It contains the contribution from the cuts applied in the photon selection as the χ^2 cut and the q_T cut and the contribution of the $M_{e^+e^-}$ cut applied in the $\gamma*$ selection. As the contribution of the conversion radius, and the V^0 finder algorithms.

$\gamma\gamma$ **contamination**: Furthermore analysis where taken studying for 1 hit or two hits on the Inner Track System, previous results show a better reduction of the contamination on the $\gamma\gamma$ channel using one hit, with two hits results show a small reduction on the contamination, but in raw data, remove half of the statistic, and with lower statistic is more difficult to fit the invariant mass and so on, for that we will only use one hit.

Yield extraction: This systematic uncertainty was computed by varying the integration window used for the π^0 meson yield extraction. In the p_T region were the signal extraction seems to be more stable.

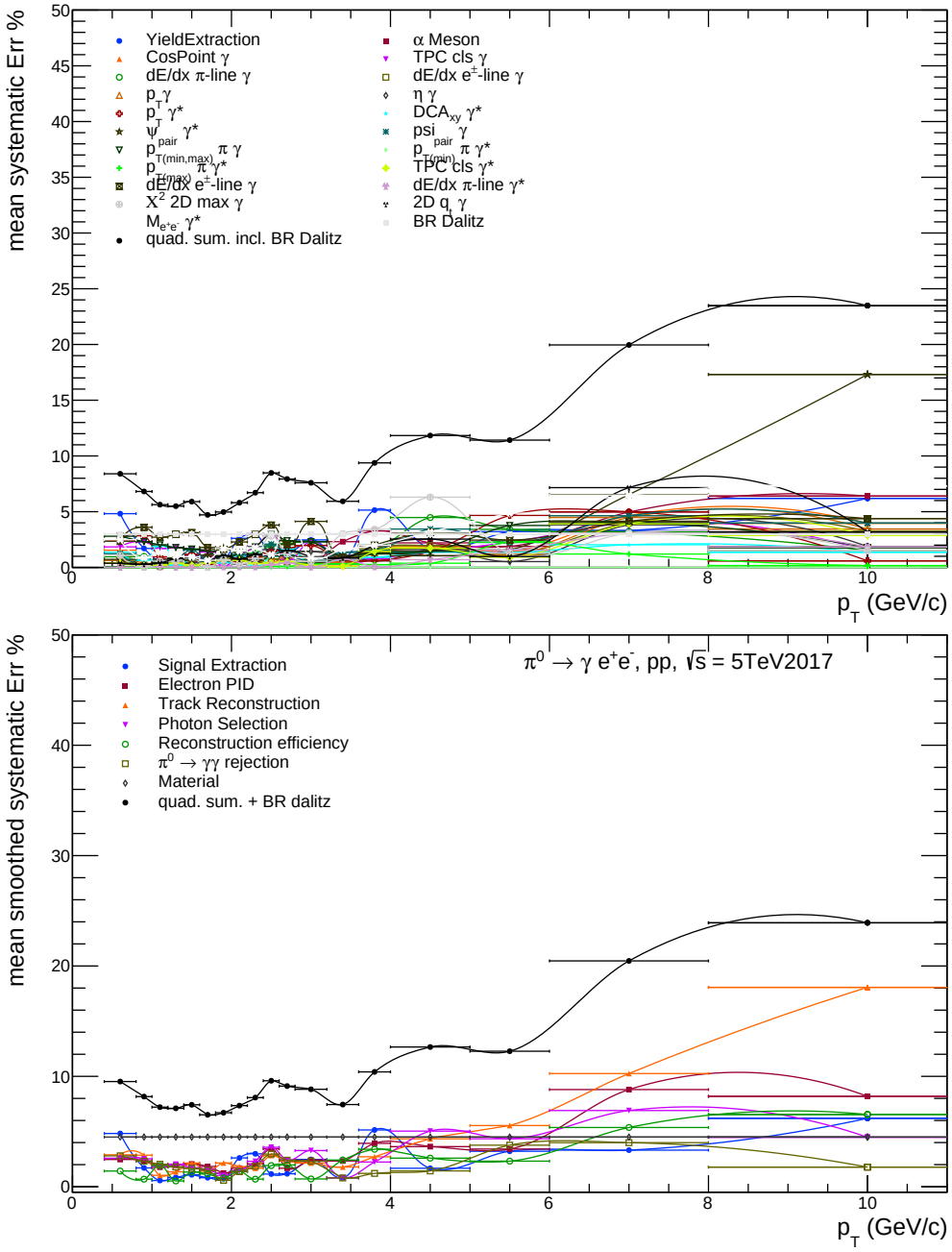

Figure 2.17.: Systematic uncertainties for all variation made for the neutral π^0. Systematic uncertainties in terms of the category for the π^0 binning

2.6. Mesons spectra

We obtain the corrected yield multiplying the raw yield with the inverse of branching ratio $Br(Dalitz)$, efficiency (ϵ), acceptance (A) and normalized to the number of events $(N_{normalization})$ as given in Eq. 2.22. Figure 2.18, shows the spectra for mesons, coming from Dalitz decay channel.

$$E\frac{d^3N}{dp^3} = \frac{d^3N}{p_T dy dp_T d\phi} = \frac{1}{2\pi p_T}\frac{d^2N}{dy dp_T} \Rightarrow \tag{2.21}$$

$$\frac{1}{2\pi p_T}\frac{1}{N_{normalization} \times \epsilon \times A \times Br(Dalitz)}\frac{N_{Raw}^{m\to e^+e^-\gamma}}{\Delta y \Delta p_T}, \tag{2.22}$$

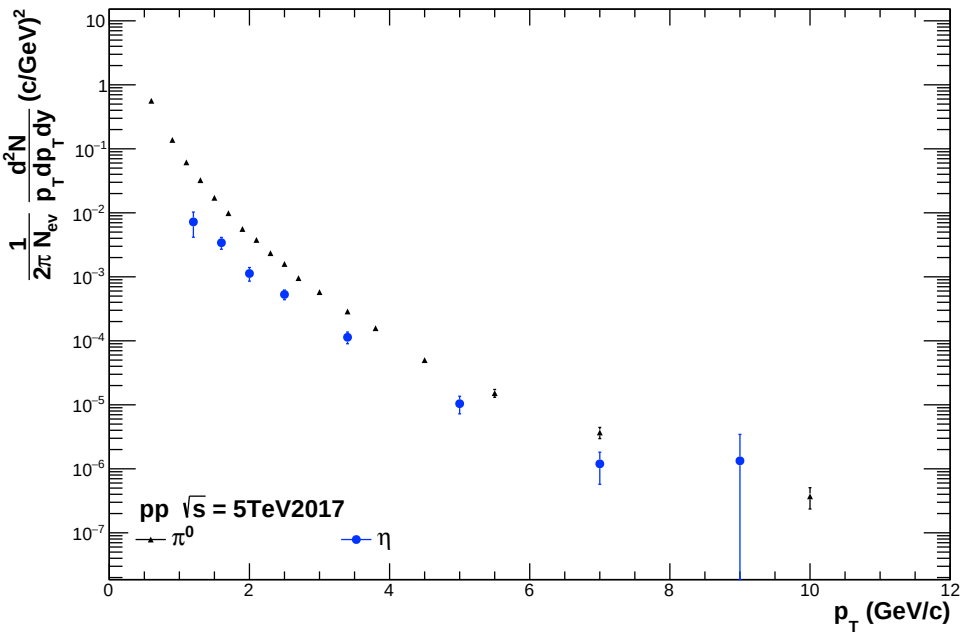

Figure 2.18.: Corrected yield for π^0 and η meson for 5 TeV.

We have reported the corrected yield for π^0 and η in Fig 2.18 from 0.4 to 10 and 1 to 10 GeV/c. Furthermore, studying the distribution of the mass bin by bin for the family of π will be interesting to corroborate the difference and understand this behavior and quantify such contributions.The η meson calculation could be

improved in terms of selection and range of binning, applying the same cut as the lower mesons. Work on the 13 TeV sampling is still on progress.

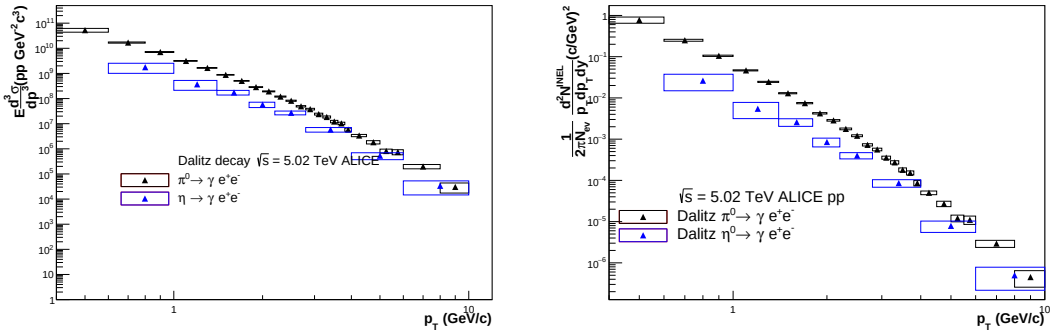

Figure 2.19.: Cross section on the left and INEL spectra on the right as function of transverse momentum.

The cross section of both mesons have been calculated, using the corrected yield and the value obtained from the theoretical side, so we can compare this spectra with those calculated with different Monte Carlo event generators. An interesting comparison should be the ratio η / π^0 for different energies where a non-linear rise is expected.

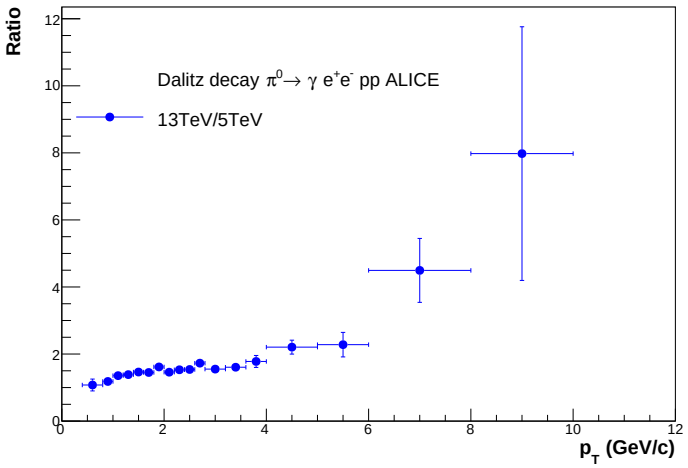

Figure 2.20.: Ratio of Dalitz decay channel for 13 TeV (First results with Dalitz) vs 5 TeV.

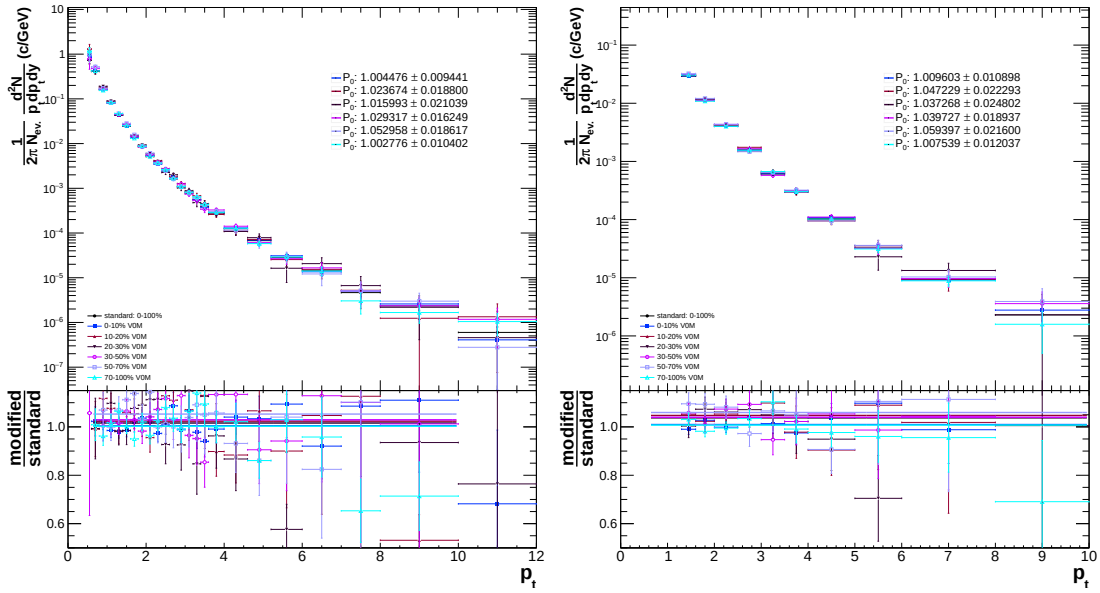

Figure 2.21.: Distribution of transverse momentum in multiplicity ranges for 13 TeV for π^0 and π^0/η ratio.

The spectra analysis in terms of the range of multiplicity is shown in Figure 2.21. In the case of the π^0, there are no significant differences (around %5 only); the spectra remain the same for the different ranges, and the same is for the ratio of π^0/η.

2.6.1. Comparison with different methods

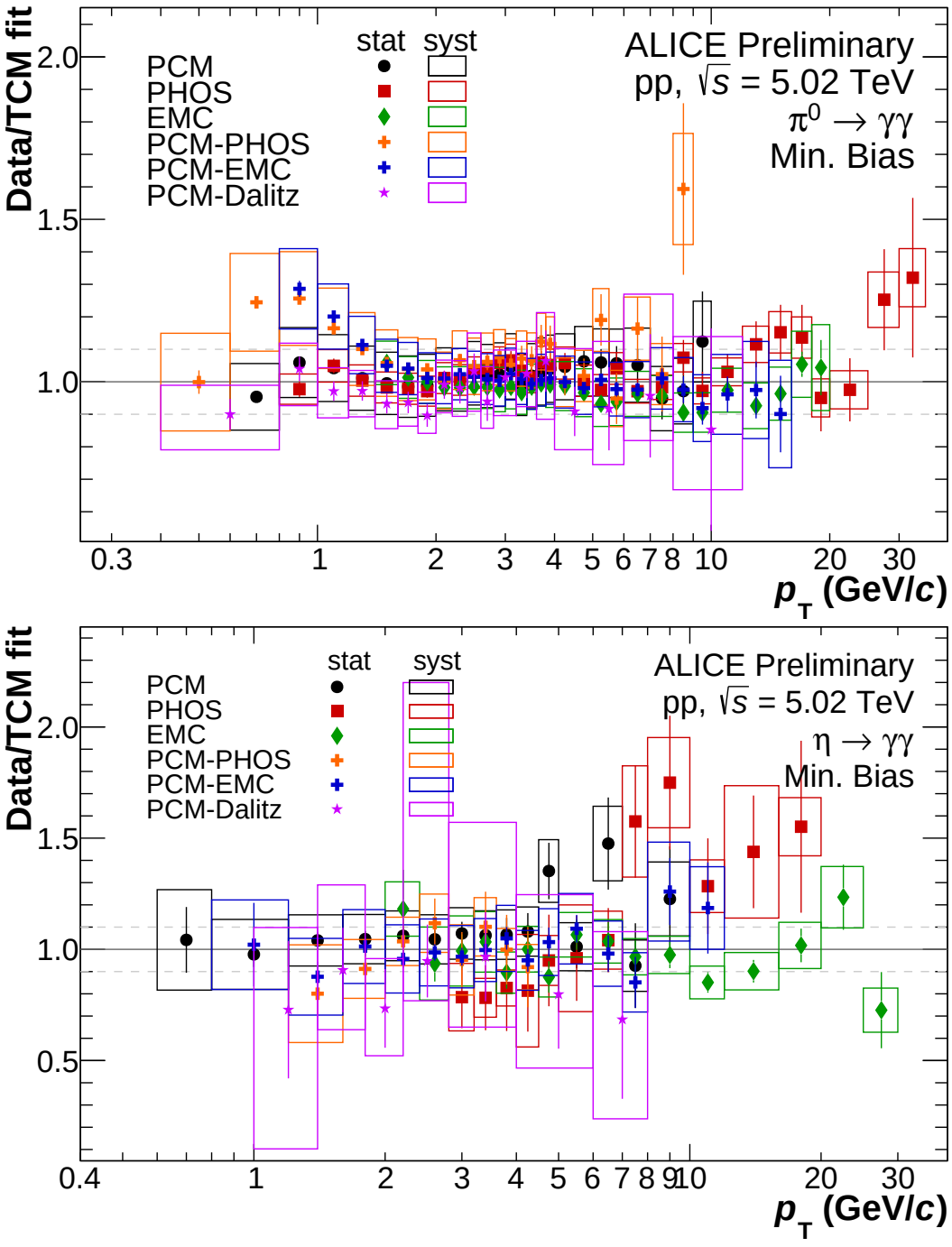

Figure 2.22.: Comparison with the different methods at $\sqrt{s} = 5.02$ TeV.

For the ALICE collaboration we have started a comparison with the different methods, on Fig. 2.22 we will show the comparison for the π^0, and η, for $\sqrt{s}$ = 5.02 TeV, and on Fig. 2.23 the ratio from charge particles for π^0 at $\sqrt{s}$ = 5.02 TeV and in Fig. 2.24 the comparison at $\sqrt{s}$ = 13 TeV. The ratio plot is very important because it gives us directly information about the contribution of the strange quark.
In this work, preliminary results on the differential invariant yield as well as the differential invariant cross section spectra for π^0 and η mesons in pp collisions at $\sqrt{s}$ = 5.02 TeV is presented. Results for the same mesons at $\sqrt{s}$ = 13 TeV are in progress.

The measurement of the π^0 and η mesons production has been carried out by detecting the final-state products of its Dalitz decay channel in the ALICE central barrel. The two primary electrons (coming from $\gamma^* \rightarrow e^+e^-$) were reconstructed using the TPC and ITS detectors. The particle identification was measured using the specific energy loss ($\mathrm{d}E/\mathrm{d}x$) in the TPC detector. On the other hand, photons (γ) were reconstructed using the Photon Conversion Method (PCM) which detects photons through their conversion products in the ALICE central barrel. The PCM requires the reconstruction of a secondary vertex, commonly known as V^0 particles which have a small difference between the angle of the secondary and the primary vertex.
The respective meson was obtained by computing the invariant mass distribution of the $\gamma^*\gamma$ pairs. The combinatorial background was estimated using the mixed event technique which combines virtual photons with photons from different events. After background subtraction, the meson signal was fitted with a gaussian function convoluted with an exponential and a linear function. The exponential function was included to take into account the long bremsstrahlung tail at the left side of the meson signal peak. The linear function was included to subtract a possible residual background below the meson signal. The meson raw yields are accomplished by integrating the invariant mass fit for every range of transverse momentum, a variation on the integration windows is taken into account.

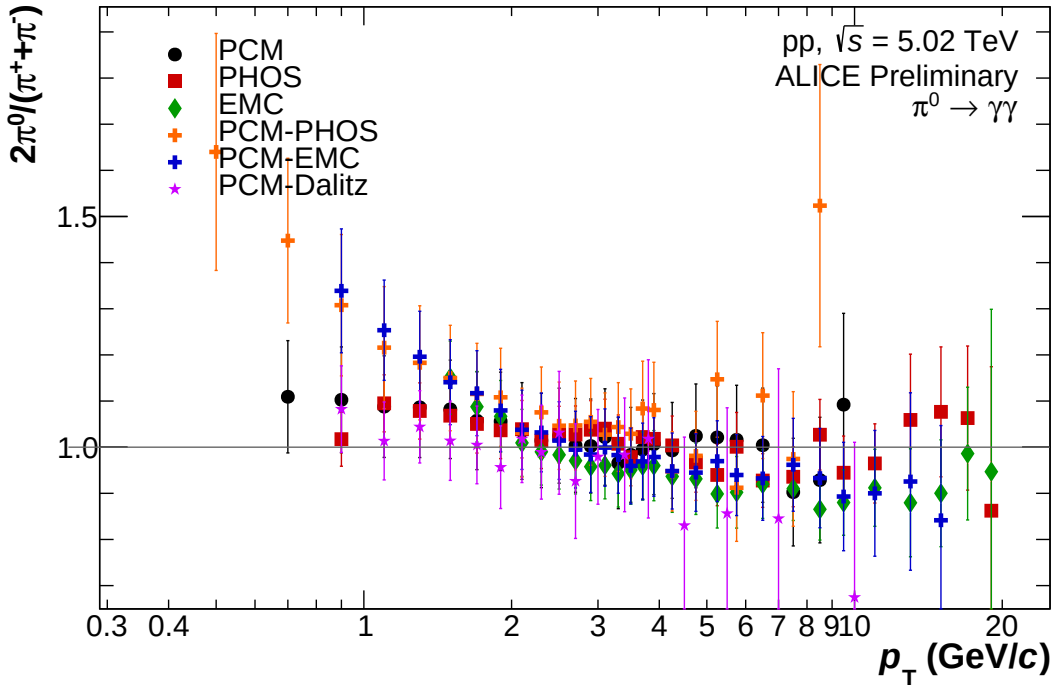

Figure 2.23.: The ratio from charge particles for π^0.

Using Monte Carlo simulation that implement PYTHIA passing trough GEANT as particle generators, the meson raw yield was corrected by acceptance and efficiency. Moreover, the contamination from the 2γ decay case in both cases was computed and subtracted from the raw yield. The systematic uncertainties were computed by varying each cut used in the virtual photon and in the photon reconstruction and in the respective meson signal extraction. As a consistency check, the measured meson spectra were compared to the others independent methods for meson reconstruction existing in ALICE: PCM, PHOS, EMCal, PCM-EMCal and PCM-PHOS.

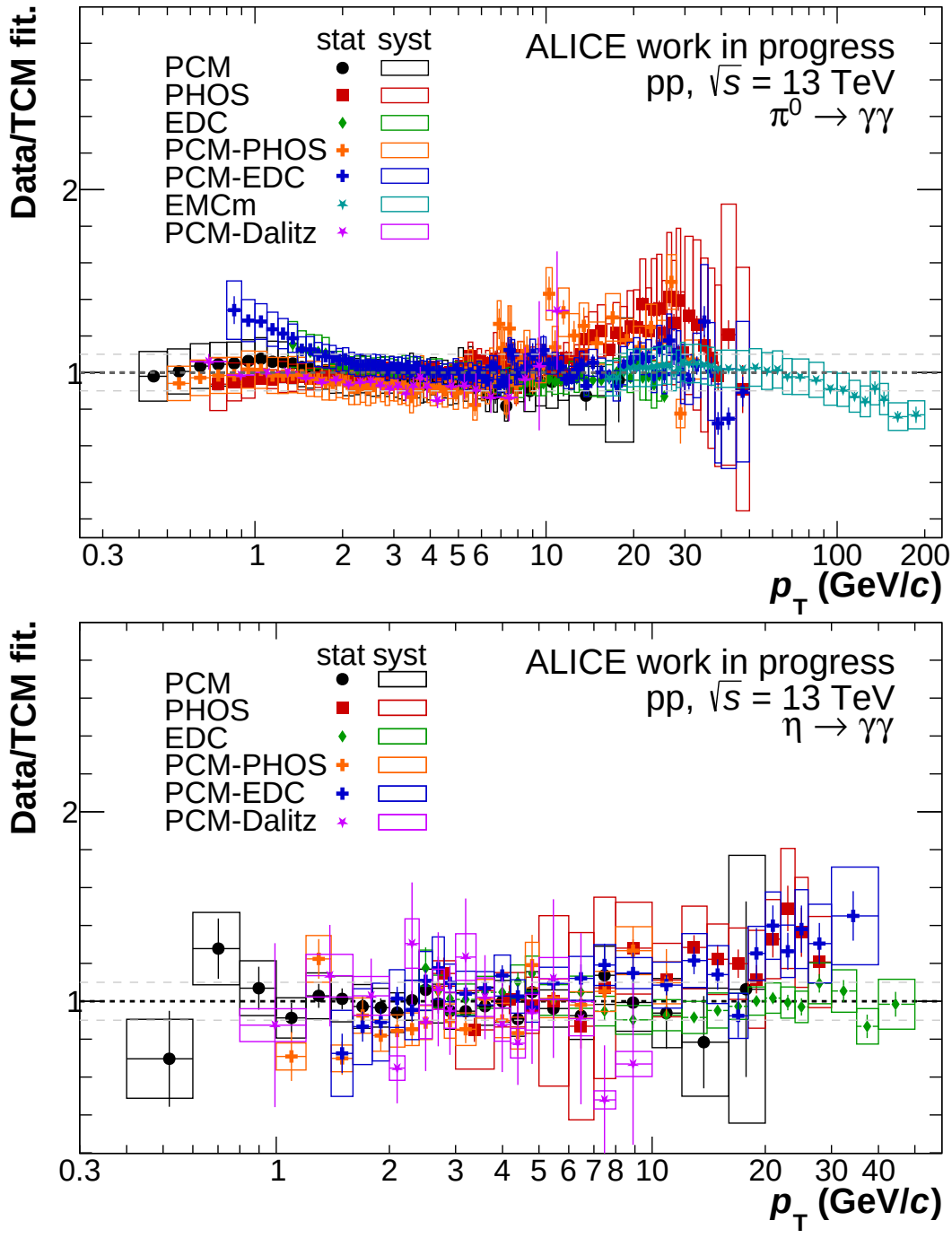

Figure 2.24.: Comparison with the different methods at $\sqrt{s}$ = 13 TeV.

Chapter 3.

Correlation, energy density and equation of state

This part of the thesis is dedicated to the analysis of experimental results of the transverse momentum distributions from ALICE and CMS. The analysis starts with kinematic variables such as transverse momentum and global ones as the multiplicity distributions. Both variables allow to explore the created matter in p+p, p+Pb, and Pb+Pb collisions; from here on, we will describe the analysis of two topics: Forward-Backward multiplicity correlation based on [48] and energy and entropy densities reported on [49].

3.1. Historical advances

Measurements in the low-momentum regime provide essential information to describe strong interactions using the non-perturbative region of Quantum Chromodynamics (QCD); QCD-inspired models are usually implemented in Monte Carlo event generators. Additionally, these kinds of measurements are used to constrain the free parameters of such models.
Furthermore, $\langle p_{\mathrm{T}} \rangle$ studies as a function of collision energy and multiplicity distributions provide more detailed information on the kinematic processes of colliding systems. Thermodynamical quantities describing the system created during the collisions are estimated using the transverse momentum of

hadrons [50].

Jet production seems to explain the increase of $\langle p_{\mathrm{T}} \rangle$ with multiplicity. Jets are responsible for the first rise since hard processes dominate over soft ones in this multiplicity region [51]. Then, a second rise seems to appear due to jet production and fragmentation; this behavior is consistent with results obtained at Tevatron energies. However, this behavior is not observed at higher energies. Moreover, the energy dependence has been studied by the CDF experiment that reported $\langle p_{\mathrm{T}} \rangle$ as a function of multiplicity for minimum bias events at 630 and 1800 GeV, showing and increase with the energy and multiplicity for central pseudorapidities. It has also been observed that $\langle p_{\mathrm{T}} \rangle$ for soft events is not energy dependent, for hard events it increases faster as the energy of the colliding system increases [52].

The behavior of $\langle p_{\mathrm{T}} \rangle$ is almost linear at low collision energies [53] it grows faster for higher energies, where it can be described using a second order logarithmic polynomial as a function of the collision energy [54, 55]. For identified charged particles the $\langle p_{\mathrm{T}} \rangle$ exhibits also a mass dependence. This behavior can not be explained [56] by the default tune of the PYTHIA event generator which overestimates ATLAS results [57] on charged particle multiplicity and transverse momentum for values larger than 40 in multiplicity, in the pseudorapidity range $|\eta| < 2.5$. Alternative models such as the Color Glass Condensate (CGC) [58], where the $\langle p_{\mathrm{T}} \rangle$ is a universal function of the ratio of the multiplicity density and the transverse area of the collision (S_{T}) [59] qualitatively reproduce the experimental data. However, this geometrical model seems to describe the $\langle p_{\mathrm{T}} \rangle$ at larger multiplicities for p+p and p+Pb collisions but fails for lower multiplicities, and neither can describe $\langle p_{\mathrm{T}} \rangle$ for Pb+Pb collisions. A possible reason for this poor description is that collective effects may be present in p+p, p+Pb, and Pb+Pb systems, since the CGC is just a geometric model, and it is not expected to reproduce the data. It is worth mentioning that in p+p collisions, it has been suggested that there are flow-like [60] effects in high multiplicity events at LHC energies.

The ALICE collaboration at the LHC has measured the $\langle p_{\mathrm{T}} \rangle$ [61] of charged hadrons from p+p collisions at energies of $\sqrt{s}$ = 0.9, 2.76, and 7 TeV in the kinematical range $0.15 < p_{\mathrm{T}} < 10.0$ GeV/c and $|\eta| < 0.3$. ALICE selected all the charged prompt particles produced in p+p collisions including all decay products, except those from weak decays of strange hadrons. The results show a correlation of $\langle p_{\mathrm{T}} \rangle$ with $\mathrm{N_{ch}}$ which is stronger for p+p than for p+Pb and Pb+Pb collisions. The observed strong correlation has been attributed within PYTHIA to Color Reconnections (CR) between hadronization strings [62, 63], which are directly related with multiple parton interactions.

Long ago, the forward-backward (F − B) multiplicity correlations were studied for different colliding systems. One of the first results in p+p collisions in the Intersecting Storage Ring (ISR) at CERN at $\sqrt{s} = 52.6$ GeV [64] was the finding of positive values for correlations. Five years later there were results of $\mathrm{p} + \bar{\mathrm{p}}$ collisions at $\sqrt{s} = 540$ GeV [65] in the Super Proton Synchrotron (SPS), also positive values of the correlation a possible dependence on the energy was reported as well. Short after, results on e^+e^- collisions at $\sqrt{s} = 29$ GeV [66] were published and the reported results showed no F − B multiplicity correlations. This result was interpreted as a consequence of the system studied, whereby the correlation is stronger in p+p and $\mathrm{p} + \bar{\mathrm{p}}$ than in e^+e^-.

The E735 collaboration at the Tevatron confirmed the dependence of the correlation with energy [67] in p+p collision at $\sqrt{s} \approx 1$ TeV. Results on heavy ions at $\sqrt{s_{NN}} = 200$ GeV published by the STAR Collaboration at the Relativistic Heavy Ion Collider (RHIC) found strong correlations [68], for the case of the most central Au+Au collisions, while for p+p collisions a small correlation was found. Recently at the LHC similar results in p+p collisions were reported by the ATLAS [69] and ALICE [70] collaborations at $\sqrt{s} = 0.9, 2.7$ and 7 TeV, where they observed strong correlations. Their analyses were more detailed, investigating the p_{T} dependence of azimuthal and pseudorapidity distributions of F − B multiplicity correlation and argue why the STAR Collaboration could not find these results.

F − B multiplicity correlation studies are more informative when decoupled into short and long range components [71,72]. Short-range correlations (SRC) are localized over a small range of η, typically up to one unit. They are induced by various short-range effects like decays of clusters or resonances, jet and mini-jet induced correlations. Long-range correlations (LRC) extend over a wider range in η and originate from fluctuations in the number and properties of particle emitting sources, e.g. clusters, cut pomerons, strings, mini-jets etc. [71–74].

Using the F − B multiplicity correlation approach, it is possible to examine string configurations and their interactions along the η-range, accessible in an experiment, and also to get rid of short-range contributions coming from resonance decays, jets, etc.

As expected, the experimental studies of long-range rapidity correlations can give us the information about the initial stage of high energy hadronic interactions [75]. It has been proposed that the study of the long-range F − B multiplicity correlations between two separated rapidity windows can provide a signature of the string fusion and percolation model [76–78] in ultrarelativistic heavy ion collisions [79].

Furthermore, the observed enhancement of $\langle p_{\mathrm{T}} \rangle$ versus multiplicity at low p_{T} is not reproduced by any model [55]. These kinematic and global observables have been associated in simulation studies to QGP formation in proton-proton collisions [80]. The relationship between multiplicity and multiple parton interactions [81] has been studied in an attemp to explain experimental results. An incoherent superposition of such interactions would lead to a constant $\langle p_{\mathrm{T}} \rangle$ at high multiplicities.

In high multiplicity p+p events, a medium governed by strong interactions is produced [82], thus, the produced matter can be described in terms of quark and gluon degrees of freedom. The equation of state, relating the energy and entropy densities, pressure, and temperature of such matter, is of fundamental impor-

tance to understand its composition and the static and dynamical properties of the medium created in p+p, p+Pb and Pb+Pb collisions at different energies.

3.2. Forward-Backward multiplicity correlations

Multiplicity fluctuation show a F − B multiplicity correlations defined by:

$$b_{Corr}(\delta\eta) = \frac{\langle n_F n_B \rangle - \langle n_F \rangle \langle n_B \rangle}{\langle n_F^2 \rangle - \langle n_F \rangle^2}, \tag{3.1}$$

where n_F and n_B is the charged particle multiplicities in two symmetrically located $\delta\eta$ pseudorapidity bins, separated by a central pseudorapidity gap, $\Delta\eta$. The strength of the correlation factor, b_{Corr}, is sensitive to changes of multiplicity. For example, the computed values of b_{Corr} for ranges of multiplicity produce negative values. This result is a consequence of the definition, but has no physical meaning. In the case of events with multiplicity larger than zero but limited from above, the b_{Corr} is well defined, this will be discussed in the next section.
The main variable to describe the b_{Corr} is the multiplicity distribution. It is well known that the evolution of this distribution is adequately described by the negative binomial distribution [83]. In fact, in order to describe the multiplicity distribution, the number of multiple particle interactions in an event was introduced. Evidence of the importance of this variable has been reported by the experiments [84] through the broadness of the multiplicity distribution. From the theoretical side, there are calculations [85] that have been included in the PYTHIA event generator. This research area has gained more interest given that its development [86] helps to understand the non-perturbative QCD processes and could also be related to physics at the LHC energies.

The forward-backward multiplicity correlations can be studied as a function of pseudorapidity (η) for windows of width $\delta\eta$, symmetrically around pseudorapidity $\eta = 0$, and also as a function of the pseudorapidity gap (η_{gap}) between the two $\delta\eta$. Experimental results of the F − B multiplicity correlations show

a common trend: they increase with increasing bin width of pseudorapidity. One obvious interpretation would be that for small bin widths, the statistic fluctuations play a more significant role, diluting the correlation strength. This asseveration has been verified by computing the F − B multiplicity correlation with a toy model. However, the shape of this correlation does not fit the data, and there is no way to modify it. Nevertheless, it is essential to remember that hard QCD processes dominate particle production in the central pseudorapidity region and that in the forward region, soft processes increase and become more important than hard ones. Therefore F − B multiplicity correlations are more complex than just fluctuations of particles in bin size of pseudorapidity, which are used to report the correlation. We examine the correlations for central and forward pseudorapidity bins.

3.2.1. Characterization of the Forward-Backward Correlation

Resonances, as mentioned before, allow to decouple the short and long range correlations. It is then important to look for the effects on b_{Corr}. The upper panel of Fig. 3.1 shows the b_{Corr} for central (two upper distributions), $|\eta| < 1$ and forward pseudorapidity (two lower distributions) ranges, $3 < |\eta| < 4$, with and without weak decays, the last one computed only with primary particles, as is usually reported by experiments. The b_{Corr} computed shows large effects of weak decays at low $\delta\eta$, where short range correlations have larger contributions compared to long range pseudorapidity correlations where there are not contributions from weak decays. These effects are reduced when $\delta\eta$ increases, as show by the ratios on the middle and the bottom panel.

The differences between these results raise the possibility to explore phenomenological aspects on non-perturbative QCD processes and their effects on the b_{Corr} when the calculation is done for low p_{T}. On the contrary, b_{Corr} for high p_{T} particles is related to the perturbative QCD regimen and then it is possible to explore effects on b_{Corr} from minimum bias experimental results, and or jets, for instance. Fig. 3.2 shows the b_{Corr} for soft and Fig. 3.3 hard processes, each one for two

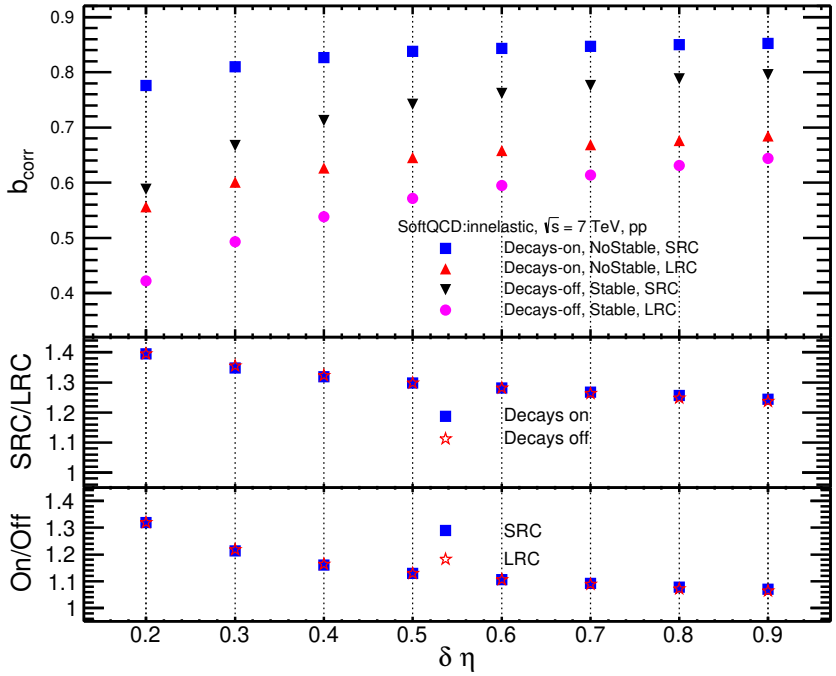

Figure 3.1.: Correlations with and without weak decays for short and long range correlations. The middle panel shows the ratio of b_{Corr} with to without weak decays. Bottom panel shows the ratio of b_{Corr} for central to forward pseudorapidity multiplicity distributions.

η ranges, as indicated in the figure. Higher values are observed from soft with respect to those from hard processes. One can observe that b_{Corr} decreases when η goes from the central region, where short range correlation (SRC) are expected, to large η values were long range correlations (LRC) are expected. In each of the bottom panels the ratio LRC to SRC is plotted, where it is observed an almost scaling behavior of the b_{Corr} for soft processes, while for hard processes the ratio increases. It is then important to attribute the change of the slope of b_{Corr} to hard processes. Let us emphasize that for our calculations hard QCD processes are those whose transferred transverse momentum ($\hat{p}_{\mathrm{T}}$) between interacting partons is larger than 30 GeV, so that we guaranty really hard events.

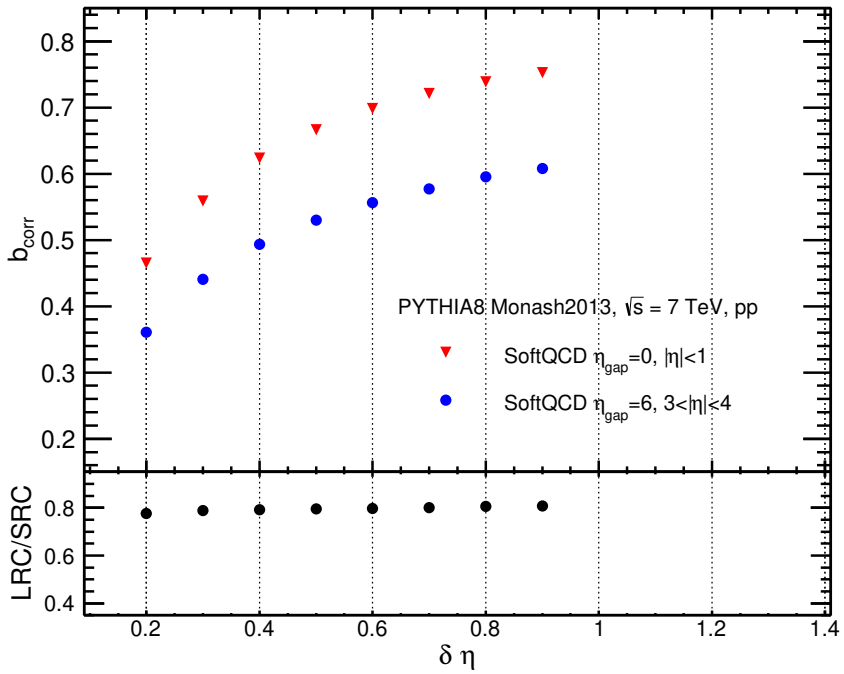

Figure 3.2.: Correlation factor for p+p collision at $\sqrt{s} = 7$ TeV for soft QCD processes, showing results for central and fragmentation pseudorapidity regions, and the ratio LRC to SRC strength correlations

3.2.2. Colour reconnection and multiple parton interaction

Another crucial contribution to the F − B multiplicity correlations is produced by the Colour Reconnection (CR) discussed in Appendix. A.5. It is well known that CR reduce the average multiplicity distribution and as a consequence, it should produce a decrease of the b_{Corr}. Figure 3.4 shows the ALICE data compared to b_{Corr} with and without CR where one can observe that an increase of the strength of CR produces a decrease on the F − B multiplicity correlations. The values used in Fig. 3.4 for the strength of CR are 0 (NCR in the figure), 1.4 and 10 (CR R in the figure), but none of them agrees with the data. The correct values could be found by an experimental data fit.

One of the main points to explore with the correlation was calculating an indirect value of multiple parton interactions. Studying the evolution when CR and the number of MPI are taken into account. Separately, an increase on the number of

MPI produces an enhancement of the b_{Corr}, however, an increase of the strength of the CR reduces the b_{Corr}, so we need to extract simultaneously the strength of both effects. The upper panel of Fig. 3.5 shows our simulation of b_{Corr} at 7 TeV while the bottom one shows b_{Corr} at 13 TeV, each of them for three sets of cuts on the average number of MPI and CR values of 0.9, compared to data at 0.9 and 7 TeV. The best range of values of the multiple parton interactions are $2 \leq \mathrm{MPI} \leq 4$ to describe data at 0.9 TeV and $6 \leq \mathrm{MPI} \leq 10$ for data at 7 TeV.

Following the behavior of the multiple parton interaction distributions the upper panel of Fig. 3.5 shows our results of the b_{Corr} at 7 TeV in the range $6 \leq \mathrm{MPI} \leq 10$ extracted from a fit of ALICE data at 7 TeV. It is worth noting that the same range of the number of MPI but computed at 13 TeV can also reproduce data at 7 TeV (bottom panel of Fig. 3.5), which is not exactly but is close to the case of data at 0.9 TeV, showed in both panels. This number of MPI

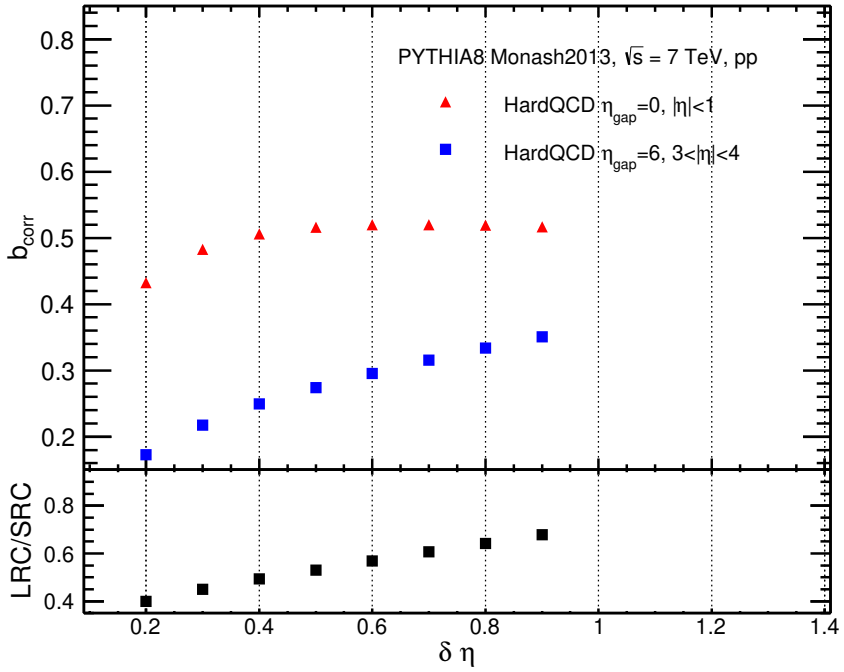

Figure 3.3.: Correlation factor for p+p collision at $\sqrt{s} = 7$ TeV for hard QCD processes, showing results for central and fragmentation pseudorapidity regions, and the ratio LRC to SRC strength correlations

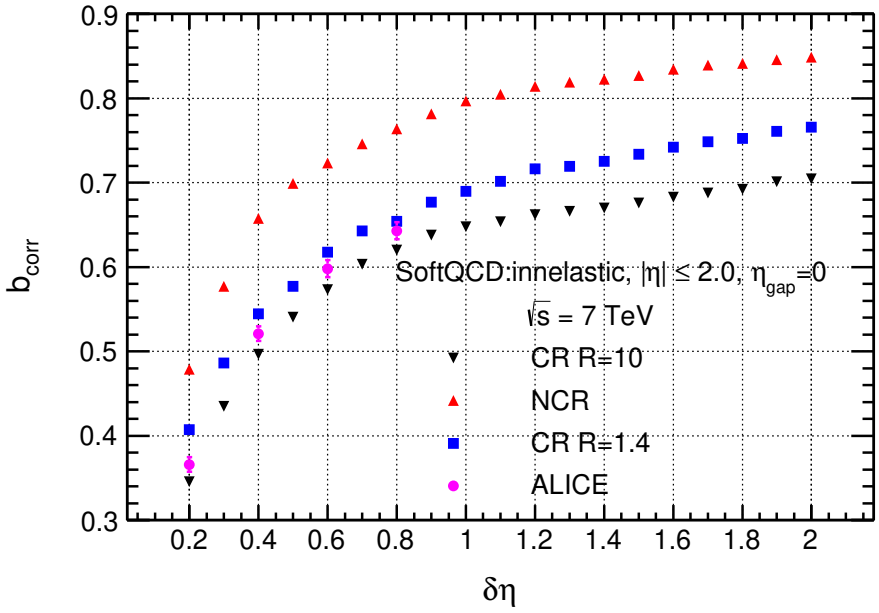

Figure 3.4.: b_{Corr} for p+p collisions at $\sqrt{s} = 7$ TeV for two values of CR and without it.

corresponds roughly to the separation point of the distributions at 0.9 and 7 TeV, 7 and 13 TeV. This could be a coincidence but following this trend of the number of MPI distributions, b_{Corr} for the average number of MPI in the range: $10 \leq \mathrm{MPI} \leq 12$ could correspond to data at 13 TeV. However, the plot shows results for the average number of MPI ≥ 10 which is $\sim 7\%$ higher than the ALICE data.

This last distribution computed at 13 TeV is $\sim 3\%$ larger than those obtained at 7 TeV. Then, considering the possibility to extract the strength of color reconnection, for instance in average transverse momentum [87], one can use the $\mathrm{F} - \mathrm{B}$ multiplicity correlations strength to extract the average number of MPI event classes. The previous procedure allows to get the average number of MPI, and not the number of event-by-event interactions. Furthermore, the procedure to get our results is model depend since we are using one specific multiple parton interaction model, and even more, the color reconnection is not completely independent of the multiple parton interaction models.

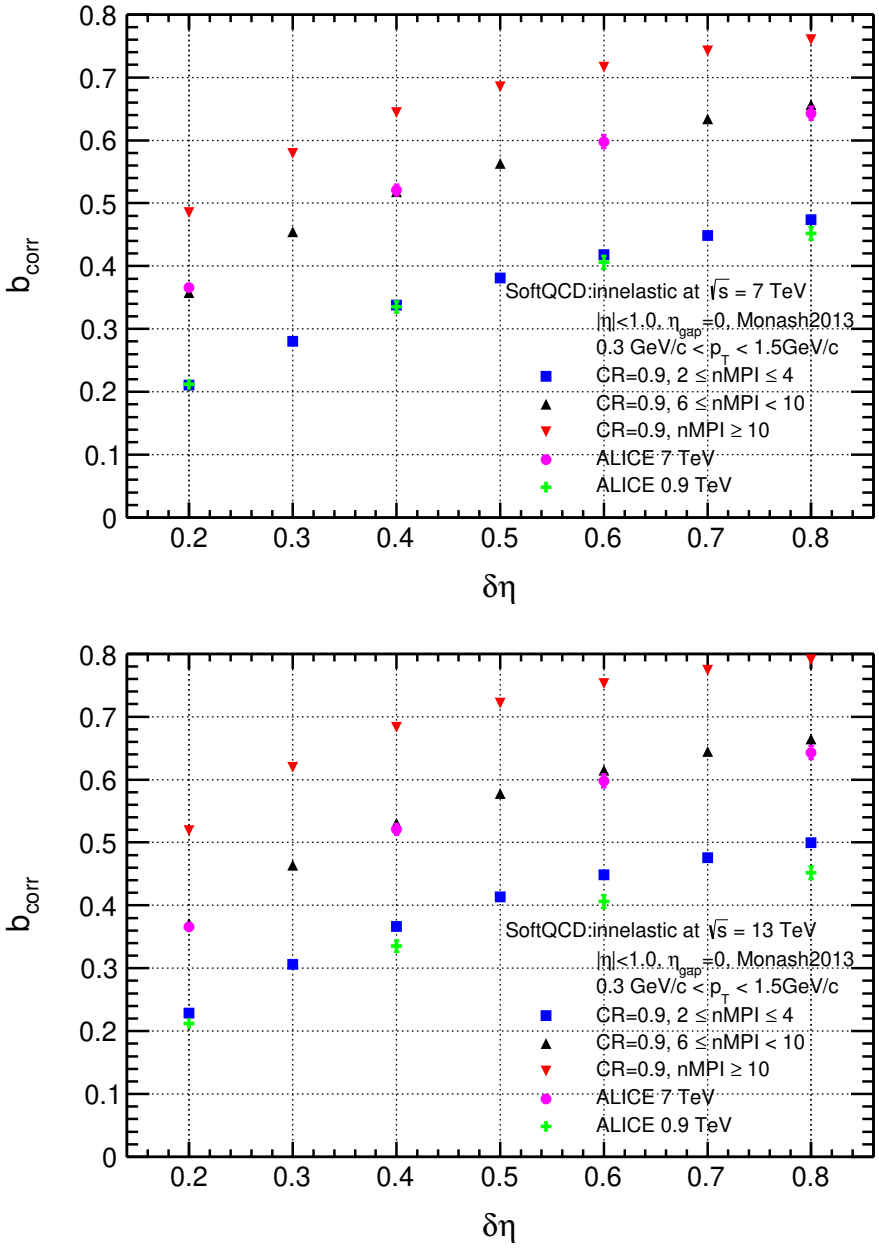

Figure 3.5.: The correlation factor in terms of ranges of MPI and CR for p+p collision at $\sqrt{s} = 7$ TeV (upper) and 13 TeV (bottom), compared to ALICE data at 0.9 and 7 TeV.

It is also important to emphasize that we can make an extrapolation of the b_{Corr} to different energies and their correspondent number of MPI. Specifically,

the ALICE data of the Fig. 3.5 at 0.9 TeV are fitted with a function $b_{\mathrm{Corr}} = a + b\ ln\sqrt{(\delta\eta)}$ where $a = 0.49$, $b = 0.17$ and with this parametric function scaled by a factor 1.36, one gets a correlation distribution very close to those for data at 7 TeV. It is worth noting that the distribution of b_{Corr} for lower MPI computed at 13 TeV presents the larger differences at higher values of $\delta\eta$, which can be associated to hard processes, according to the previous discussion.

The previous results based on PYTHIA are computed incorporating color reconnection combined with multiple parton interactions to describe the data, thereby one can see the importance of the final state effects, and in general, the phenomenology of non-pQCD reached in the experiment. The energy dependence has also been observed, then knowledge of the relationship among the b_{Corr}, MPI and CR brings the possibility to get insight into the rich phenomenology of the soft QCD process.

3.2.3. Correlation and Jets

A jet is defined as multiple collimated particles (hadrons) created by the hadronization of quarks or gluons produced in lepton-lepton, lepton-hadron, hadrons-hadrons, or heavy-ion collisions. Figure 3.6 illustrate the topology of the jet cone, where the hadrons inside a phase space defined by a cone with radius $R = \sqrt{\Delta\eta + \Delta\phi}$, belong to a jet. The probability to have certain number of jets depends on the different initial condition of the collision. The present analysis uses the size of the cone radii of 0.3, 0.5, 0.7 to study effects of these conditions. The minimum threshold energy of 700 MeV was taken. The cell jet algorithm is simple enough to make an analysis, but weakness since it is insensitive to the topology of the events (di-jets) and its surroundings.
Figure 3.7 shows the probability distribution for the event multiplicity divided by ranges of the number of jets with and without CR. Here, we can observe how the mean multiplicity is related to the number of jets, and CR shows the same behavior as explored previously. The bottom plot shows the ratio of CR, and without CR in the range of the same number of jets, the results indicate how at

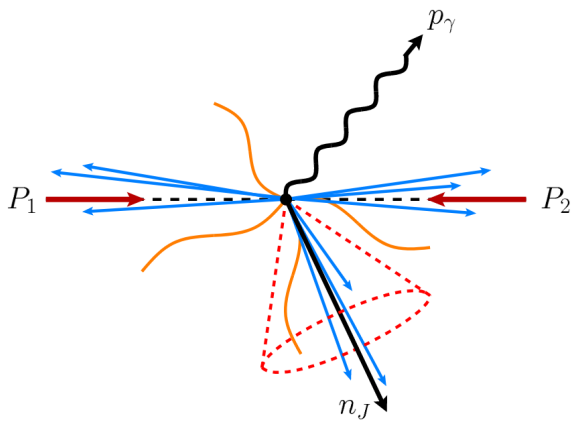

Figure 3.6.: Jet topology illustrating a jet cone.

higher multiplicity, the effect has an exponential behavior, meaning CR has a high dependence on the number of jets.

Regarding the correlation Fig. 3.8, b_{Corr} shows a high correlation for a small number of jets; this indicates that higher multiplicity did not mean higher correlation; ranges 1 to 3 have the di-jets or back-to-back jets, meaning symmetric events. For CR ratios, the more significant difference is for small $\delta\eta$ ranges.

Ongoing work

Last results, we are investigating the ratio of the mean of nMPI and nJets; Figure 3.9 shows the particular ratio in terms of the energy inside the jets as a function of multiplicity; the idea behind this figure is to explore a direct correlation between nMPI and nJets. The more energy inside the jet, the curve becomes flatter, implying that the nMPI is sensitive to the nJets.

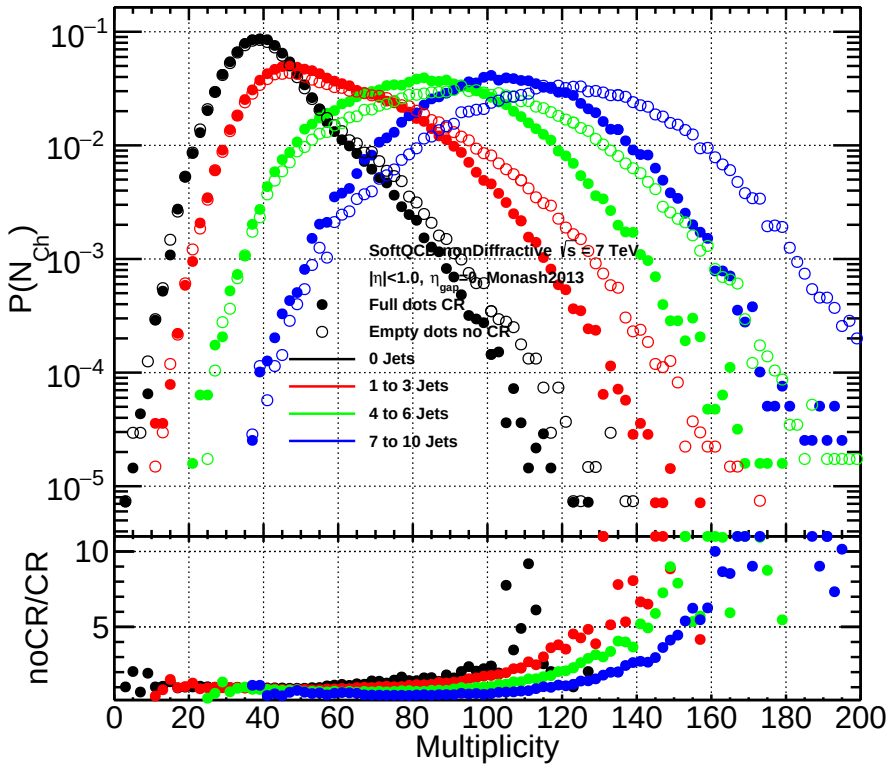

Figure 3.7.: Multiplicity distribution with and without CR as a function of number of jets.

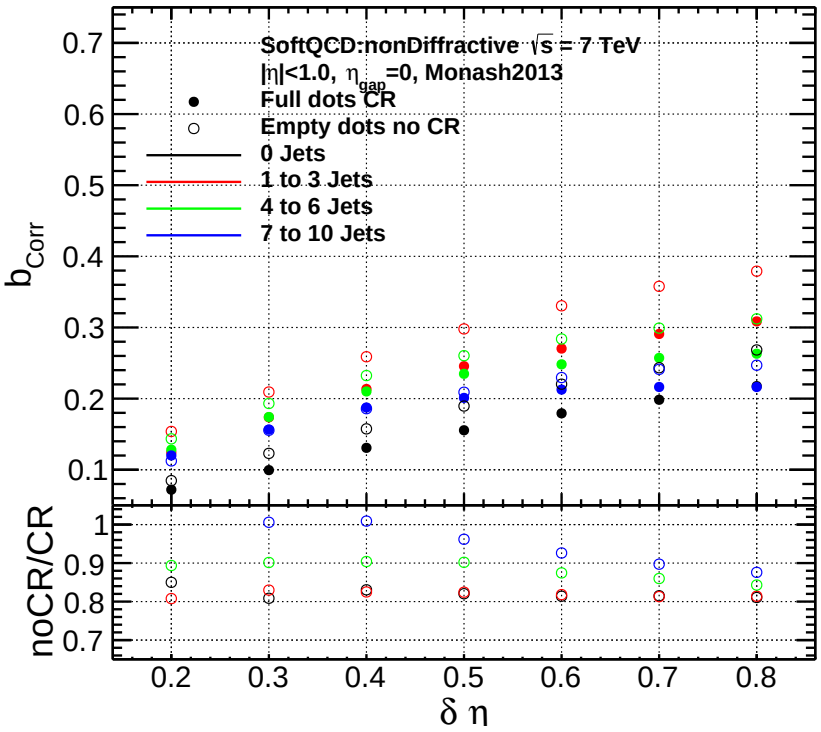

Figure 3.8.: b_{Corr} for ranges of number of jets with and without CR

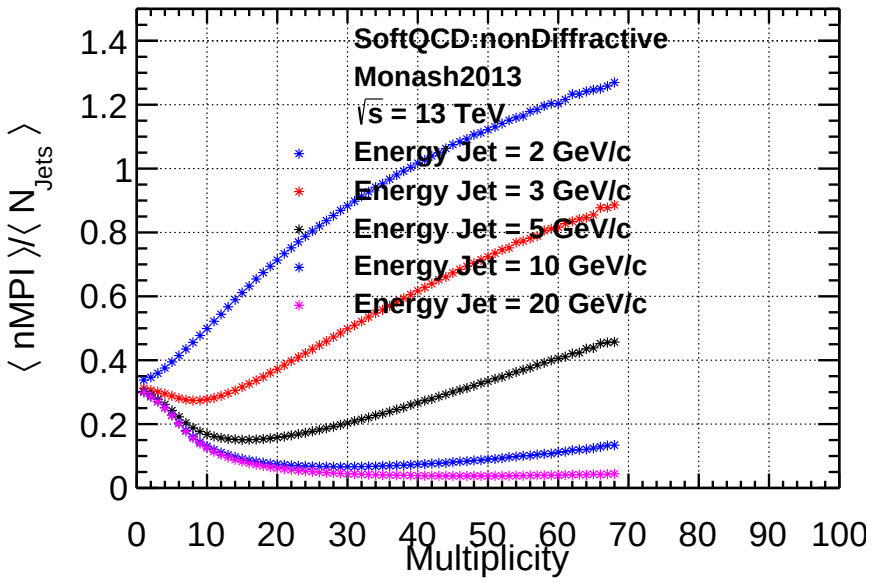

Figure 3.9.: Mean nMPI divided by mean number of jets in function of the energy in the jet for 13 TeV.

3.3. Multiplicity and mean momentum

The correlation between multiplicity and transverse momentum has been studied since the 80's [88]. The experimental results on multiplicity suggested the introduction of the multiple parton interaction (MPI) [89]. Since then, nMPI was introduced in the event generators as an ingredient to describe hadronization processes, together with the string fragmentation mechanism within the Lund model [90].

3.3.1. Average transverse momentum and multiplicity

Figure 3.10 shows the average multiplicity distributions versus transverse momentum generated with PYTHIA for p+p collisions without CR at different energies in the range from 0.01 to 13 TeV (Fig. 3.10a). The distributions at the lowest energy, 10 GeV, shows a flat behavior; meanwhile, as the energy increases, a rising slope appears, which can roughly be described by $< N_{\rm ch} >= a + b \cdot p_{\rm T}^{c}$, where a, b and c are free parameters. When the energy increases $< N_{\rm ch} >$ does as well, similarly to the charged particle density. The exact shape of the average multiplicity is illustrated by looking at the ratio between average multiplicity for two energies: $< N_{\rm ch} > (E_n)/ < N_{\rm ch} >$ (E=13 TeV), where $E_n = 0.01, 0.9, 2.76$ and 7 TeV (Fig. 3.10b). Fig. 3.10c shows the ratio of the average multiplicity without CR effect to that where it is included. The ratio shows a more prominent difference at higher energy. For instance, at 13 TeV, the ratio is reduced down to $\approx$ 20% when $p_{\rm T}$ goes from $\sim$ 0.5 to $\sim$ 3.0 GeV/c. The distributions above 3 GeV/c become flat. The CR effects tend to vanish when the energy decreases, producing a null effect at 10 GeV. These results are presented as a function of the momentum but they also have a dependence on the intensity of the CR, described in Eq. (A.1). The transverse momentum distribution experiences a flow-like effect due to CR [91,92] in PYTHIA, and it is observed in p+p collisions at CMS [60] resembling the distributions observed in heavy ion collisions, where hydrodynamics describes the data qualitatively.

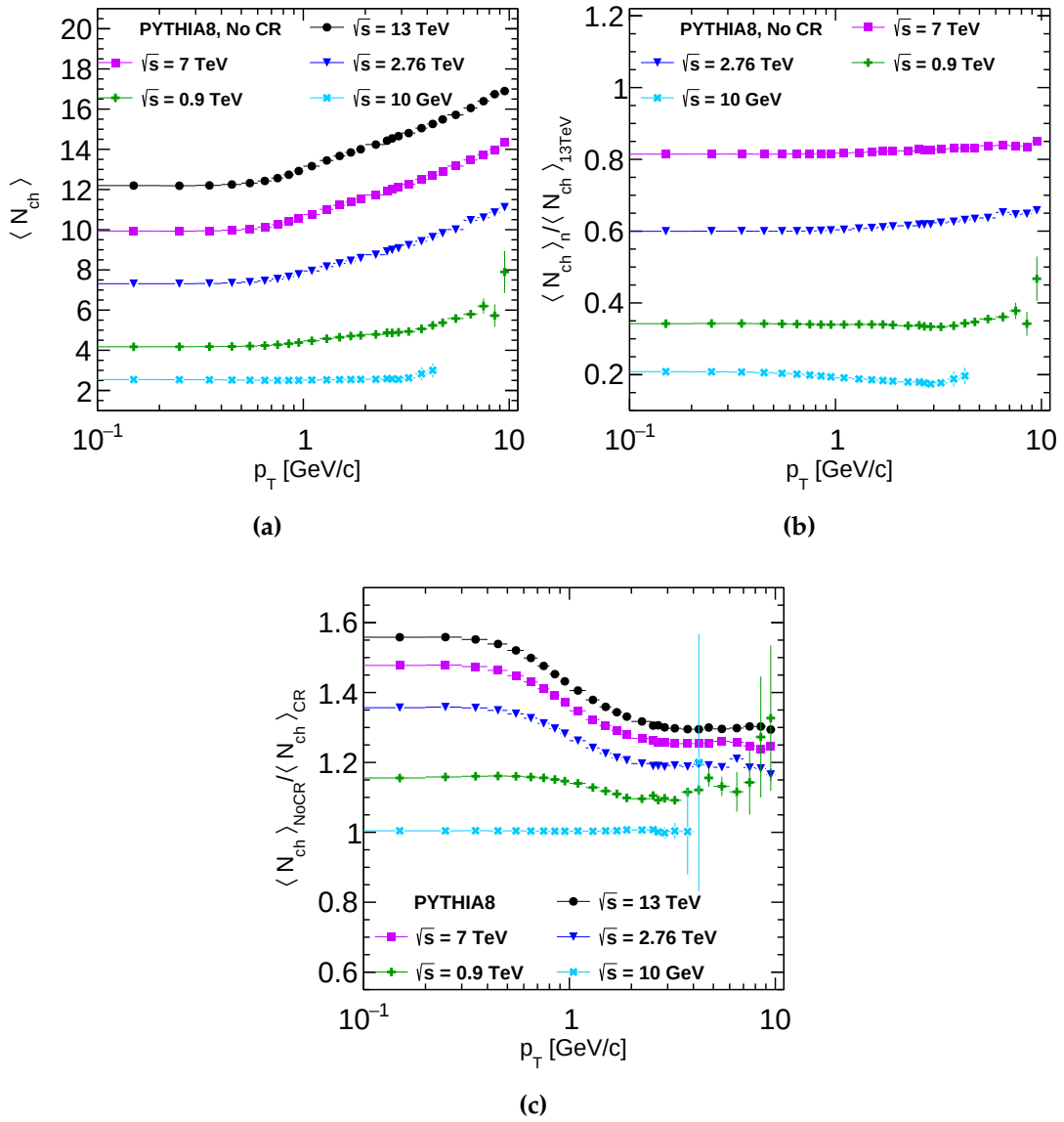

Figure 3.10.: Average multiplicity distributions as a function of transverse momentum (a) without CR. Ratios of the average multiplicities at two energies (b), and ratios between the average multiplicity at the same energy but without to with CR (c).

The distributions in Fig. 3.11 are equivalent to the ones shown in Fig. 3.10 but computed with the EPOS event generator where fusion and no fusion models were considered instead of CR or no CR included in PYTHIA. Both Fig 3.10a

and 3.11a are very similar, nonetheless in 3.11b, EPOS produces a flat ratio for 10 GeV whereas PYTHIA produces ratios that go down and then up. The ratios of the $< N_{\rm ch} >$ given by fusion off to fusion on models (Fig. 3.11c) show a slight and constant decrease with increasing energy and for $p_{\rm T}$ larger than $\sim$ 0.5 GeV/c, the ratios decrease except for the case of 10 GeV which remains constant within uncertainties. Comparing EPOS fusion and PYTHIA CR, the first predicts a slight reduction on the $< N_{\rm ch} >$ whereas the second reduces the $< N_{\rm ch} >$ up to $\sim$20% for higher energy when $p_{\rm T}$ goes from 0.0 - 10 GeV/c.

As mentioned in Sec. A.1, the impact-parameter could modify some kinematic variables like the average transverse momentum versus multiplicity. Fig. 3.12a shows slight differences in the distributions of the impact-parameters for p+p collisions incorporated in two event generators, EPOS and PYTHIA. The differences come from the different models to describe the matter distribution of the colliding hadrons and the set of parameters used to fit data. EPOS uses PYTHIA 6 with default tune, whereas PYTHIA 8 has a different tune and includes several new functions [93] for a better description of kinematical variables.

Our analysis considers the effects on $\langle p_{\rm T} \rangle$ versus multiplicity for two event generators: for the case of PYTHIA with CR, one gets the distributions in Fig. 3.12b compared to ALICE data [61], where it is shown that different ranges of impact-parameter produce a slight change in the slope of the $\langle p_{\rm T} \rangle$. Variation in the ranges on the impact-parameter, by themselves do not allow the reproduction of data, and this worsens for low multiplicity, overestimating up to $\sim$7% for the impact-parameter range of $0.0 < b < 0.2$ fm, whereas for events with high multiplicity, the statistical errors are large enough to cover the disagreement. Similar variations on the impact-parameter are applied to EPOS event generator, resulting in a great description of data for the range of $0.0 < b < 0.2$ fm. EPOS includes hydrodynamical effects; however, kinematic observables from these event generators in hadron-hadron collisions are not the same, nor do they look like the PYTHIA results discussed in the previous lines.

This last one includes flow-like effects in hadron-hadron collisions, resembling hydrodynamical effects, but clearly, we can not give a hydrodynamical treatment using this event generator. Fig. 3.13a shows the average transverse momentum versus multiplicity for charged hadrons produced in p+p collisions from two-

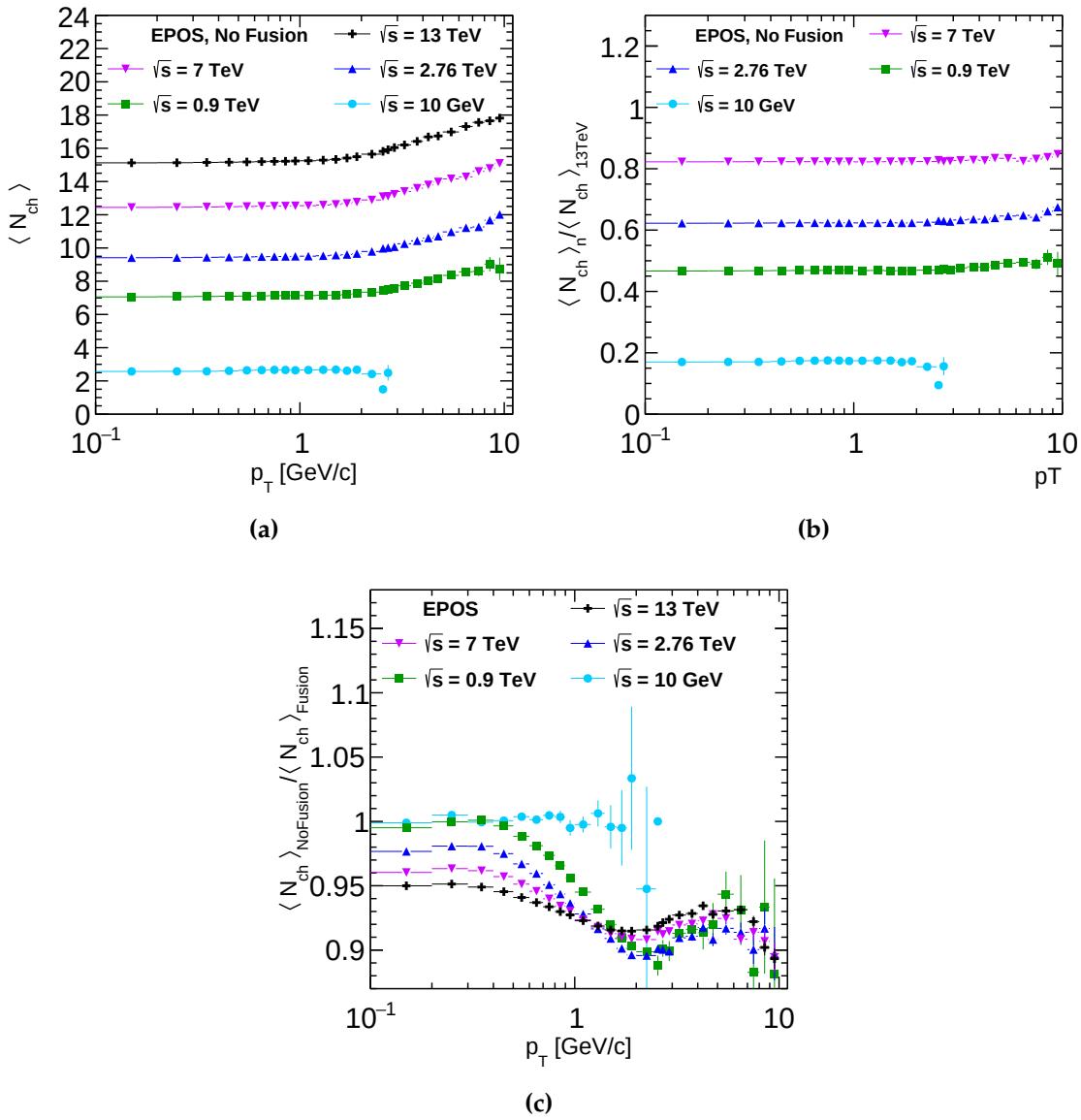

Figure 3.11.: Average multiplicity distributions as a function of transverse momentum (a). Ratios between average multiplicities for two energies (b), and ratios between average multiplicities for two models at the same energy (c).

event generators: PYTHIA without CR and EPOS with fusion turned off. These results show a discrepancy for all p_T ranges.

The same distributions with flow or hydro effects are shown in Fig. 3.13b together with ALICE data. There is a good agreement between data and EPOS

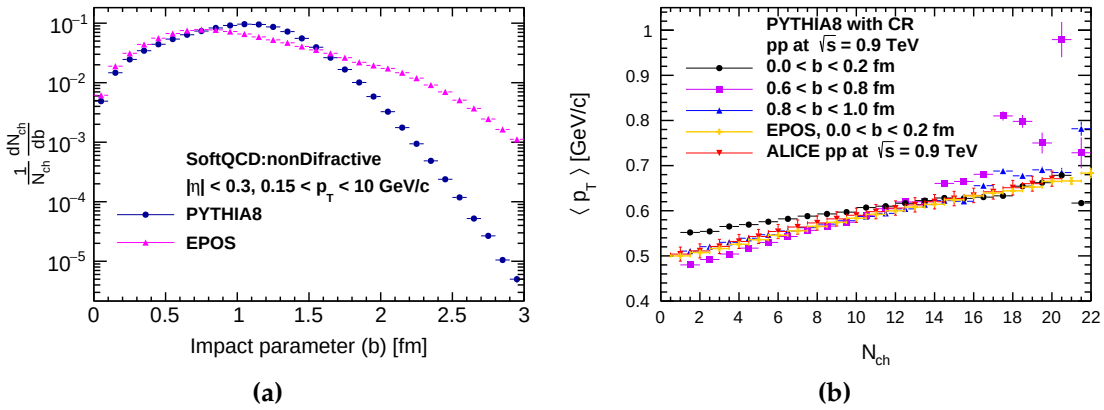

(a) (b)

Figure 3.12.: Impact-parameter distributions, from the EPOS and PYTHIA event generators (a), and average transverse momentum as a function of the multiplicity for three ranges of impact-parameter for the PYTHIA case and one range of EPOS, compared to ALICE data [61] at 900 GeV (b).

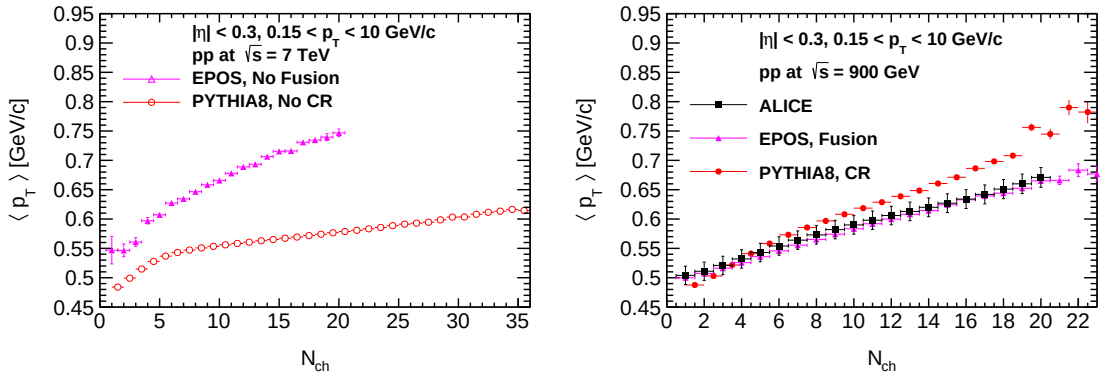

(a) (b)

Figure 3.13.: Comparison of the average transverse momentum versus multiplicity for two event generators without (a) and with (b) hydro and CR of 1.8 is considered at 900 GeV. ALICE data [61] also are showed in the (b) panel.

for all multiplicity ranges. Nevertheless, PYTHIA with CR shows an increasing disagreement as the multiplicity increases; besides the model dependency, there is a dependence on energy and the hardness of the process incorporated in each model. PYTHIA and EPOS event generators have many parameters which can usually be modified to create a tuning to fit experimental data. Our results of $\langle p_{\mathrm{T}} \rangle$ are without tuning but are computed for different impact-parameter

ranges, which according to section A.1, could give insight into the hadronic matter distribution in the proton beam.
Fig. 3.14a shows results in agreement among PYTHIA, EPOS and ALICE data at 900 GeV. Results from EPOS considered a range of impact-parameter from 0.0-0.3 fm, for larger impact parameter ranges, It overestimates by $\sim$9% at low multiplicity. An agreement between models and data is also observed for $\langle p_{\mathrm{T}} \rangle$ versus multiplicity at 7 TeV [61], showed in Fig. 3.14b, where PYTHIA results were generated with CR parameter of 1.3 instead of 1.8, to improve the agreement with data up to 6% for multiplicity below 25, at least for the $\langle p_{\mathrm{T}} \rangle$ from p+p at 7 TeV. At higher multiplicity the agreement worsens. Results have been tested at different energies but in this work we only show results for 0.9 and 7 TeV. We also tested for p+Pb and Pb+Pb systems with colliding energies of 5.02 TeV and 2.76 TeV, respectively. These comparisons are complementary to those reported by ALICE [61].

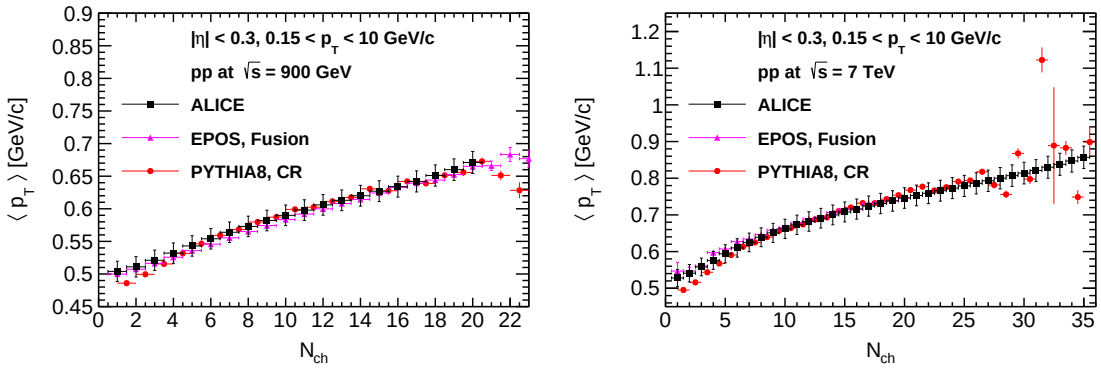

Figure 3.14.: Comparison of the average transverse momentum versus multiplicity for two event generators and ALICE data [61] at 0.9 TeV (a), and 7 TeV (b).

The average transverse momentum for charged hadrons as well as for identified particles has been measured in different colliding systems, since it provides a more detailed understanding of the dynamics of the collisions, like the mass dependence or quark content. The results clearly show that $\langle p_{\mathrm{T}} \rangle$ presents the most significant slope for higher mass particles, and gets significantly smaller for the lightest particles [56].

The average transverse momentum as a function of the multiplicity scaled by the transverse area has been proposed as a good scaling law at high multiplicity but not at lower ones. The study of this scaling requires knowledge of interferometry to extract the size (radius) of the matter created in p+p, p+Pb, and heavy-ion collisions. These techniques were used by ALICE [94] and CMS [95] to extract the radius as a function of the particle multiplicity. The multiplicity distributions normalized to the transverse area (S_T) of the collisions (N_{ch}/S_T) is an excellent variable to explore $\langle p_{\mathrm{T}} \rangle$ in hadron collisions. The CMS measurements of the multiplicity allows the parametrization of the radius for p+p and p+Pb collisions as follows [96]:

$$R_{pPb,pp} = 1fm \times f_{pPb,pp}\left(\sqrt[3]{dN_g/dy}\right) \tag{3.2}$$

$$\frac{dN_g}{dy} \approx K\frac{3}{2}\frac{1}{\Delta\eta}N_{tracks}, \tag{3.3}$$

where dN_g/dy is the gluon density and

$$f_{pp}(x) = \begin{cases} 0.387 + 0.0335x + 0.274x^2 - 0.0542x^3 & \text{if} \quad x < 3.4 \\ 1.538 & \text{if} \quad x \geq 3.4 \end{cases} \tag{3.4}$$

$$f_{pPb}(x) = \begin{cases} 0.21 + 0.47x & if \text{ x} < 3.5 \\ 1.184 - 0.483x + 0.305x^2 - 0.032x^3 & \text{if} \quad 3.5 \leq x < 5.0 \\ 2.394 & \text{if} \quad x \geq 5.0 \end{cases} \tag{3.5}$$

where N_{tracks} is the number of tracks and $\Delta\eta$ is the pseudorapidity range where the experiment performed its measurements. $K = 1$ in our case. Fig. 3.15a shows the radii as a function of the multiplicity computed from Eqs. (3.4) and (3.5) for p+p and p+Pb collisions, respectively, with the multiplicity from ALICE p+p, p+Pb, and Pb+Pb colliding systems [61], and compared to CMS p+p [97] and p+Pb [98] results. The parametric distribution measured directly from ALICE [94] has also been presented for the case p+p and p+Pb. It corresponds

to the lower distribution in the plot 3.15a. An agreement at low multiplicity is observed, but the radius increases faster with the multiplicity for the heaviest systems. As it will be discussed later, these differences bring consequences in other calculations, such as energy density and entropy density. The average transverse momentum also presents a scaling law when it is plotted as a function of multiplicity scaled by the transverse area. Fig. 3.15b, shows the comparison among results from ALICE p+p at 7.0 TeV and PYTHIA with CR and EPOS with fusion turned on, at the same energy. Results from ALICE p+Pb at 5.02 TeV are compared to EPOS simulations at the same energy. These scaling laws with experimental data were studied [96] in the framework of CGC, suggesting that no scaling is present at low p_{T} due to flow effects. Nevertheless, our simulated results include flow, showing that the breaking of scaling still remains.

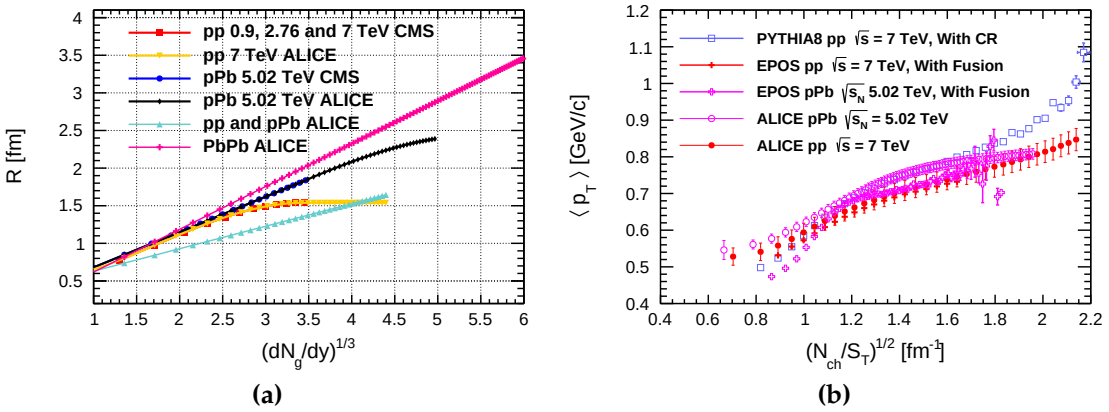

Figure 3.15.: Radii as a function of multiplicity according to parametric function [59], comparing results from ALICE data [61,94], CMS p+p [97] and p+Pb [98] data (a). Average transverse momentum as a function of multiplicity normalized by transverse area (b), comparing results from ALICE experiment [61] and simulation from PYTHIA and EPOS event generators.

3.4. Experimental equation of state in p+p and Pb+Pb collisions

Thermodynamical quantities like energy and entropy densities, temperature, and pressure, are related by an equation of state to describe the evolution of the medium created in heavy-ion collisions and also in high multiplicity p+p events. Hydrodynamic theory has been used to get the energy density, entropy, temperature and other quantities as a first description approach to p+p collisions [99]. Different observables are analyzed to explore the formation of QGP-droplets in p+p collisions [100]. The HotQCD Collaboration has developed an equation of state in (2+1) flavor QCD [101] which gives a prediction for the energy density divided by temperature T^4 (ϵ/T^4) as a function of T. Similar results have been obtained [102] using the Color String Percolation Model, which allows to compute hydrodynamical properties [50] in p+p, p+Pb and Pb+Pb collisions.
Analyzing data from the p+p and p+$\bar{\text{p}}$ collisions, the equation of state can be estimated [103] by combining $\langle p_{\text{T}} \rangle$ versus multiplicity distribution measurements. Results from heavy-ion collisions can be well described by hydrodynamics, however, this theory does not apply to results from p+p collisions. Nevertheless, p+p collisions at high energy produce a high particle density, and the mean free path of particles in such a system is very small compared to its dimension. The created system expands, and a fraction of the expansion processes must have hydrodynamical characteristics. Under this consideration the initial entropy density estimated by Landau [104] is proportional to the multiplicity ($s_0 = k dN_{ch}/d\eta$, where k is a constant) which allows to compute the entropy [105] for a mini-QGP system. Statistical models can be used to analyze the multiplicity densities and then get thermodynamical limits, in p+p collisions. In particular, the ϵ/T^4 as a function of multiplicity tends to the same value [106] when it is calculated from different statistical ensembles. The shear viscosity, isothermal compressibility and speed of sound have also been calculated [107] from ALICE p+p results.
This work presents the extraction of the thermodynamical properties from CMS and ALICE data, starting from the average transverse momentum as a function of multiplicity. At the same time, the results are compared to those from event generators.

The Bjorken energy density (ϵ_{Bj}) [108] defined by Eq. (3.6) has been used to show that the enhancement of the strangeness production as a function of energy density for different colliding systems presents a scaling law [109,110].

$$\epsilon_{Bj} \simeq \frac{3}{2} \frac{\langle p_T \rangle \frac{dN}{d\eta}}{S_T \cdot \tau}. \tag{3.6}$$

In this equation, S_T is the interaction area calculated as in the previous section, and τ is the proper time in the Bjorken model, so the product $S_T \cdot \tau$ is the volume occupied by the particles. Using Eq. (3.6), we compute the energy density for charged hadrons from p+p, p+Pb, and Pb+Pb data at different energies measured by ALICE. The results as a function of the multiplicity scaled by S_T are shown in Fig. 3.16a, where a clear scaling law is observed at low multiplicity for all colliding systems. At high multiplicity, the energy density shows differences that may come from the measured radii. Analysis of the energy density for identified particles produced in p+Pb is shown in Fig. 3.16b, where higher values for the heaviest particles are evident. It is possible to add the energy by particle species and the total approximately corresponds to the results for all charged hadrons.

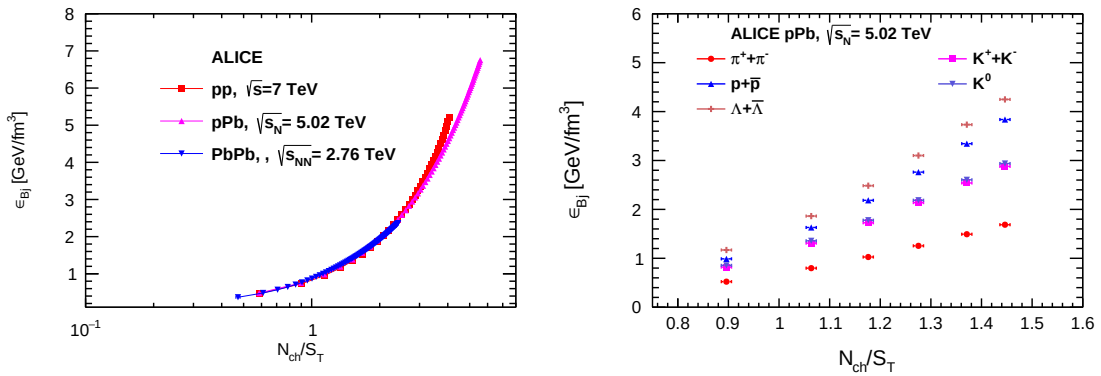

(a) **(b)**

Figure 3.16.: Bjorken energy density for charged hadrons (a) from different colliding systems and energies as a function of multiplicity scaled by the overlap transverse collision area for ALICE data [61]. The same quantity for identified particles from ALICE data [111] is shown in panel (b).

The entropy density (σ) is determined in statistical QCD with dynamical quarks [112] as:

$$\sigma \approx \epsilon_{Bj}/\langle p_{\mathrm{T}}\rangle, \tag{3.7}$$

where the initial Bjorken energy density is given by Eq. (3.6). This means that the entropy density only depends on the initial energy density and therefore on the multiplicity reached in the collisions. The previous equations can also be written as

$$\frac{\epsilon_{Bj}}{\langle p_T\rangle^4} \equiv \frac{\sigma}{\langle p_T\rangle^3}. \tag{3.8}$$

Using the average transverse momentum distributions as a function of the multiplicity from ALICE and CMS, we get the energy density of Eq. (3.6). To investigate possible phase transition in the hadronic matter created in p+p, p+Pb, and Pb+Pb collisions, we use Eq. (3.8). As the first approximation, using the Color String Percolation Model, the $\langle p_{\mathrm{T}}\rangle$ is proportional to the initial temperature T [113]. This quantity has also been extracted from an analysis of the average transverse momentum, using a linear relationship, $\langle p_{\mathrm{T}}\rangle = a + bT$, between $\langle p_{\mathrm{T}}\rangle$ and T [114], where a and b are free fit parameters. It is worth mentioning that the relation between $\langle p_{\mathrm{T}}\rangle$ and T depends on the model used, and b is a function of the collision energy. However, as a first approach, we consider $\langle p_{\mathrm{T}}\rangle \sim T$, consequently the Eq. (3.8) as a function of $\langle p_{\mathrm{T}}\rangle$ provides results similar to those obtained from a plot of σ/T^3 as a function of T, analyzed using lattice QCD [101].

Figure 3.17 shows the plot of entropy scaled by $\langle p_{\mathrm{T}}\rangle^3$ ($\sigma \cdot S_T\tau/\langle p_{\mathrm{T}}\rangle^3$) as a function of $\langle p_{\mathrm{T}}\rangle$ computed using CMS data [56]. The distributions correspond to pions (Fig. 3.17a) and kaons (Fig. 3.17b) from CMS p+p collisions at 0.9, 2.76, 7.0 TeV [56]. The plot of the entropy instead of entropy density is to avoid the use of large uncertainty radii extracted from CMS, which precludes possible energy

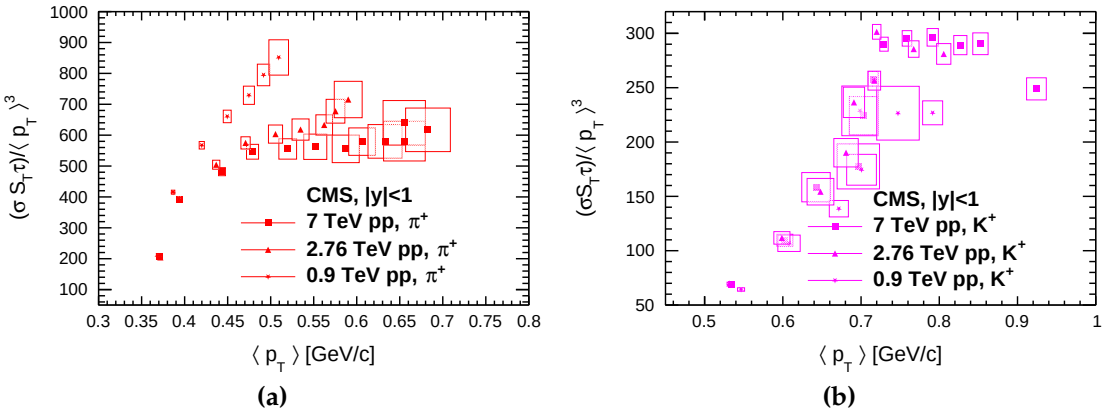

Figure 3.17.: Entropy density normalized to $\langle p_{\mathrm{T}} \rangle^3$ for pions (left) and kaons (right) from CMS p+p data [56] at different energies.

effects. This entropy has a rapid increase and seems to be saturated for pions and kaons produced in p+p at 7 TeV. Significant fluctuations in the behavior of entropy for the same species at different energies could be associated with the selection processes in the measurements by the CMS experiment. Figure 3.18a shows our results for entropy density as a function of $\langle p_{\mathrm{T}} \rangle$ for pions, kaons, protons, and Lambda's, computed with p+Pb ALICE data [111]. In all cases, the entropy rises to reach the values determined by the multiplicity as a function of $\langle p_{\mathrm{T}} \rangle$; we observe a faster growth for the lightest particles. When the entropy (entropy density multiplied by $S_T \tau$) is normalized to $\langle p_{\mathrm{T}} \rangle^3$ (Fig. 3.18b), however, all the cases can be fitted to a functional form Exp(A+B$\langle p_{\mathrm{T}} \rangle$) where A and B are shown in the Table 3.1. The distributions for Λ's and protons can also be fitted with a linear functional form, but the best fits are for exponential form.

Finally, the results for the entropy scaled to $\langle p_{\mathrm{T}} \rangle^3$ for all charged particles produced in ALICE p+p, p+Pb, and Pb+Pb colliding systems are shown in Fig. 3.19, together with predictions from the Monte Carlo event generators for the same systems and energies as the ALICE data. Fig. 3.19a shows the experimental data from p+p collisions, which are well described by EPOS, and PYTHIA predictions. It is interesting to note a kind of saturation for $\langle p_{\mathrm{T}} \rangle$ larger than 0.8 GeV/c.
Regarding p+Pb collisions, Fig. 3.19b shows that data and simulation have

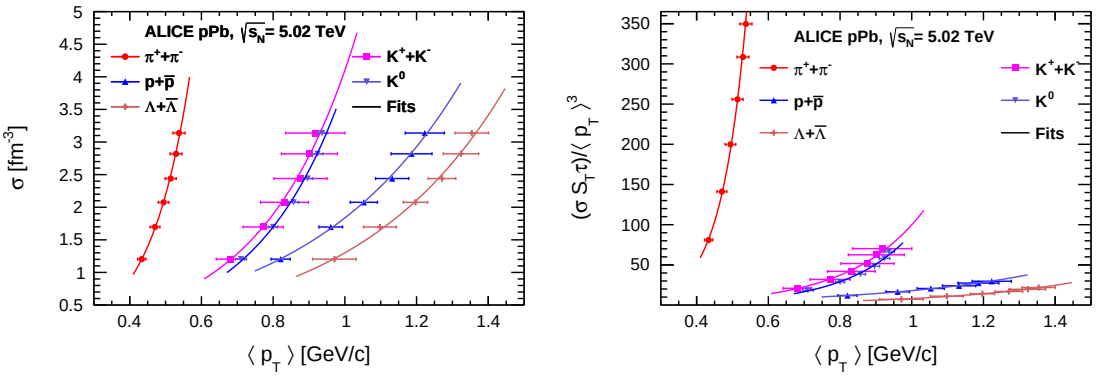

Figure 3.18.: Entropy density as a function of $\langle p_{\mathrm{T}} \rangle$ for identified particles (a). Entropy normalized to $\langle p_{\mathrm{T}} \rangle^3$ as a function of $\langle p_{\mathrm{T}} \rangle$, (b). Both cases, correspond to ALICE p+Pb data [111] at different energies.

Table 3.1.: Parameters of the fitted function: Exp (A +B $\langle p_{\mathrm{T}} \rangle$), in Fig. 3.18 (a) and 3.18 (b).

		$\pi^+ + \pi^-$	$K^+ + K^-$	$p^+ + \bar{p}$	K^0	$\Lambda + \bar{\Lambda}$
Fig. 9 (a)	A	-3.7114	-2.4520	-1.7269	-2.7737	-2.1473
	B [1/(GeV/c)]	8.9957	3.8628	2.3344	4.1288	2.4104
Fig. 9 (b)	A	-1.6948	-0.3344	0.6161	-1.0888	-0.6768
	B [1/(GeV/c)]	14.0796	4.9379	2.2758	5.5768	2.7725

the same trend: a rapid growth of the slope that appears around $\langle p_{\mathrm{T}} \rangle \approx 0.7$ GeV/c and $\langle p_{\mathrm{T}} \rangle \approx 0.75$ GeV/c for EPOS and PYTHIA respectively, while data are between both event generators. We emphasize that a well defined inflection point, around $\langle p_{\mathrm{T}} \rangle = 0.62$ GeV/c, is observed for EPOS when simulations cross the experimental data.

For Pb+Pb colliding system, shown in Fig. 3.19c, a sudden change in the entropy is observed in data and almost the same trend for PYTHIA is observed but shifted to higher $\langle p_{\mathrm{T}} \rangle$ values. The EPOS event generator produces a larger slope such that the distribution crosses the data and seems to bend backwards because the $\langle p_{\mathrm{T}} \rangle$ rises and then falls as the multiplicity increases, in

the pseudorapidity range of $|\eta| < 0.3$. This value was used to compare with the ALICE data. Fig. 3.19c, also shows the same distribution produced with EPOS in $|\eta| < 0.9$. We notice that it rises with a slope closer to that of data. The results observed from EPOS suggest that caution has to be taken to describe the most central pseudorapidity region, since this event generator does not describe data. Looking at the details of the sudden change in the entropy $\equiv \sigma S_{\mathrm{T}} \tau$ normalized to $\langle p_{\mathrm{T}} \rangle^3$ as a function of $\langle p_{\mathrm{T}} \rangle$ for the Pb+Pb ALICE data, we observe almost a linear growth for $\langle p_{\mathrm{T}} \rangle$ less than $\approx$ 0.61 GeV/c, while an exponential growth is observed for $\langle p_{\mathrm{T}} \rangle$ larger than 0.61 GeV/c. Assuming $\langle p_{\mathrm{T}} \rangle = 3T$ [115], the entropy normalized to temperature (S/T^3) has a linear behavior with respect to the temperature in the range from 0.172 to 0.203 GeV/c, and an exponential one for temperatures larger than 0.203 GeV/c.

Within our approaches we have obtained properties of the medium created in different colliding systems. More details can be computed; however, any conclusion from this analysis can only have a limited agreement with data and inspired QCD models due to the simplified model we used. Other properties will be reported elsewhere.

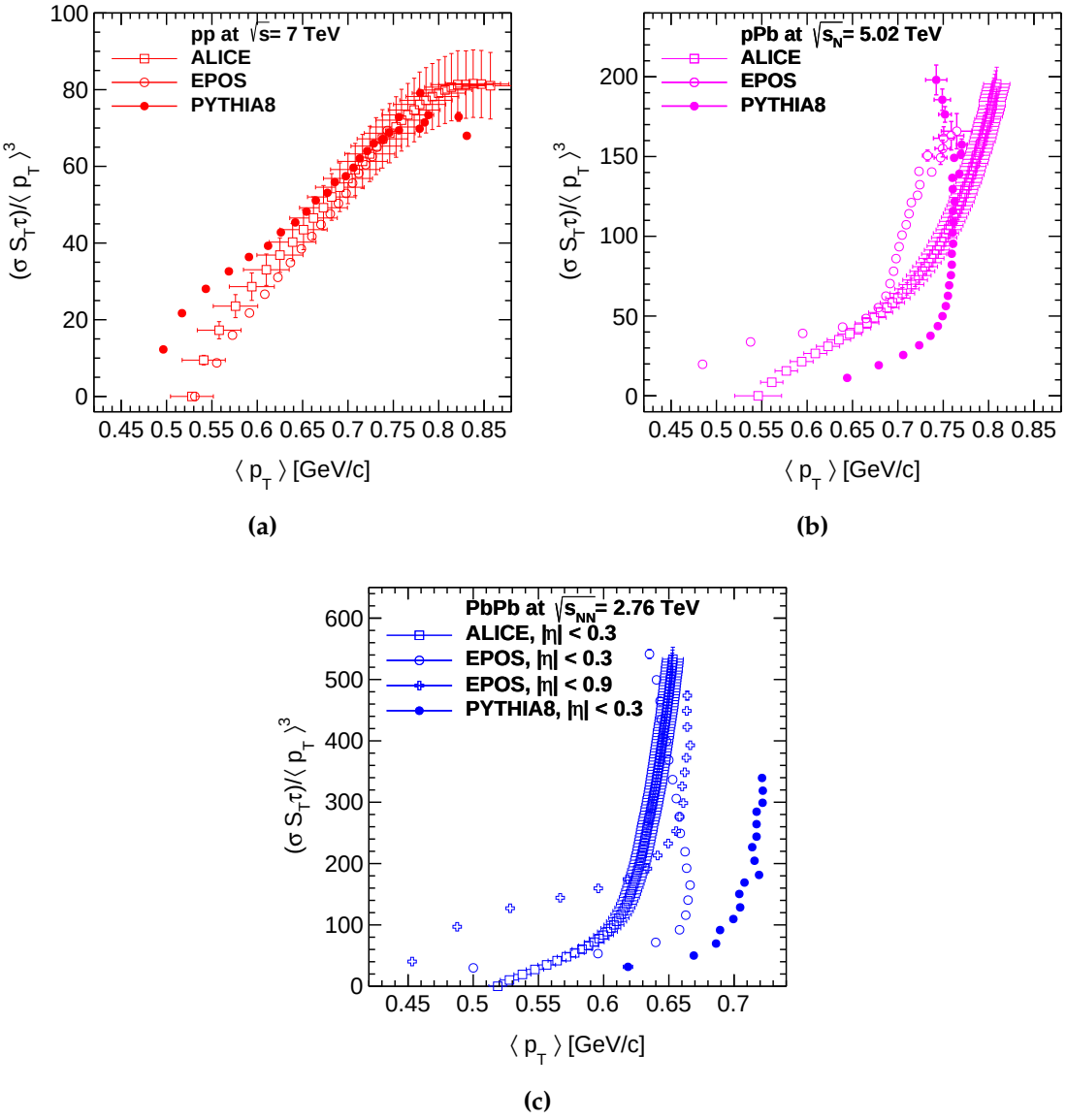

Figure 3.19.: Entropy density normalized to $\langle p_{\mathrm{T}} \rangle^3$ for ALICE p+p, p+Pb and Pb+Pb data [61] at different energies.

Chapter 4.

Discussion and conclusions

4.1. Discussion of results

This work address the experimental analysis of ALICE data to measure the transverse momentum yield of π^0 and η mesons through the Dalitz decay channel. This works reports also a phenomenological study, which is divided into the forward-backward multiplicity correlations, energy and entropy density results.

In the experimental part, preliminary results on the differential invariant yield as well as the differential invariant cross-section spectra for π^0 and η mesons in pp collisions at $\sqrt{s}$ = 5.02 TeV and $\sqrt{s}$ = 13 TeV is presented. The measurement of the π^0 and η mesons production has been carried out by detecting the final-state products of its Dalitz decay channel ($\pi^0 \to \gamma^*\gamma \to e^+e^-\gamma$) in the ALICE central barrel. The two primary electrons (coming from $\gamma^* \to e^+e^-$) were reconstructed using the TPC and ITS detectors, the identification was performed using the specific energy loss ($\mathrm{d}E/\mathrm{d}x$) in the TPC detector. On the other hand, photons (γ) were reconstructed using the Photon Conversion Method (PCM) which detects photons through their conversion products in the ALICE central barrel. The PCM requires the reconstruction of a secondary vertex, commonly known as V^0 particles which have a slight difference between the angle of the secondary and the primary vertex. The respective meson was obtained by computing the invariant mass distribution of the $\gamma^*\gamma$ pairs. The combinatorial background was

estimated using the mixed event technique which combines virtual photons with photons from different events. After background subtraction, the meson signal was fitted with a gaussian function convoluted with an exponential and a linear function. The exponential function was included to take into account the long bremsstrahlung tail at the left side of the meson signal peak. The linear function was included to subtract a possible residual background below the meson signal. The meson raw yields are accomplished by integrating the invariant mass fit for every range of transverse momentum, a variation on the integration windows is taken into account.
Using Monte Carlo simulation that implements PYTHIA passing through GEANT as particle generators, the raw meson yield was corrected by acceptance and efficiency. Moreover, the contamination from the 2γ decay in both cases was computed and subtracted from the raw yield. The systematic uncertainties were computed by varying each cut used in the virtual photon and in the photon reconstruction and in the respective meson signal extraction.

Regarding the phenomenological work, we compute the correlations of the charged hadron production in symmetric forward and backward pseudorapidity windows, in central and fragmentation pseudorapidity regions, using PYTHIA p+p event generator. The strength of this correlation, usually represented by b_{Corr}, has been studied taking into account different effects on the hadron production like weak decays, color reconnection, multiple parton interactions, collision energy and splitting the events into soft and hard QCD processes. Comparison with available data was also made, with the following results: The general trend is that the correlations observed at lower $\delta\eta$ values are diluted with respect to those observed for the maximal window ($\delta\eta$). Weak decays have an important role in central rapidity; they produce an enhancement around 40% on b_{Corr} for $\delta\eta = 0.2$ and approximately 5% for $\delta\eta = 0.9$. In the case of the fragmentation region, the behavior is similar but with higher b_{Corr}. In general, when the resonances are introduced, the b_{Corr} increases. This happens because the multiplicity increases, and is higher for central than forward pseudorapidity. However, it is important to point out that the differences between b_{Corr} for central and forward pseudorapidity region decrease as $\delta\eta$ increases. In fact,

analyzing the soft QCD processes one finds a scaling between long and short range correlations. Meanwhile for hard processes, a faster saturation of the b_{Corr} at central rapidity with respect to the fragmentation region is observed. Furthermore, color reconnection produces an almost constant reduction of the strength of the b_{Corr}; in the present work the maximum is around 14% for all $\delta\eta$ values. In a similar way, the collision energy produces an almost constant enhancement on b_{Corr}. The discrepancies could be attributed to a not linear relationship between the number of MPI and the multiplicity. The number of multiple parton interactions increases with the collision energy, as well as for more isotropic events where the multiplicity increases and consequently the b_{Corr} strength increases. However it saturates as the number of MPI does. Since the higher (lower) number of MPI can be associated with isotropic (jetty-like) events and the b_{Corr} is lower for jets than for isotropic events, this asseveration is attractive and may be used to investigate the number of MPI through the correlations on multiplicity in the underlying events from the experimental point of view. Finally, without trying to get a tune on the event generator, the simulation of p+p collisions at one energy and with an appropriate event selection on its number of MPI, it is possible to reproduce the experimental data at different energies, and consequently the predictions to other energies, taking care that these results are dependent on the MPI model.

For the phenomenological work related to energy and entropy density we study first the correlation between transverse momentum and multiplicity distributions for different colliding systems at energies of 0.01, 0.9, 2.76, 5.0, 7.0, and 13 TeV using two event generators: PYTHIA with/without CR; EPOS with/without fusion model as part of the hadronization. Then a data analysis is carried for the average transverse momentum versus multiplicity from ALICE and CMS experiments to extract thermodynamical properties of the system created in p+p, p+Pb, and Pb+Pb collisions at different collision energies. The results were compared with predictions from EPOS and PYTHIA event generators. Average multiplicity distributions increase with the collision energy and can be parameterized as $< N_{\mathrm{ch}} >= a + b \cdot p_{\mathrm{T}}^{c}$, where a, b, and c, are free parameters for each energy. A stronger dependence between $< N_{\mathrm{ch}} >$ and the collision

energy is observed at higher collision energies. The hadronization mechanism incorporated through CR in PYTHIA produces a more substantial reduction in multiplicity than the EPOS fusion model; this effect is more visible for transverse momentum larger than 0.5 GeV/c. On the other hand, the average transverse momentum as a function of the multiplicity, computed with PYTHIA, shows that a differential analysis in terms of impact-parameter is not enough to explain the data. The CR with different strengths is enough to explain the behavior of data at collision energies of 0.9, 2.76, and 7 TeV reported by the ALICE experiment. This has been tested for other energies finding good agreement. Nonetheless, in the case of the EPOS fusion model with a combination of impact-parameters, which is related to the hadronic matter model in the proton, it allows an excellent description of the data, although EPOS results without cut on impact-parameter are within experimental uncertainties.

We have shown that the average transverse momentum and Bjorken energy density as a function of multiplicity, normalized to the transverse interaction area, present a scaling law. The results were computed with ALICE data, PYTHIA, and EPOS event generators. For all cases, the $\langle p_{\mathrm{T}} \rangle$ scaling breaks in the lowest and highest multiplicity values, which can not be associated with flow effects, as other authors have suggested.

Regarding the thermodynamical properties obtained with an analysis of CMS and ALICE data: the results indicate an exponential growth of the energy and entropy normalized to $\langle p_{\mathrm{T}} \rangle^3$ as a function of the average transverse momentum for charged and identified particles measured in p+p, p+Pb, and Pb+Pb collisions at the available energies. This growth is faster for light particles with respect to heavy ones. Considering $\langle p_{\mathrm{T}} \rangle$ as a linear function of the initial temperature of the system created in the collisions, the conclusions obtained from $\epsilon_{Bj}/\langle p_{\mathrm{T}} \rangle^4$ are similar to those from ϵ_{Bj}/T^4, a quantity widely studied to look for a QCD phase transition. The same conclusion can be reached from σ/T^3. Analysis of experimental Pb+Pb data with $\langle p_{\mathrm{T}} \rangle = 3T$ produces an effective temperature range of 0.17-0.2 GeV/c, where the energy density normalized to T^4 has a linear behavior, and for effective temperatures larger than 0.2 GeV/c, it grows exponentially. Our results from EPOS and PYTHIA p+p collisions agree with ALICE p+p data and have the behavior obtained by lattice (2+1) flavor

QCD. They show a kind of saturation for $\langle p_{\mathrm{T}} \rangle$ larger than 0.8 GeV/c, which is not observed for either p+Pb and Pb+Pb ALICE data. The predictions from PYTHIA and EPOS show the data trend, but there is no complete agreement to ALICE data. Particularly, the $\langle p_{\mathrm{T}} \rangle$ in Pb+Pb from EPOS does not describe the data at the most central pseudorapidity and consequently produces two values of the entropy density for one $\langle p_{\mathrm{T}} \rangle$ value, which is not a physical result. Results for other thermodynamical variables require a more detailed analysis of the relation between $\langle p_{\mathrm{T}} \rangle$ and temperature and more precision on the radii measurements to look for a quantitative possible QCD phase transition. It is important to remember that, the results on the energy and entropy densities are calculated using simple models of Landau and Bjorken, respectively, based on hydrodynamical approaches. Consequently, our conclusions can thus be considered as qualitative results that could be improved using more realistic models in the calculations, hadronic matter in the proton, and models for the core created in p+p collisions.

4.2. Conclusion

We report the production for the Dalitz decay channel (π^0, $\eta \rightarrow \gamma^* \gamma \rightarrow e^+ + e^- + \gamma$) for the neutral meson π^0, η, as well as ratio π^0/η for $\sqrt{s} = 5.02$ TeV and $\sqrt{s} = 13$ TeV in the ranges of transverse momentum from 0.6 to 12 GeV/c for the first and from 0.4 to 12 GeV/c for the second time. There are previously reported measurement of same quantity as a function of multiplicity bins, observing slightly differences among the spectra. Meanwhile, the ratio of pions at $\sqrt{s} = 5.02$ TeV to those at $\sqrt{s} = 13$ TeV shows an increasing trend as a function of momentum. As a consistency check, the measured meson distributions were compared to measurements with independent methods made in ALICE: PCM, PHOS, EMCal, PCM-EMCal, and PCM-PHOS with their respective detector. The comparison with the different techniques shows excellent performance for low and intermediate range of transverse momentum distributions.

The Forward-Backward multiplicity correlation study was done considering the effects of colour reconnection and multiple parton interactions. The results agreed with ALICE data at the available energy, and was also made predictions for higher ones. Furthermore, we find a direct relationship between Forward-Backward multiplicity correlations and multiple parton interactions.

We analyze the average mean momentum in terms of the multiplicity, using different event generators, taking into account colour reconnection and hydrodynamics effects; without these effects, it is impossible to reproduce the data. Furthermore, with multiplicity and average transverse momentum distributions from Monte Carlo and real data we study the energy and entropy density in the Bjorken approach in p+p, p+Pb and Pb+Pb collisions. We find that for these variables a sudden rise in terms of mean transverse momentum for Monte Carlo and real data, resembling a possible phase transition as the case of lattice QCD results for the ϵ/T^4 as a function of the temperature; however, only the experimental data from p+p shows a kind of saturation.

Appendix A.

Monte Carlo Generator

This chapter is dedicated to qualitatively explaining the MonteCarlo generator's concepts. PYTHIA is the main generator used for analysis in high-energy physics for smaller systems. The hadronization mechanism and the hard and soft QCD process will be explained. Phenomenological effects such as the number of multiparton interactions (nMPI) and color reconnection are aborded in this section.

A.1. Modeling parameters of the hadroproduction

Hadronization processes are among the most widely studied topics. Despite these efforts, currently we only have effective theories to describe these phenomena. Different event generators have been developed to investigate hadronization processes in p+p, p+Pb, and ion-ion collision systems. Each event generator approaches hadron production mechanisms in a different manner but most of them are based on string fragmentation models at high energies. Some general aspects are briefly described in the following lines: PYTHIA hadronization processes include the CR mechanisms providing an alternative final interaction mechanism, modifying some kinematical variables of the hadron-hadron collisions and lepton collisions. These final state interactions allow a better description of the transverse momentum measured by the ALICE experiment. Color Reconnection

is based on the production of hadrons through the interaction probability between partons of low and high p_T. These interacting partons can come from the beam or from the remnant of the beam. They can be quantified by the probability distribution of reconnecting partons, $P_{rec}(p_T)$, defined as:

$$P_{rec}(p_T) = \frac{(R_{rec}\ p_{T0})^2}{(R_{rec}\ p_{T0})^2 + p_T^2}, \tag{A.1}$$

where the range of CR, $0 \leq R_{rec} \leq 10$, is a phenomenological parameter and p_{T0} is an energy dependent parameter used to damp the low p_T divergence of the $2 \rightarrow 2$ QCD cross section. Equation (A.1) used for the description of the color flow, is based on the Multiple Parton Interaction model. However, there are other newer approaches [116], or even older ones such as those developed to describe W bosons in $e^- + e^-$ processes [117]. Each model contains additional parameters to turn on/off the color CR.
Hadron-hadron collisions consider a spherically symmetric matter distribution of the hadrons, $\rho(\mathbf{x})d^3x = \rho(r)d^3x$. In collision processes, the overlap of the colliding hadrons is a function of the impact-parameter (b) and is given by

$$O(b) \propto \int\int d^3x dt \rho(x,y,z)\rho(x,y,z-\sqrt{b^2-t^2}), \tag{A.2}$$

where different ρ distributions have been studied previously [118]. Taking a simple Gaussian for this ρ, the convolution becomes trivial, but it does not give a good enough description of the data. A better choice of this matter distribution is a double Gaussian function given by:

$$\rho(r) = (1-\beta)\frac{1}{r_1^3}\exp(\frac{r^2}{r_1^3}) + \beta\frac{1}{r_2^3}\exp(-\frac{r^2}{r_2^3}), \tag{A.3}$$

this equation corresponds to a distribution with a small core region of radius r_2 and containing a fraction (β) of the total hadronic matter, embedded in a larger hadron of radius r_1. Two free parameters β and r_2/r_1 are sufficient to give the

necessary flexibility.
This way of modeling the overlap matter distribution allows the study of hadron-hadron collisions as a function of impact-parameter as for heavy-ion collisions. Thus kinematical variables like $\langle p_{\mathrm{T}} \rangle$ in hadron production can also be studied in terms of the impact-parameter [118].

EPOS simulates interactions among ions as binary interactions, each represented by a parton ladder; this ladder considers a longitudinal color field, conveniently treated as a relativistic string. The string decays via the production of quark anti-quark pairs creating string fragments usually identified with hadrons [119].
Our EPOS p+p simulation at the energy of $\sqrt{(s)} = 10$ GeV used the version 1.99, and for larger than 10 GeV, EPOS-LHC was used. From now on, these choices are referred to as EPOS. Both versions include a simplified treatment of final state interaction but do not include full hydro as is already possible in most recent EPOS 3 not released version.
EPOS − LHC is a minimum bias hadronic generator used for heavy-ion collisions and cosmic ray air shower development. However, the goal of this generator is to describe soft particle production ($p_{\mathrm{T}} < \sim 5$ GeV$/c$) for any system and energy in great detail. Moreover, high-density effects leading to collective behavior in heavy-ion collisions are taken into account [120] by the fusion model, which means that there is the probability to form a core and a corona, even in proton-proton collisions. The model considers the hadronization part of the secondary particles, and the flow intensity includes different radial flow types that depend only on the total mass of the high density core produced by the overlap of the string segments due to multiple parton interactions in proton-proton or multiple nucleon interactions. The model also includes different radial flow types in the core created in a small volume due to multiple scattering between partons in a single pair of nucleons, which is the case of p+p collisions.

A.2. Event generator: PYTHIA

The Monte Carlo methods are computational algorithms that rely on repeated random sampling to obtain numerical results. In high energy physics, this is beneficial because it lets us think that every random sample tested in a model can result from the collision of two hadrons. After all, with Heisenberg's Uncertainty principle, we are only capable to know the probability, meaning that Monte Carlo methods are just the perfect tool for particle physics.

The event generator used for this work is PTYHIA [121] [122]; it is one of the best references and can reproduce and predict experimental results. PYTHIA contains multiple physics theories and models tuned with experimental data. The primary process contains hard and soft QCD processes, supersymmetry models (SUSY), leptoquark production, and more.

PYTHIA generator has implemented diverse parameters, which can be fitted in terms of the type of physics you are scrutinizing, is not the same work with jet and underlying events. The parameters emerge for the necessity of understanding the physics, specifically the hadronization part and multiple parton interactions, which are involved with no-perturbative QCD. An example of this parameter is the color reconnection, fitted in experimental data.

The generator works in the following form, suppose we have a function $f(x)$ that is not negative in an interval $x_{min} \leq x \leq x_{max}$. Then, if we need to select a random variable x to obtain the probability in an interval dx, this must be proportional to the function $f(x)dx$. In Monte Carlo, the function $f(x)$ can be the fragmentation function or the differential cross-section of one QCD process $ij \to k$,

$$\sigma_{ij\to k} = \int dx_1 \int dx_2 f_i^1(x_1) f_j^2(x_1) \hat{\sigma}_{ij\to k}, \tag{A.4}$$

The process is codified in a matrix form where $\hat{\sigma}$ is the cross-section at the partonic level. The term $f_i^a(x)$ is the partonic distribution function, which describes the probability of finding a parton i inside a particle a; this parton i will carry a fraction of the moment x of the particle a. For the hard process, the distribution function of partons depends on the scale and momentum transfer in the collision.

PYTHIA starts selecting the kind of class of particle involved in the beams, and the collision energy subsequently starts the sampling. In the second place, the selection of random hadrons starts the collision; for everyone, it generates a parton sequence. The first collision will be a hard process where the resonances are produced. After that, the partons decay, and the decay sequence starts again until the final state hadron is produced.

In the decay process, the fragmentation functions, the cross-sections of each process, and the particle distribution function are employed. Other factors that are taken into account are the remanents of the beam particles. These residual particles are not considered as initial particles but directly affect the multiplicity and moment of the events; one way around is color reconnection.

A.2.1. Process in PYTHIA

Distinguishing between hard and soft QCD processes can be made by measuring the particle with the higher transverse moment in the event (Leading particle) generated. If the particle's momentum is lower than two (2 GeV/c), the event is classified as soft, and meanwhile, if the momentum is higher than two (2 GeV/c), it is a hard process.

Hard process

Hard processes focus on $2 \rightarrow 1$ and $2 \rightarrow 2$ processes with some $2 \rightarrow 3$ available. However, it may be possible to generate processes with higher final-state multiplicity if the particles arise from decays of resonances.

Hard QCD processes implemented in PYTHIA are divided into light quarks and gluons: $gg \to gg$, $qg \to qg$, etc. Heavy flavors $gg \to c\bar{c}$, $gg \to b\bar{b}$, and others. Finally, Three-parton processes such as $gg \to ggg$, $q\bar{q} \to ggg$, etc. More processes are implemented, including Electroweak (EW) processes prompt photon production. Onia include the production of any ${}^3S_1$, ${}^3P_J$, and ${}^3D_J$ states of charmonium or bottomonium via color-singlet and color-octet mechanisms. Top production, singly or in pairs, fermion production via strong or EW interactions, Higgs and SUSY process between others.

Soft process

Theoretically the soft process attempt to describe all the components of the total cross section in the hadronic collisons in terms of the elastic, diffractive and no-difractive process.

In recent years, the diffraction modeling has improved to a comparable level, even if tuning of the related free parameters lags. The total, elastic, and inelastic cross sections are obtained from Regge fits data. At the time of writing, the default for pp collisions is the 1992 Donnachie-Landshoff parametrization [26], with one Pomeron and one Reggeon term,

$$\sigma_{TOT}^{pp}(s) = (21.70 s^{0.0808} + 56.08 s^{0.4525}) mb, \tag{A.5}$$

with the pp CM energy squared, s, in units of GeV^{-2}. For pp collisions, the coefficient of the second (Reggeon) term changes to 98.39; A simple exponential falloff approximates the elastic cross-section with momentum transfer, valid at small Mandelstam t, connected to the total cross-section through the optical theorem,

$$\frac{d\sigma_{EL}^{pp}}{dt} = \frac{(\sigma_{TOT}^{pp})^2}{16\pi^2} exp(B_{EL}^{pp}(s)t) \qquad \rightarrow \qquad \sigma_{EL}^{pp}(s) = \frac{(\sigma_{TOT}^{pp})^3}{16\pi(B_{EL}^{pp}(s))}, \tag{A.6}$$

using $1mb = 1/(0.3894GeV^{-2}$ to convert between mb and GeV units, and $B_{EL}^{pp} = 5 + 4s0.0808$ the pp elastic slope in GeV^{-2}, defined using the same power of s as the Pomeron term in σ_{TOT}, To maintain sensible asymptotic behavior at high energies. We emphasize that the electromagnetic Coulomb term, with interference, can optionally be switched on for elastic scattering, a feature unique to Pythia among influential generators. The inelastic cross-section is a derived quantity:

$$\sigma_{INEL}(s) = \sigma_{TOT}(s) - \sigma_{EL}(s). \tag{A.7}$$

The elastic process is a dispersion of type $AB \rightarrow AB$; the diffractive can be separated in single $AB \rightarrow XB, \quad AB \rightarrow AX$, double $AB \rightarrow X_1X_2$, and central $AB \rightarrow AXB$. The inelastic non-diffractive part of the total cross-section is called the "minimum-bias component", the formalism is based on an eikonalized description of all the hard QCD processes, which includes them in combination with low transverse momentum events. In Pythia, to change between the process is through the components given by choice between five different parametrizations [28, 29]. The current default is the Schuler-Sjostrand one [27, 30]

The primary process used is soft, which contains the hard ones, which the particles can acquire a high and low transverse momentum. The theoretical method to distinguish is according to the massive QCD parameters, which ones have additional corrections in the mass in terms of power $\approx m/E$, with E the scale energy [123], all this in partonic level, in other words, process like $gg, qg, qq, q\overline{q} \rightarrow gg, qg, qq, gg$. In shorter terms, the hard process must be more inclusive if the energy is more significant than its mass; therefore, the most extensive energy comes from the momentum.

A.3. Hadron production

Perturbative QCD theory, described in quarks and gluons, is validated at short distances (smaller than Armstrongs). Then, QCD becomes a theory with " strong " interactions at a higher distance. In this confinement regimen, the parton colors are transformed into hadrons without color; this process is called hadronization. Everything did not disperse at a hadron level, thanks to the strong forces.

Meanwhile, non-perturbative QCD remains without an exact solution; the hadronization process is not totally understood at first principle. The study in spectroscopy of hadrons and lattice QCD supports the idea of lineal confinement in the absence of quarks dynamics. In other words, the energy deposited in the color dipole field between charge and anticharge keeps growing linearly with the separation between them; this is the dipole model, assuming that we ignore the Coulomb term. The supposition of the lineal confinement provides the point of beginning for the "String model," illustrated in the production of particles in jets back-to-back.

A.3.1. Lund string fragmentation

All existing models are of a probabilistic and iterative nature. This implies that the fragmentation process as a whole is represented in terms of one or a few simple underlying branchings of the type, for example, jet $\rightarrow$ hadron $+$ remainder-jet, string $\rightarrow$ hadron $+$ remainder-string, and so onwards. At each branching, probabilistic rules are given for the production of new flavors and the sharing of energy and momentum between the products.

It is necessary to work with the annihilation on electron-positron pairs producing quarks-antiquarks ($e^+e^- \rightarrow q\bar{q}$) to understand the hadron fragmentation in quarks.

$$\sigma(e^+e^- \to hadrons) = \sum_q \sigma(e^+e^- \to q\overline{q}), \tag{A.8}$$

As the q and $\overline{q}$ drive apart, the potential energy stored in the string grows, and the string may break by the production of a new $q'\overline{q}'$ pair, so that the system splits into two color-singlet systems $q'\overline{q}$ and $q\overline{q}'$. If the invariant mass of either of these string pieces is large enough, additional breaks may occur. In the Lund string model, the string break-up process is assumed to proceed until only on-mass-shell hadrons remain, each hadron corresponding to a miniature piece of string with a quark in one end and an antiquark in the other.

The Lund model invokes the idea of quantum mechanical tunneling in order to cause the quark-antiquark string break-up. The different string breaks are causally disconnected, so it is possible to describe the breaks in any convenient order.

However, the choice of starting the fragmentation from the quark end is arbitrary. Therefore, a fragmentation process described in terms of starting at the $\overline{q}$ end of the system and fragmenting towards the q end should be equivalent. This "left–right" symmetry constrains the allowed shape of the fragmentation function $f(z)$, where z is the fraction of the remaining light-cone momentum $E \pm p_z$ ($+$ for the q jet, $-$ for the $\overline{q}$ one) taken by each new particle. The resulting "Lund symmetric fragmentation function" has two free parameters determined from data.

$$f(z) \propto \frac{1}{z} z^{a_\alpha} \left(\frac{1-z}{z}\right)^{a_\beta} exp\left(-\frac{bm_\perp^2}{z}\right), \tag{A.9}$$

where $f(z)$ is the fragmentation function, which represents the probability that a given z is selected, could in principle, be random. There is one distinct parameter a for each flavour, with the index α corresponding to the "old" flavour in the

iteration process and β to the "new" flavour. It is typical to put all parameters the same, arriving at the simplified expression:

$$f(z) \propto z^{-1}(1-z)^{a} exp(-bm_{\perp}^{2}/z). \tag{A.10}$$

In the PYTHIA, only two separate alpha values can be given: for quark pair and diquark production. In addition, there is the b parameter, which is universal. The explicit mass dependence in f (z) indicates a harder fragmentation function for heavier hadrons. The asymptotic behavior of the mean z value for heavy hadrons is:

$$\langle z \rangle \approx 1 - \frac{1+a}{-bm_{\perp}^{2}}. \tag{A.11}$$

This result leads to a harder spectrum for B Mesons, which is not observed in experimental data. A solution is implemented by Bowler [124] has shown, using the ArtruMennessier model [125]. Therefore, in PYTHIA, an approximation for the alpha term has been used [126] because the ArtruMennessier model only applies in a continuous mass spectrum for clusters. the approximation used in PYTHIA is the following:

$$f(z) \propto \frac{1}{z^{1+r_{Q}bm_{Q}^{2}}} z^{a_{\alpha}} \left(\frac{1-z}{z}\right)^{a_{\beta}} exp\left(-\frac{bm_{\perp}^{2}}{z}\right). \tag{A.12}$$

Different fragmentation function are implemented in PYTHIA, one of the is The Field–Feynman parameterization [127],

$$f(z) = 1 - a + 3a(1-z)^{2}, \tag{A.13}$$

this it is only available for the light quarks. For heavier flavors Peterson/SLAC formula it is used in PYTHIA [128],

$$f(z) \propto \frac{1}{z\left(1-\frac{1}{z}-\frac{\epsilon_Q}{1-z}\right)^2}, \tag{A.14}$$

where ϵ_Q is a free parameter, expected to scale between flavours like $\epsilon_Q = 1/m_Q^2$ The cross-section of production of the hadrons is obtained through the sum over all the color quark: $q = u, d, s, ..., h$ represents the hadron, E_h the energy measure, and his corresponding cross-section is:

$$\frac{d\sigma}{dz} = (e^+e^- \to hx) = \sum_q \sigma(e^+e^- \to q\overline{q})[D_q^h(z) + D_{\overline{q}}^h(z)], \tag{A.15}$$

the secuencial sum of two events la suma secuencial de dos eventos, la producción de un par $q\overline{q}$, seguida por la fragmentación de un q o un $\overline{q}$. La función $D(z)$ representa la probabilidad de que el quark q y $\overline{q}$ forme el hadrón h, llevando una fracción de energía z de los quarks, es decir,

The sequential sum of two events, the production of a pair $q\overline{q}$, followed by the fragmentation of q or $\overline{q}$, where function $G(x)$ represents the probability of the quark q and $q\overline{q}$ create and hadron, containing a fraction of the energy Z of both quarks. Then the fragmentation function $D(z)$ describes the transition, and $D(z)$ follows the rule of normalization and conservation of momentum. Where z is the limit of the energy to produce a hadron of mass m, and n is the mean multiplicity of the hadrons

$$z = \frac{E_h}{E_q} = \frac{E_h}{E_{\overline{q}}} = \frac{2E_h}{Q}, \tag{A.16}$$

the fragmentation function $D(z)$, describe the transition of *parton→hadron*. As a probability $D(z)$ obey the rule of normalization and energy conservation:

$$\sum_h \int_0^1 z D_q^h(z) dz = 1, \tag{A.17}$$

$$\sum_q \int_{z_{min}}^1 [D_{\bar{q}}^h(z) + D_q^h(z)] dz = n_h, \tag{A.18}$$

where z_{min} is the energy limit $2m_h/Q$ required to produce an hadron of mass m_h, and n_h is the mean multiplicity of hadrons of type h.

A.4. Multiple Parton Interaction

In PYTHIA, in order to estimate the number of multiple parton interactions, they need to know the perturbative QCD jet cross section for parton parton interaction [85]:

$$\frac{d\sigma}{dp_{\mathrm{T}}^2} = \sum_{i,j,k} \int\int\int f_i^a(x_1, Q^2) f_j^b(x_2, Q^2) \frac{\hat{\sigma}_{i,j}^k}{d\hat{t}} \delta(p_{\mathrm{T}}^2 - \frac{\hat{t}\hat{u}}{\hat{s}}) dx_1 dx_2 d\hat{t} \tag{A.19}$$

where $f_{i(j)}^{a(b)}(x, Q^2)$ are the parton distribution functions of the incoming partons $i(j)$, carrying a fraction x of the energy and longitudinal momentum of the incoming hadron $a(b)$, for a given factorization and renormalization scale $Q^2 = p_{\mathrm{T}}^2 = \hat{t}\hat{u}/\hat{s}$, with the hard scattering cross section ($\hat{\sigma}_{i,j}^k$) for k-th sub-process between incoming partons i and j, and a fragmentation function (δ). The Mandelstam variables are related for massless partons by $\hat{s} + \hat{t} + \hat{u} = 0$. The hardness of the parton-parton interaction is provided by the corresponding integrated cross section which depends on the $p_{\mathrm{T,min}}$ scale:

$$\sigma_{int}(p_{\mathrm{T,min}}) = \int_{p_{\mathrm{T,min}}^2}^{s/4} \frac{d\sigma}{dp_{\mathrm{T}}^2} dp_{\mathrm{T}}^2. \tag{A.20}$$

Diffractive events contribute with a small fraction of the perturbative jet activity, however, these events do not contribute to elastic processes. Therefore, the simplest model sets out to describe only inelastic non-diffractive events, with an approximately known cross section. It is thus concluded that the average of such events should contain hard interactions. An average above unit corresponds to more than one sub-collision per event, which is allowed by the multiple structure of the incoming hadrons, described by the following expression [86]:

$$\langle n_{MPI}(p_{T,min})\rangle = \frac{\sigma_{int}(p_{T_{min}})}{\sigma_{nd}} \tag{A.21}$$

where σ_{nd} and $\sigma_{int}(p_{T_{min}})$ correspond to the cross section for non diffractive events and to the integrated one, respectively.

Of course $\langle n_{MPI}\rangle$ is multiplicity-dependent and seems to saturate according to the previous calculation [129], increasing for forward compared to central pseudorapidities.
It becomes important to explore the average number of MPI and its relationship with F − B multiplicity correlations since these encode essential information on the borderline between perturbative and non-perturbative physics, as has been discussed [86].

A.5. Colour Reconnection

Color reconnection (CR) could be connected to the number of MPI, though this represents an independent research avenue [130]. Starting from the lowest p_T interaction in a set of multiple parton interactions, a reconnection probability for an interaction with hardness scale p_T is given by $P_{rec}(p_T)$

$$P_{rec}(p_T) = \frac{(R_{rec}\ p_{T_0})^2}{(R_{rec}\ p_{T_0})^2 + p_T^2} \tag{A.22}$$

where the range of CR, $0 \leq R_{rec} \leq 10$, is a phenomenological parameter and p_{T_0} is an energy dependent parameter used to damp the low p_T divergence of the $2 \rightarrow 2$ QCD cross section. CR was essential to describe successfully the average transverse momentum of charged hadrons at LHC energies [87]. Specific applications of CR include top quark, Z^0 and $W^{\pm}$ decays, since they happen after previous hard perturbative activity like initial and final state radiation, as well as multiple parton interactions, but still inside the hadronizing color fields, thereby allowing CR with the rest of the event. For LHC studies, several new CR models were implemented in PYTHIA 8 [131]. Other studies on CR have been proposed as an alternative mechanism to produce flow like effects in proton-proton collisions [132] where the direct variable that changes with the CR is the multiplicity distribution, that decreases when CR increases and, consequently, it should produce an effect on the F − B multiplicity correlations multiplicity.

Appendix B.

Experimental parameters

This appendix is dedicate to the different parameters we select in the experimental study of Dalitz for the ALICE experiment.

B.1. Dalitz: Physics parameter

Physics selection are the cuts used for almost all the analysis, are the standard one to get proper particles candidates in the analysis.

	TPC	ITS
Cluster	$< 20GeV = f(p_T)(ncls)$ $> 20GeV = 100$	
Accept Kinks	No	
SA	Yes	
Shared	Yes	
$\|\eta\|$	0.9	
p_T	> 0.15 GeV/c	
Refit	Yes	Yes
$\chi^2/Cluster$	4	36
SPD		Any

	Vertex
DCAz	3.2 cm (Accept secondaries)
DCAxy	2.4 cm (Accept secondaries)
χ^2 TPC	36
Constrain Global	(Accept secondaries)
σ	Yes (Accept secondaries)
2D	No

Table B.1.: The filter used on the ESD data to generate the AOD sample, showing the cut aplied to the variables.

B.2. Dalitz: positron-electron selection

Electron positron selection is based in the cuts used in TPC and ITS for the electron positron pair used for the Dalitz decay.

ID	*Parameter*	*Nominal*
2	Max χ^2 TPC Constrained Global	36
0	e dE/dx σ ITS Cut	No
4	e dE/dx σ TPC Cut	[-4,5] σ
c	π dE/dx σ TPC Cut	$> 2\sigma$, 0.5 p_{T}
6	π Min Momentum dE/dx σ TPC Cut	0.4 GeV/c
4	π Max Momentum dE/dx σ TPC Cut	3.5 GeV/c
0	Low Rejection σ Cut	No
0	kTOF electron PID	No
2	cluster ITS Cut	One hit in any layer of SPD
6	cluster TPC Cut	70, TPCToF=0.6
3	η Cut	0.9
2	Ψ_{Pair} $(\Delta\Phi)$	0.6 (Section 2.1.2)
0	Reject Shared Electron Gamma	No
2	Max χ^2 Per Cluster TPC	4
2	Max χ^2 Per Cluster ITS	36
2	p_{T} Cut	0.125 GeV/c
3	DCA Cut	Standard 2011
7	Mass Cut	if p_{T} <1.0 GeV $\rightarrow <$ 0.015GeV
		or p_{T} >1.0 GeV $\rightarrow <$ 0.035GeV
1	Weights	Yes
0	VPhoton MCP Smearing	No

Table B.2.: Primary electron (positron) and $\gamma*$ selection cut code description with the specific cut values used in this analysis.

B.3. Dalitz: photon selection

ID	*Parameter*	*Nominal*
0	V0 Finder Type	Only V0 finder
d	η Cut	0.8
m	Min R Cut	5 to 180 cm, exclusion of 55-72 cm
0	η For ϕ Cut	-0.9 to 0.9
0	Min ϕ Cut	0, No shrink TPC Acceptance
0	Max ϕ Cut	2π,No shrink TPC Acceptance
0	Single p_T Cut	0.05 GeV/c
9	Cluster TPC Cut	0, no info
f	e dE/dx σ Cut	$[-3, 4]$ σ
9	π dE/dx σ Cut	> 1 σ, with $p_T > 0.5 GeV/c^2$
7	π Min Momentum dE/dx σ Cut	0.4 GeV/c
3	π Max Momentum dE/dx σ Cut	3.5 GeV/c
0	Low P Rejection σ Cut	No
0	TOF electron PID	No
0	ITS electron PID	No
0	TRD electron PID	No
d	q_T Max Cut	$q_T < 0.5$, p_T dependence, 2D cut
g	χ^2 Gamma Cut	50, Exp factor = -0.055
e	Ψ_{Pair}	0.18 and Exp factor = -0.055 (χ^2)
0	Do Photon Asymmetry Cut	No
4	Cosine Pointing Angle	Cos(Open Angle) > 0.85
0	Shared Electron Cuts	No
4	Reject To Close V0s	Yes
0	DCA Radius (plane xy) Primary Vertex	1000
0	DCA Z Primary Vertex	1000
0	Event Plane	No Event plane

Table B.3.: Photon selection cut code description an avaible in the code with the cut values used in this analysis.

B.4. Dalitz: meson selection

ID	*Parameter*	*Nominal*
0	Meson kind	No info
1	Background Scheme	Mixed event, V^0 multiplicity
5	Number of BackGround Events	50 limit
2	Degrees for Rotation Method	15 free parameters
1	Rapidity Meson Cut	0.8
0	Min p_T Cut	No cut
3	α Meson Cut	
	Min cut	0.0
	Max cut	0.1
5	Selection Window	
	Low	0.1
	High	0.15
	Accepted meson mass	kTRUE
0	Shared Electron Cuts	No
0	Reject to Close V0s	No, min 250 V0
0	Use MCP Smearing	0,1,0,0
0	Distance Closes Aproche (DCA) $\gamma\gamma$	No, 1000
0	DCA Radius (plane xy) Primary Vertex	No, 1000
0	DCA Z Primary Vertex	No, 1000
0	Min Opening angle Meson Cut	0 and not p_T dep
0	Max Opening angle Meson Cut	π and not p_T dep

Table B.4.: Meson selection cut code description with the specific cut values used in the analysis.

B.5. Dalitz: systematic variation

Quantities	*Standard*	*Variations*
Electron PID		
dE/dx e-line γ		
σ dE/dx, $e^{\pm}$	-3 $<\sigma<$5	-4$<\sigma<$5, -2.5$<\sigma<$4
dE/dx π^0 rejection-line γ		
above σ	$>$ 1,-10 p_{T}	$>$ 0,-10 p_{T}, $>$ 2,-10 p_{T}
dE/dx e-line $\gamma*$		
σ dE/dx, $e^{\pm}$	-3 $<\sigma<$5	-3$<\sigma<$5, -4$<\sigma<$4
dE/dx π^0 rejection-line $\gamma*$		
above σ	$>$ 2, 0.5 p_{T}	$>$ 2.5, -10 p_{T}, $>$ 2, 2.0 p_{T}
$p_{min,max}$ for π^0 rejection γ	0.4, 3.5 GeV/c	
$p_{min,max}$ for π^0 rejection $\gamma*$	0.4, 3.5 GeV/c	
Track reconstruction		
Single p_T $\gamma*$	$>$ 0.125 GeV/c	$>$0.15, $>$0.1 GeV/c
Single p_T γ	$>$0.050 GeV/c	$>$0.075, $>$0.1,$>$0.0 GeV/c
$N_{TPCcls}^{found}/N_{TPCcls}^{findable}$ $\gamma*$	$>$0.6	$>$0.35, $>$0.7
DCA primary	$z < 2$ cm $xy(p_T)$	$z < 2$ cm, $xy < 1$ cm
TPC Cluster $\gamma*$	< 70	$< 80, 60$

Table B.5.: Compilation of the variation used on this analysis for the π^0 and η meson, for the category of Electron PID and Track reconstruction.

Quantities	*Standard*	*Variations*
Photon selection		
cos(Point Angle) γ	> 0.85	$> -1, > 0.9$
χ^2 $2D$ Max γ	< 30	$< 20, < 50$
q_T $2D$ Max γ	< 0.05	$< 0.06, < 0.03$
$M_{e^+e^-}$	if $p_{\mathrm{T}} < 1.0\,\mathrm{GeV}/c$, $< 0.015\,\mathrm{GeV}/c^2$	if $p_{\mathrm{T}} < 1.0\,\mathrm{GeV}/c$, $< 0.02\,\mathrm{GeV}/c^2$
	or $p_{\mathrm{T}} > 1.0\,\mathrm{GeV}/c < 0.035\,\mathrm{GeV}/c^2$	or $p_{\mathrm{T}} > 1.0\,\mathrm{GeV}/c < 0.03\,\mathrm{GeV}/c^2$,
		if $p_{\mathrm{T}} < 1.0\,\mathrm{GeV}/c$, $< 0.027\,\mathrm{GeV}/c^2$
		or $p_{\mathrm{T}} > 1.0\,\mathrm{GeV}/c < 0.054\,\mathrm{GeV}/c^2$,
		$< 0.02\,\mathrm{GeV}/c^2$
Ψ_{Pair} for γ	< 0.05	$< 0.06, < 0.03$
Reconstruction efficiency		
α meson	$[0.0, 0.1]$	$[p_T]$dependence, $[0.0, 0.85]$
η γ	< 0.8	$< 0.85, < 0.9$
$\pi^0 \to \gamma\gamma$ **Rejection**		
Ψ_{Pair} for $\gamma*$	< 0.6	$< 0.65, < 0.45$

Table B.6.: Compilation of the variation used on this analysis for the π^0 and η meson, for the category of Photon selection, Reconstruction efficiency and $\pi^0 \to \gamma\gamma$ rejection.

Bibliography

[1] A. Andronic, P. Braun-Munzinger, K. Redlich, and J. Stachel, (2017), 1710.09425.

[2] J. E. Bernhard, J. S. Moreland, S. A. Bass, J. Liu, and U. Heinz, Phys. Rev. **C**94, 024907 (2016), 1605.03954.

[3] D. Boyanovsky, H. J. de Vega, and D. J. Schwarz, Ann. Rev. Nucl. Part. Sci. **5**6, 441 (2006), hep-ph/0602002.

[4] L. Evans and P. Bryant, JINST **3**, S08001 (2008).

[5] ALICE, J. Adam *et al.*, Phys. Lett. **B**754, 235 (2016), 1509.07324.

[6] ALICE, B. B. Abelev *et al.*, Phys. Rev. **D**91, 012001 (2015), 1405.4117.

[7] ALICE, B. Abelev *et al.*, Phys. Lett. **B**717, 162 (2012), 1205.5724.

[8] ALICE, B. Abelev *et al.*, Eur. Phys. J. **C74**, 3108 (2014), 1405.3794.

[9] ALICE, S. Acharya *et al.*, Eur. Phys. J. **C**77, 339 (2017), 1702.00917.

[10] ALICE, S. Acharya *et al.*, (2017), 1708.08745.

[11] D. d'Enterria, K. J. Eskola, I. Helenius, and H. Paukkunen, Nucl. Phys. **B**883, 615 (2014), 1311.1415.

[12] D. de Florian, R. Sassot, M. Epele, R. J. Hernández-Pinto, and M. Stratmann, Phys. Rev. **D**91, 014035 (2015), 1410.6027.

[13] M. Bourquin and J. M. Gaillard, Nucl. Phys. **B**114, 334 (1976).

[14] PHENIX, S. S. Adler *et al.*, Phys. Rev. C **7**5, 024909 (2007).

[15] P. K. Khandai, P. Shukla, and V. Singh, Phys. Rev. **C**84, 054904 (2011), 1110.3929.

[16] PHENIX, A. Adare *et al.*, Phys. Rev. **D**83, 052004 (2011), 1005.3674.

[17] ALICE, S. Acharya *et al.*, Eur. Phys. J. **C**78, 624 (2018), 1801.07051.

[18] K. Jiang *et al.*, Phys. Rev. **C**91, 024910 (2015), 1312.4230.

[19] G. Agakishiev *et al.*, Eur. Phys. J. **C**4, 249 (1998).

[20] R. H. Dalitz, Proceedings of the Physical Society. Section A **6**4, 667 (1951).

[21] Y. A. Budagov, S. Wiktor, V. Dzhelepov, P. Ermolov, and V. Moskalev, SOVIET PHYSICS JETP **1**1 (1960).

[22] N. P. Samios, Phys. Rev. **1**21, 275 (1961).

[23] M. A. Schardt *et al.*, Phys. Rev. D **2**3, 639 (1981).

[24] W.-M. Yao *et al.*, Journal of Physics G: Nuclear and Particle Physics **3**3, 001 (2006).

[25] D. Joseph, Il Nuovo Cimento (1955-1965) **1**6, 997 (1960).

[26] A. Beddall, The European Physical Journal C **5**4, 365 (2008).

[27] P. G. Zamora, *Measurement of the π^0 meson properties through its Dalitz decay channel in pp and p-pPb collisions with the ALICE experiment at the LHC*, PhD thesis, Madrid, CIEMAT, 2016.

[28] P. González, P. L. de Guevara, E. L. Torres, A. Marín, and E. Serradilla, The European Physical Journal C **6**1, 899 (2009).

[29] K. Hattori, K. Itakura, and S. Ozaki, (2013), 1305.7224.

[30] W. Dai, X.-F. Chen, B.-W. Zhang, and E. Wang, Physics Letters B **7**50, 390 (2015).

[31] J. Kapusta, P. Lichard, and D. Seibert, Phys. Rev. D **4**4, 2774 (1991).

[32] F.-M. Liu and K. Werner, Phys. Rev. Lett. **1**06, 242301 (2011).

[33] A. Ortiz Velasquez, P. Christiansen, E. Cuautle Flores, I. A. Maldonado Cervantes, and G. Paić, Phys. Rev. Lett. **1**11, 042001 (2013).

[34] A. Ayala, E. Cuautle, J. Magnin, and L. M. Montano, Phys. Rev. **C**74, 064903 (2006), nucl-th/0603039.

[35] A. Ayala, E. Cuautle, J. Magnin, L. M. Montaño, and A. Raya, Physics Letters B **6**34, 200 (2006).

[36] ALICE Collaboration, E. Rosas *et al.*, ALICE Analysis Note (2019).

[37] ALICE Collaboration, J. König *et al.*, ALICE Analysis Note (2021).

[38] Particle Data Group, M. Tanabashi and H. et al., Phys. Rev. D **9**8, 030001 (2018).

[39] N. M. Kroll and W. Wada, Phys. Rev. **9**8, 1355 (1955).

[40] A. Kalweit, Production of light flavor hadrons and anti-nuclei at the LHC, 2012.

[41] ALICE, B. B. Abelev *et al.*, Int. J. Mod. Phys. **A**29, 1430044 (2014), 1402.4476.

[42] ALICE Collaboration, L. Leardini, ALICE Analysis Note (2018).

[43] ALICE Collaboration, Murakami, Hikari, ALICE Analysis Note (2018).

[44] ALICE Collaboration, A. Passfeld, ALICE Analysis Note (2014).

[45] ALICE Collaboration, L. Leardini, ALICE Analysis Note (2017).

[46] ALICE Collaboration, M. C. Danisch, ALICE Analysis Note (2019).

[47] ALICE Collaboration, L. Leardini and M. Ana, ALICE Analysis Note (2018).

[48] E. Cuautle, E. D. Rosas, and M. Rodríguez-Cahuantzi, J. Phys. G **4**9, 105006 (2022), 2208.08072.

[49] E. Cuautle, E. Dominguez, and I. Maldonado, Eur. Phys. J. C **7**9, 626 (2019), 1907.08706.

[50] D. Sahu and R. Sahoo, Journal of Physics G: Nuclear and Particle Physics **4**8, 125104 (2021).

[51] X.-n. Wang and R. C. Hwa, Phys. Rev. D **3**9, 187 (1989).

[52] F. Rimondi, Physics of Atomic Nuclei **6**7, 130 (2004).

[53] A. Rossi *et al.*, Nuclear Physics B **8**4, 269 (1975).

[54] V. Khachatryan *et al.*, Journal of High Energy Physics **2**010, 1 (2010).

[55] K. Aamodt *et al.*, Physics Letters B **6**93, 53 (2010).

[56] CMS, S. Chatrchyan *et al.*, Eur. Phys. J. C **7**2, 2164 (2012), 1207.4724.

[57] M. Aaboud *et al.*, The European Physical Journal C-Particles and Fields **7**6 (2016).

[58] L. McLerran, Acta Phys. Polon. B **4**1, 2799 (2010), 1011.3203.

[59] A. Bzdak, B. Schenke, P. Tribedy, and R. Venugopalan, Physical Review C **8**7, 064906 (2013).

[60] V. Khachatryan *et al.*, Physics Letters B **7**65, 193 (2017).

[61] B. Abelev *et al.*, Physics Letters B **7**27, 371 (2013).

[62] P. Z. Skands, Physical Review D **8**2, 074018 (2010).

[63] J. R. Christiansen and T. Sjöstrand, The European Physical Journal C **7**5, 1 (2015).

[64] British-French-Scandinavian, M. G. Albrow *et al.*, Nucl. Phys. B **1**45, 305 (1978).

[65] U. C. Bonn-Brussels-Cambridge-CERN *et al.*, Physics Letters B **1**23, 361 (1983).

[66] M. Derrick *et al.*, Physical Review D **3**4, 3304 (1986).

[67] T. Alexopoulos *et al.*, Physics Letters B **3**53, 155 (1995).

[68] B. Abelev *et al.*, Physical review letters **1**03, 172301 (2009).

[69] G. Aad *et al.*, Journal of High Energy Physics **2**012, 1 (2012).

[70] J. Adam *et al.*, Journal of High Energy Physics **2**015, 1 (2015).

[71] A. Capella and A. Krzywicki, Phys. Rev. D **1**8, 4120 (1978).

[72] A. Capella, U. Sukhatme, C.-I. Tan, and J. Tran Thanh Van, Phys. Rept. **2**36, 225 (1994).

[73] N. S. Amelin, N. Armesto, M. A. Braun, E. G. Ferreiro, and C. Pajares, Phys. Rev. Lett. **7**3, 2813 (1994).

[74] M. A. Braun, R. S. Kolevatov, C. Pajares, and V. V. Vechernin, Eur. Phys. J. C **3**2, 535 (2004), hep-ph/0307056.

[75] A. Dumitru, F. Gelis, L. McLerran, and R. Venugopalan, Nucl. Phys. A **8**10, 91 (2008), 0804.3858.

[76] T. S. Biro, H. B. Nielsen, and J. Knoll, Nucl. Phys. B **2**45, 449 (1984).

[77] A. Bialas and W. Czyz, Nucl. Phys. B **2**67, 242 (1986).

[78] M. Braun and C. Pajares, Nucl. Phys. B **3**90, 542 (1993).

[79] N. S. Amelin, N. Armesto, M. A. Braun, E. G. Ferreiro, and C. Pajares, Phys. Rev. Lett. **7**3, 2813 (1994).

[80] B. Nachman and M. L. Mangano, The European Physical Journal C **7**8, 1 (2018).

[81] A. Ortiz, E. Cuautle, and G. Paić, Nuclear Physics A **9**41, 78 (2015).

[82] ALICE, J. Adam *et al.*, Nature Phys. **1**3, 535 (2017), 1606.07424.

[83] ALICE, S. Acharya *et al.*, Eur. Phys. J. C **7**7, 852 (2017), 1708.01435.

[84] CDF, F. Abe *et al.*, Phys. Rev. Lett. **7**9, 584 (1997).

[85] T. Sjostrand and M. van Zijl, Phys. Rev. D **3**6, 2019 (1987).

[86] T. Sjöstrand, Adv. Ser. Direct. High Energy Phys. **2**9, 191 (2018), 1706.02166.

[87] B. Abelev *et al.*, Physics Letters B **7**27, 371 (2013).

[88] A. Breakstone *et al.*, Zeitschrift für Physik C Particles and Fields **3**3, 333 (1987).

[89] T. Sjöstrand and M. van Zijl, Physical Review D **3**6, 2019 (1987).

[90] B. Andersson, G. Gustafson, G. Ingelman, and T. Sjöstrand, Physics Reports **9**7, 31 (1983).

[91] A. O. Velasquez, P. Christiansen, E. C. Flores, I. M. Cervantes, and G. Paić, Physical Review Letters **1**11, 042001 (2013).

[92] C. Bierlich, G. Gustafson, and L. Lönnblad, Physics Letters B **7**79, 58 (2018).

[93] T. Sjöstrand and P. Z. Skands, Journal of High Energy Physics **2**004, 053 (2004).

[94] B. Abelev *et al.*, Physics Letters B **7**39, 139 (2014).

[95] A. M. Sirunyan *et al.*, Physical Review C **9**7, 064912 (2018).

[96] L. McLerran, M. Praszalowicz, and B. Schenke, Nuclear Physics A **9**16, 210 (2013).

[97] CMS, V. Khachatryan *et al.*, JHEP **0**1, 079 (2011), 1011.5531.

[98] CMS, S. Chatrchyan *et al.*, Eur. Phys. J. C **7**4, 2847 (2014), 1307.3442.

[99] S. Chadha, C. Lam, and Y. Leung, Physical Review D **1**0, 2817 (1974).

[100] R. Sahoo, AAPPS Bull. **2**9, 16 (2019), 1908.10566.

[101] A. Bazavov *et al.*, Physical Review D **9**0, 094503 (2014).

[102] M. Braun *et al.*, Physics Reports **5**99, 1 (2015).

[103] R. Campanini and G. Ferri, Physics Letters B **7**03, 237 (2011).

[104] L. D. Landau, Izv. Akad. Nauk Ser. Fiz. **1**7, 51 (1953).

[105] B. Zakharov, Journal of Physics G: Nuclear and Particle Physics **4**1, 075008 (2014).

[106] N. Sharma, J. Cleymans, and B. Hippolyte, Advances in High Energy Physics **2**019 (2019).

[107] D. Sahu, S. Tripathy, R. Sahoo, and A. R. Dash, The European Physical Journal A **5**6, 1 (2020).

[108] J. D. Bjorken, Physical review D **2**7, 140 (1983).

[109] E. Cuautle and G. Paić, arXiv preprint arXiv:1608.02101 (2016).

[110] G. Paić and E. Cuautle, International Journal of Modern Physics E **2**5, 1642009 (2016).

[111] B. Abelev *et al.*, Physics Letters B **7**28, 25 (2014).

[112] K. Redlich and H. Satz, Physical Review D **3**3, 3747 (1986).

[113] R. Scharenberg, B. Srivastava, and A. Hirsch, The European Physical Journal C **7**1, 1 (2011).

[114] M. Waqas and F.-H. Liu, The European Physical Journal Plus **1**35, 147 (2020).

[115] F. G. Gardim, G. Giacalone, M. Luzum, and J.-Y. Ollitrault, Nature Physics **1**6, 615 (2020).

[116] J. R. Christiansen and P. Z. Skands, Journal of High Energy Physics **2**015, 1 (2015).

[117] P. Schwaller, D. Stolarski, and A. Weiler, Journal of High Energy Physics **2**015, 1 (2015).

[118] T. Sjöstrand, Adv. Ser. Direct. High Energy Phys. **2**9, 191 (2018), 1706.02166.

[119] K. Werner, Physical review letters **9**8, 152301 (2007).

[120] T. Pierog, I. Karpenko, J. M. Katzy, E. Yatsenko, and K. Werner, Physical Review C **9**2, 034906 (2015).

[121] T. Sjostrand, S. Mrenna, and P. Z. Skands, JHEP 05, 026 (2006).

[122] T. Sjostrand, S. Mrenna, and P. Z. Skands, Comput. Phys. Commun. 178, 852 (2008).

[123] R. K. Ellis, W. J. Stirling, and B. R. Webber, (2003).

[124] M. G. Bowler, Z. Phys. C **1**1, 169 (1981).

[125] X. Artru and G. Mennessier, Nucl. Phys. B **7**0, 93 (1974).

[126] D. A. Morris, Nucl. Phys. B **3**13, 634 (1989).

[127] R. Field and R. Feynman, Nuclear Physics B **1**36, 1 (1978).

[128] C. Peterson, D. Schlatter, I. Schmitt, and P. M. Zerwas, Phys. Rev. D **2**7, 105 (1983).

[129] E. Cuautle, A. Ortiz, and G. Paic, Nucl. Phys. A **9**56, 749 (2016), 1512.09011.

[130] J. R. Christiansen and T. Sjöstrand, Eur. Phys. J. C **7**5, 441 (2015), 1506.09085.

[131] S. Argyropoulos and T. Sjöstrand, Journal of High Energy Physics **2**014, 1 (2014).

[132] A. O. Velasquez, P. Christiansen, E. C. Flores, I. M. Cervantes, and G. Paić, Physical Review Letters **1**11, 042001 (2013).